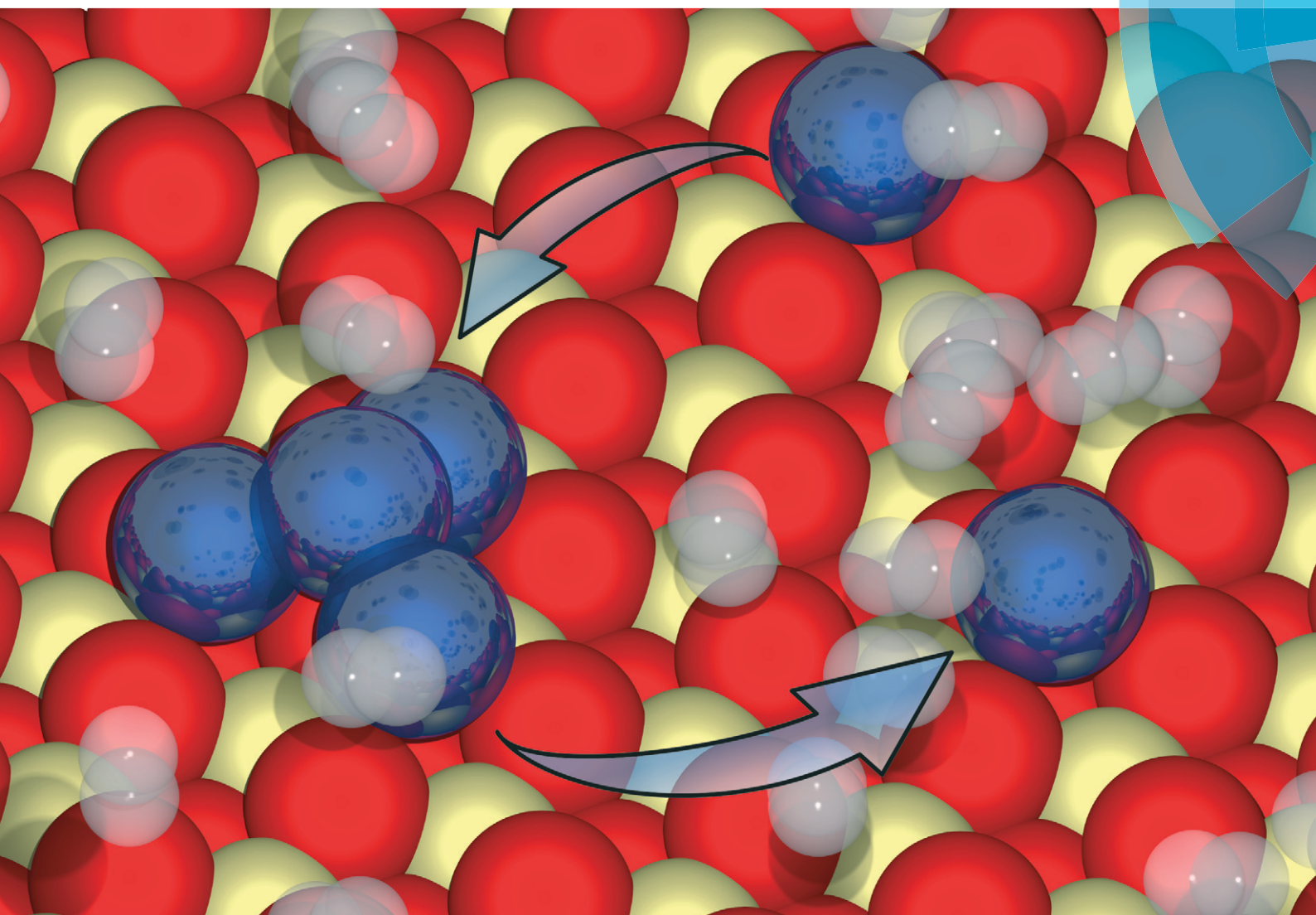


# Catalysis Science & Technology

rsc.li/catalysis



Themed issue: Single atom catalysis

ISSN 2044-4761



## MINIREVIEW

Yaroslava Lykhach, Vladimír Matolín, Jörg Libuda, Konstantin M. Neyman et al.  
Oxide-based nanomaterials for fuel cell catalysis: the interplay between supported single Pt atoms and particles



Cite this: *Catal. Sci. Technol.*, 2017,  
7, 4315

## Oxide-based nanomaterials for fuel cell catalysis: the interplay between supported single Pt atoms and particles

Yaroslava Lykhach, \*<sup>a</sup> Albert Bruix, <sup>b</sup> Stefano Fabris, <sup>c</sup> Valérie Potin, <sup>d</sup> Iva Matolínová, <sup>e</sup> Vladimír Matolín, \*<sup>e</sup> Jörg Libuda \*<sup>af</sup> and Konstantin M. Neyman \*<sup>gh</sup>

The concept of single atom catalysis offers maximum noble metal efficiency for the development of low-cost catalytic materials. Among possible applications are catalytic materials for proton exchange membrane fuel cells. In the present review, recent efforts towards the fabrication of single atom catalysts on nanostructured ceria and their reactivity are discussed in the prospect of their employment as anode catalysts. The remarkable performance and the durability of the ceria-based anode catalysts with ultra-low Pt loading result from the interplay between two states associated with supported atomically dispersed Pt and sub-nanometer Pt particles. The occurrence of these two states is a consequence of strong interactions between Pt and nanostructured ceria that yield atomically dispersed species under oxidizing conditions and sub-nanometer Pt particles under reducing conditions. The square-planar arrangement of four O atoms on {100} nanoterraces has been identified as the key structural element on the surface of the nanostructured ceria where Pt is anchored in the form of  $\text{Pt}^{2+}$  species. The conversion of  $\text{Pt}^{2+}$  species to sub-nanometer Pt particles is triggered by a redox process involving  $\text{Ce}^{3+}$  centers. The latter emerge due to either oxygen vacancies or adsorption of reducing agents. The unique properties of the sub-nanometer Pt particles arise from metal-support interactions involving charge transfer, structural flexibility, and spillover phenomena. The abundance of specific adsorption sites similar to those on {100} nanoterraces determines the ideal (maximum) Pt loading in  $\text{Pt}-\text{CeO}_x$  films that still allows reversible switching between the atomically dispersed Pt and sub-nanometer particles yielding high activity and durability during fuel cell operation.

Received 11th April 2017,  
Accepted 31st May 2017

DOI: 10.1039/c7cy00710h

rsc.li/catalysis

### 1. Introduction

Hydrogen powered proton exchange membrane fuel cells (PEMFCs) are considered potential next generation power

<sup>a</sup> Lehrstuhl für Physikalische Chemie II, Friedrich-Alexander-Universität Erlangen-Nürnberg, Egerlandstrasse 3, 91058 Erlangen, Germany.

E-mail: yaroslava.lykhach@fau.de, joerg.libuda@fau.de; Fax: +49 9131 8528867

<sup>b</sup> Department of Physics and Astronomy and Interdisciplinary Nanoscience Center, Aarhus University, Ny Munkegade 120, Building 1520, DK-8000 Aarhus, Denmark

<sup>c</sup> CNR-IOM DEMOCRITOS, Istituto Officina dei Materiali, Consiglio Nazionale delle Ricerche and SISSA, Via Bonomea 265, I-34136, Trieste, Italy

<sup>d</sup> Laboratoire Interdisciplinaire Carnot de Bourgogne, UMR 6303 CNRS-Université de Bourgogne Franche-Comté, 9 Av. A. Savary, BP 47870, F-21078 Dijon Cedex, France

<sup>e</sup> Faculty of Mathematics and Physics, Department of Surface and Plasma Science, Charles University, V Holešovičkách 2, 18000 Prague, Czech Republic.

E-mail: matolin@mbox.troja.mff.cuni.cz

<sup>f</sup> Erlangen Catalysis Resource Center, Friedrich-Alexander-Universität Erlangen-Nürnberg, Egerlandstrasse 3, 91058 Erlangen, Germany

<sup>g</sup> Departament de Ciència dels Materials i Química Física and Institut de Química Teòrica i Computacional, Universitat de Barcelona, c/ Martí i Franquès 1, 08028 Barcelona, Spain

<sup>h</sup> ICREA (Institució Catalana de Recerca i Estudis Avançats), Pg. Lluís Companys 23, 08010 Barcelona, Spain. E-mail: konstantin.neymen@icrea.cat; Fax: +34 93 40 21 231

sources for a variety of small to medium-scale applications, including automotive vehicle propulsion and chip-integrated micro-devices.<sup>1–3</sup> For PEMFC technology, platinum is the essential catalytic element. Typically, commercial anode catalysts contain about  $2\text{--}5 \text{ mg cm}^{-2}$  of the noble metal. The high cost of platinum is the main factor limiting the large-scale application of fuel cell technology. Therefore, great efforts are dedicated to the development of catalytic materials for PEMFCs to meet the standards defined by the US Department of Energy (DOE).<sup>4</sup> The latest developments in fuel cell technology may reduce the total Pt loading in PEMFCs to  $0.15 \text{ mg cm}^{-2}$  which is still above the target value ( $0.125 \text{ mg cm}^{-2}$ ) set for the year 2017.<sup>4</sup>

In the prospect of further reduction of Pt loading, supported single atom catalysts (SACs) offer ultimate noble metal efficiency by exposing the entire noble-metal content to reactants.<sup>5–8</sup> The synthesis and performance of SACs in numerous heterogeneous reactions have been recently reviewed in detail.<sup>6–10</sup> Several key challenges have been identified with respect to the stability and reactivity of the atomically dispersed noble metals. In particular, anchoring of noble metal atoms at appropriate supports requires the presence of

specific adsorption sites that are capable of stabilizing metal atoms against sintering and agglomeration into particles. Such sites have been identified on the surfaces of graphene,<sup>11–13</sup> nitrides,<sup>14–18</sup> zeolites,<sup>19</sup> and metal oxides.<sup>20–31</sup> In most cases, atomically dispersed metals are found to be anchored in surface cationic positions of the host oxide.<sup>23,28,30,32</sup> Depending on the oxidation state of the anchored metal atom, spontaneous formation of anionic or cationic vacancies occurs to balance the charge. In some cases, anchoring of the metal atom is achieved through the spatial confinement in pores or open channels of the support.<sup>17,18,33</sup> The stability of the anchored metal atoms and their propensity to agglomerate is determined by the energy difference between the states associated with an adsorbed metal atom and a supported metal particle. In this respect, the use of metal oxides allows employing metal-support interactions to achieve a strong binding between the metal and the support.<sup>34–36</sup> Conceptually, oxide supported noble metal SACs are closely related to noble metal-doped oxides.<sup>36–38</sup> However, the common disadvantage of the latter is that a substantial amount of the noble metal is atomically dispersed in the bulk.<sup>36–38</sup> As a result, the density of the noble-metal sites at the surface is low. An increase of the noble metal loading in doped oxides, on the other hand, often gives rise to metallic particles at the surface.<sup>36</sup>

Different strategies are applied to increase the density of the atomically dispersed species at the surface. These include grafting of the atomically dispersed metals, the use of stabilizing ligands, and nanostructuring of the support. In particular, new sites emerge at the surface of the nanostructured oxides that may anchor atomically dispersed noble metals in a structural environment which is energetically highly favorable<sup>21</sup> with respect to cationic substitution in the doped bulk.<sup>36</sup> Under these circumstances, the segregation of the noble metal is driven thermodynamically, yielding a high density of atomically dispersed noble metal at the surface.<sup>27</sup>

In the following review we summarize the properties of new materials containing atomically dispersed noble metals anchored at surface sites of nanostructured ceria. In particu-

lar, the catalytic performance of atomically dispersed platinum supported on nanostructured ceria is discussed in the prospect of applications as anode catalysts for PEMFCs. The remarkable properties of these catalysts involve the interplay between the two states associated with the atomically dispersed noble metal and sub-nanometer particles. The great stability and durability of the prototype anode catalyst arise from reversible switching between these two states under operating PEMFC conditions.

## 2. Supported single atom catalysts in proton exchange membrane fuel cells

### 2.1. High efficiency at ultra-low noble metal loading

The performance of Pt–CeO<sub>2</sub> catalysts with ultra-low Pt loading prepared by means of radio frequency sputtering was tested under relevant PEMFC conditions.<sup>21,39–44</sup> The key parameter determining the cost efficiency of the fuel cell catalyst is the specific power (SP), *i.e.* the power density (PD) per weight of noble metal. The corresponding SPs and PDs achieved using the Pt–CeO<sub>2</sub> catalysts at the anode (Table 1) were compared with those of a commercial Pt nanoparticle catalyst and Pt thin films (Table 2) under identical operation conditions.

The thin film of the Pt–CeO<sub>2</sub> catalyst deposited directly on the gas diffusion layer (GDL) yielded a higher PD with respect to the reference PtRu anode catalyst despite the ten-fold lower Pt loading.<sup>39,40</sup> The use of double-wall (DWCNT),<sup>40</sup> multi-wall (MWCNT),<sup>42</sup> and chemical vapor deposited (CVD-CNT)<sup>43</sup> carbon nanotubes resulted in a further increase of PDs and SPs (see Table 1). With respect to the commercial Pt anode (Table 2a), the Pt–CeO<sub>2</sub> catalyst yielded an around 10<sup>2</sup>-fold increase of the SP.<sup>41</sup>

Additionally, an increase of the operation temperature of the fuel cell yielded an approximately two-fold increase of the PD and SP.<sup>43</sup> However, the highest PD and SP were obtained with the Pt–CeO<sub>2</sub> catalyst deposited on carbon nanoparticle coated GDL (nanoGDL, also n-GDL).<sup>21,41,44</sup>

**Table 1** Power density (PD) and specific power (SP) obtained with the Pt–CeO<sub>2</sub> anode catalyst as a function of Pt loading, the catalyst support, and temperature

Catalyst support	Pt loading ( $\mu\text{g cm}^{-2}$ )	T (K)	PD ( $\text{mW cm}^{-2}$ )	SP ( $\text{W mg}^{-1}$ )	Ref.
GDL	2.2	300	4.9	2.5	39
	2.2 <sup>a</sup>	300	10.5	5.4	39
	1.2	300	12.3	10	40
	1.2	313	15.5	12.6	40
	0	300	0.41	—	40
DWCNT/GDL	1.2	300	43	35	40
MWCNT/GDL	0.9	300	25	28	42
CVD-CNT/GDL	0.9	348	38	42	42
	0.9	300	40	44.4	43
		342	70	77.8	43
n-GDL		348	74	82.2	43
	4	338	330	82.5	41, 44
	2	338	410	205	21, 41
	0.6	338	170	283	41

<sup>a</sup> The catalyst contains Sn.



**Table 2** Power density (PD) and specific power (SP) obtained with anode catalysts based on a commercial Pt nanoparticle catalyst (a) and thin Pt films (b and c) as a function of noble metal loading, the catalyst support, and temperature

Anode catalyst	Pt loading ( $\mu\text{g cm}^{-2}$ )	T (K)	PD ( $\text{mW cm}^{-2}$ )	SP ( $\text{W mg}^{-1}$ )	Ref.
(a) Pt/GDL	2000	338	440	0.22	41
(b) Pt/GDL	21.45	300	2.4	0.12	40
(c) Pt/n-GDL	2	338	75	37	41

The morphology of the GDL support has a critical influence on the performance of the Pt–CeO<sub>2</sub> catalyst. Scanning electron microscopy (SEM) revealed characteristic differences in the structure of the bare GDL, GDL coated with DWCNTs, MWCNTs, and CVD-CNTs, and n-GDL (see Fig. 1).

The main difference between the CNT-coated GDL supports (Fig. 1b-d) is the diameter of the tubes and their alignment with respect to the surface of GDL. In particular, CVD-CNTs grow perpendicular to the surface of GDL while DWCNTs and MWCNTs deposited by spin-coating are aligned parallel to the surface of GDL.<sup>42</sup>

## 2.2. The composition of the catalysts

The composition of the Pt–CeO<sub>2</sub> anode catalysts and the Pt oxidation state were investigated as a function of the information depth.<sup>39,40</sup> The experimental approach involved a combination of high-resolution synchrotron spectroscopy (SRPES), angle-resolved X-ray photoelectron spectroscopy (AR XPS), and hard X-ray photoelectron spectroscopy (HAXPS).<sup>48</sup> The information depth achieved with these techniques increases with increasing photon energies ( $h\nu$ ) and  $\cos(\alpha)$  with respect to the surface normal from 0.5 nm (SRPES) and 1–2 nm (AR XPS) to 7 nm (HAXPS). The corresponding Pt 4f spectra obtained from the Pt–CeO<sub>2</sub> thin films with SRPES, AR XPS, and HAXPS are shown in Fig. 2.

The major contributions in the Pt 4f spectra arise from atomically dispersed Pt<sup>2+</sup> and Pt<sup>4+</sup> species. Additionally, traces of metallic Pt<sup>0</sup> were identified at the surface of Pt–CeO<sub>2</sub> films (Fig. 2, bottom spectrum). The formation of ionic species is typically found for films prepared by magnetron co-sputtering of CeO<sub>2</sub> in combination with transition

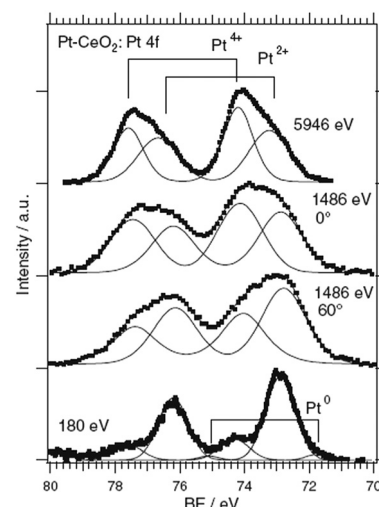


**Fig. 2** Pt 4f spectra obtained from the Pt–CeO<sub>2</sub> film by means of SRPES ( $h\nu = 180 \text{ eV}$ ,  $\alpha = 0^\circ$ ), AR XPS ( $h\nu = 1486 \text{ eV}$ ,  $\alpha = 60^\circ$  and  $0^\circ$ ), and HAXPS ( $h\nu = 5946 \text{ eV}$ ,  $\alpha = 0^\circ$ ). Reproduced with permission from ref. 39, Copyright 2009, The Electrochemical Society.

metals.<sup>40,49,50</sup> The ratio between the Pt<sup>2+</sup>, Pt<sup>4+</sup>, and Pt<sup>0</sup> contributions in the Pt 4f is a function of the sampling depth. Accordingly, Pt<sup>4+</sup> species are located mostly in the bulk while Pt<sup>2+</sup> and Pt<sup>0</sup> reside at the surface.

The relationship between the performance of the Pt–CeO<sub>2</sub> catalyst supported on n-GDL and the abundance of Pt<sup>2+</sup>, Pt<sup>4+</sup>, and Pt<sup>0</sup> species can be derived from the comparison of the SPs (Table 1) and the shape of the corresponding Pt 4f spectra (Fig. 3a) as a function of Pt loading.

Clearly, the SP is directly related to the Pt<sup>2+</sup>/Pt<sup>4+</sup> ratio in the films. The highest SP was obtained at the highest Pt<sup>2+</sup>/Pt<sup>4+</sup> ratio corresponding to the lowest Pt loading ( $0.6 \mu\text{g cm}^{-2}$ ). However, the PD shows a rather non-linear dependence on the Pt<sup>2+</sup>/Pt<sup>4+</sup> ratio. The maximum PD was achieved at moderate Pt loading ( $2 \mu\text{g cm}^{-2}$ ) and at a lower Pt<sup>2+</sup>/Pt<sup>4+</sup> ratio. Note that a further increase of the Pt loading yielded a lower Pt<sup>2+</sup>/Pt<sup>4+</sup> ratio and resulted in a substantial decrease of the PD (Table 1). The analysis of the Pt–CeO<sub>2</sub> catalyst after running several FC cycles revealed conversion of the Pt<sup>4+</sup> species to Pt<sup>2+</sup> and Pt<sup>0</sup> (Fig. 3b). As a result, both Pt–CeO<sub>2</sub> films with Pt loadings  $0.6$  and  $2 \mu\text{g cm}^{-2}$  contain Pt<sup>2+</sup> species, exclusively. Despite the slightly lower SP, the Pt–CeO<sub>2</sub> film with

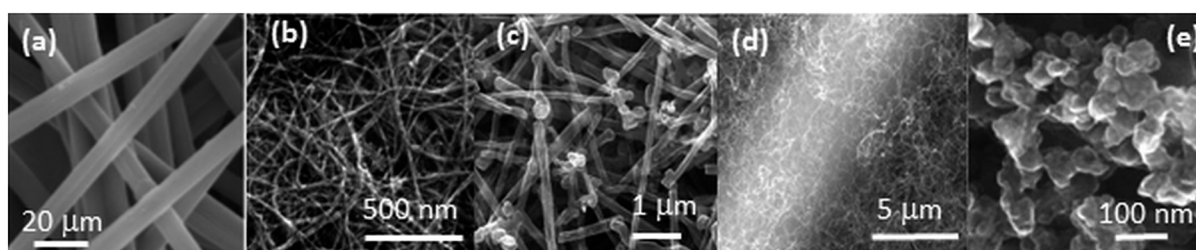


**Fig. 1** SEM images of bare (a) and DWCNT (b), MWCNT (c), CVD-CNT (d) coated GDL, and n-GDL (e). (a) Reprinted from ref. 45 with permission from John Wiley & Sons, Inc. Copyright 2016 by John Wiley & Sons, Inc. (b) Adapted from ref. 40, Copyright 2009, The Electrochemical Society. (c) Reprinted from ref. 46 with permission from John Wiley & Sons, Inc. Copyright 2010 by John Wiley & Sons, Inc. (e) Reprinted from ref. 47, Copyright 2015, with permission from Elsevier.



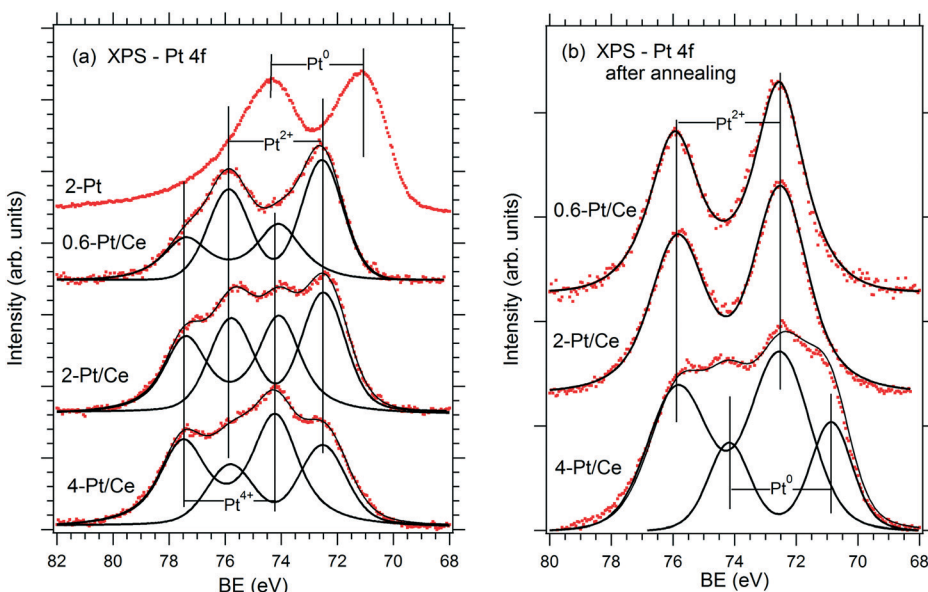


**Fig. 3** Pt 4f spectra obtained from the reference Pt film ( $2 \mu\text{g Pt cm}^{-2}$ , 2-Pt) and Pt–CeO<sub>2</sub> films supported on n-GDL with Pt loadings of 0.6 (0.6-Pt/Ce), 2 (2-Pt/Ce) and 4 (4-Pt/Ce)  $\mu\text{g Pt cm}^{-2}$  before (a) and after annealing under PEMFC operating conditions (b). Reprinted from ref. 41, Copyright 2016, with permission from Elsevier.

a Pt loading of  $2 \mu\text{g cm}^{-2}$  shows a significantly higher PD with respect to the film with a Pt loading of  $0.6 \mu\text{g cm}^{-2}$ . Under these conditions, the PD increases with the density of Pt<sup>2+</sup> species. From the perspective of volumetric power densities, the Pt–CeO<sub>2</sub> catalyst with a Pt loading of  $2 \mu\text{g cm}^{-2}$  is therefore the most suitable for a compact design of the FC.

The presence of metallic Pt<sup>0</sup> deteriorated the catalyst performance (see Fig. 3 and Table 1 for a Pt loading of  $4 \mu\text{g cm}^{-2}$ ). It follows that the excellent performance of the Pt–CeO<sub>2</sub> catalyst is associated with the high density and the enhanced stability of Pt<sup>2+</sup> species.

### 2.3. Parameters controlling proton exchange membrane fuel cell performance

The main parameter that controls the abundance of Pt<sup>2+</sup> species on the Pt–CeO<sub>2</sub> catalyst is the morphology of the support. The SEM images obtained from Pt–CeO<sub>2</sub> deposited on CNT-coated GDL and n-GDL are shown in Fig. 4. The mor-

phology of the Pt–CeO<sub>2</sub> anode catalyst corresponds to a porous columnar structure<sup>42</sup> that varies as a function of the support with respect to the width and height of the crystallites. The degree of nanostructuring increases for films deposited on CNT-coated GDLs (Fig. 4a–c) and n-GDLs (Fig. 4d) with respect to the bare GDL.

The parameters controlling the growth of Pt–CeO<sub>2</sub> films have been systematically investigated with respect to the microstructure of the carbon films, the pressure and the temperature. It was found that the major process giving rise to the porous structure of the Pt–CeO<sub>2</sub> films is associated with the etching of the carbon films by oxygen plasma.<sup>52–55</sup> The corresponding mechanism involves the formation of nucleation centers, *e.g.* Pt–CeO<sub>x</sub> or Ce–C particles which mask the carbon substrate partially and, thus, prevent etching.<sup>53,55</sup> The density and the mobility of these nucleation centers determine the width of the columns. Additional parameters are the deposition rate<sup>55</sup> and thickness<sup>56</sup> of the Pt–CeO<sub>2</sub> films, temperature, and the composition of the reactive gas.<sup>54,55</sup>

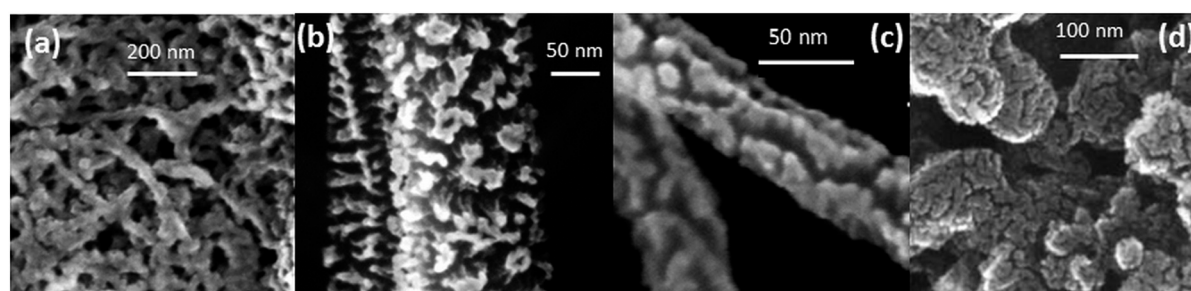


**Fig. 4** SEM images of the Pt–CeO<sub>2</sub> anode catalyst deposited on DWCNT (a), MWCNT (b), and CVD-CNT (c) coated GDL, and n-GDL (d). (a) Adapted with permission from ref. 40, Copyright 2009, The Electrochemical Society. (b) Reprinted with permission from ref. 51, Copyright 2012, InderScience Enterprises Ltd. (d) Reprinted from ref. 47, Copyright 2015, with permission from Elsevier.

## 2.4. Preparation of the nanostructured Pt–CeO<sub>2</sub> films

Besides radio frequency magnetron sputtering,<sup>21,39–44</sup> the nanostructured Pt–CeO<sub>2</sub> films can be prepared by a variety of other techniques including pulsed laser deposition<sup>57</sup> and chemical vapor deposition techniques.<sup>58–61</sup> The preparation of nanostructured Pt–CeO<sub>2</sub> films by means of physical vapor co-deposition of Pt and Ce in an oxygen atmosphere requires low deposition temperature.<sup>21</sup> For some methods, *e.g.* pulsed laser deposition, the degree of the nanostructuring of the Pt–CeO<sub>2</sub> films depends on the morphology, *i.e.* roughness of the support.<sup>57</sup>

## 2.5. Identification of the surface sites on the nanostructured CeO<sub>2</sub> support

The degree of the nanostructuring of the Pt–CeO<sub>2</sub> films determines the density of the Pt<sup>2+</sup> species and is closely related to the number of Ce<sup>3+</sup> cations.<sup>42,52</sup> For instance, the Pt<sup>2+</sup>/Pt<sup>4+</sup> ratio is much higher in the Pt–CeO<sub>2</sub> films deposited under glancing angle (GLAD) conditions.<sup>46</sup> In contrast, normal deposition (ND) yielded mainly Pt<sup>4+</sup> species accompanied by a low number of Ce<sup>3+</sup> cations.<sup>62</sup> It was found that Ce<sup>3+</sup> sites are located predominantly at the surface steps and edges of the nanostructured Pt–CeO<sub>2</sub> films.<sup>42</sup>

The surface of the Pt–CeO<sub>2</sub> films was investigated by means of high-resolution transmission electron microscopy (HRTEM). There, the Pt–CeO<sub>2</sub> nanoparticles terminated by the {111} and {100} facets were identified in the Pt–CeO<sub>2</sub> films supported on CNT-coated GDL,<sup>42,43</sup> n-GDL,<sup>41,44</sup> and silicon wafers.<sup>42,63</sup> Typical HRTEM images obtained from the Pt–CeO<sub>2</sub> films supported on n-GDL are shown in Fig. 5 for two different Pt loadings.

The structure of the Pt–CeO<sub>2</sub> films is identical to the structure of bare CeO<sub>2</sub> films and does not depend on the choice of the preparation technique. For instance, nanoparticles of CeO<sub>2</sub> and Pt–CeO<sub>2</sub> terminated predominantly by the {111} and {100} facets have been identified in films prepared by magnetron sputtering,<sup>56,64</sup> chemical vapor deposition,<sup>60</sup> and pulsed laser deposition.<sup>57</sup> It follows that with respect to the nature of Pt<sup>2+</sup> surface species, either the {111} or {100} facets or edge and step sites connecting

these facets provide the adsorption sites that anchor atomically dispersed Pt atoms.

## 3. Stability of single atom catalysts

### 3.1. Anchoring noble metal atoms at surface sites of nanostructured ceria

The capacity of the nanostructured ceria to anchor atomically dispersed noble metals at the {111} and {100} facets was analyzed by means of density functional calculations.<sup>21</sup> A Ce<sub>40</sub>O<sub>80</sub> nanoparticle model<sup>65,66</sup> featuring a truncated octahedral shape with O-terminated {111} and very small {100} facets was identified as a representative model for nanostructured ceria.<sup>67</sup> This particle structure, displayed in Fig. 6, emerged from an exhaustive global optimization search.<sup>65,66,68</sup> The polar {100} surface corresponding to the {100} nanofacets of the ceria particles is known to be less stable than the {111} surface of ceria.<sup>69</sup> Each of these {100} nanofacets is terminated by four surface O<sup>2-</sup> ions in a square planar arrangement with O–O distances of 315–320 pm forming a so-called O<sub>4</sub> pocket.

The binding of Pt atoms adsorbed on the regular CeO<sub>2</sub>(111) surface in the form of Pt<sup>0</sup> or Pt<sup>+</sup> is associated with a low diffusion barrier along the surface.<sup>71</sup> The formation of Pt<sub>2</sub> dimers is therefore kinetically facile and strongly exothermic (by 369 kJ mol<sup>-1</sup>)<sup>72</sup> giving rise to rapid nucleation of Pt particles.<sup>73</sup> In turn, the oxidation state and adsorption energy of Pt atoms on the surface of ceria nanoparticles drastically depend on the local structure of the adsorption sites. A moderately strong binding of atomic Pt on edge sites between {111} facets of the Ce<sub>40</sub>O<sub>80</sub> nanoparticle yields Pt<sup>0</sup> and Pt<sup>+</sup> species with the adsorption energies of -273 and -303 kJ mol<sup>-1</sup>, respectively.<sup>21</sup> Similar adsorption energies were calculated for Pt<sup>0</sup> (-256 kJ mol<sup>-1</sup>) and Pt<sup>+</sup> species (-226 kJ mol<sup>-1</sup>) on the regular CeO<sub>2</sub>(111) surface.<sup>71</sup> This adsorption strength of atomic Pt is typical also for regular surfaces of more inert non-reducible metal oxides, such as MgO(001).<sup>74</sup> In contrast, the adsorption of Pt atoms on the {100} nanofacet yields Pt<sup>2+</sup> species with an extraordinarily large binding energy of -678 kJ mol<sup>-1</sup>,<sup>21</sup> which is ~100 kJ mol<sup>-1</sup> more in magnitude than that for Pt atoms anchored to neutral oxygen vacancies of the MgO(001) surface.<sup>75</sup> In these calculations the formal oxidation state of the adsorbed Pt atom was determined by the number of Ce<sup>3+</sup> centers formed *via* electron transfer into the 4f orbitals of Ce<sup>4+</sup>. Consequently, the formation of Pt<sup>+</sup> or Pt<sup>2+</sup> species is accompanied by the reduction of one or two Ce<sup>4+</sup> cations to Ce<sup>3+</sup>, respectively (Fig. 6).

Strong interactions of metal atoms with oxide surfaces are indicative of surface coordination compounds, in which the support acts as a polydentate ligand.<sup>76</sup> Indeed, the O<sub>4</sub> site provides an ideal coordination environment to host the Pt<sup>2+</sup> (d<sup>8</sup>) species yielding a square planar PtO<sub>4</sub> moiety.<sup>77</sup> Remarkably, the adsorption energy of the anchored Pt<sup>2+</sup> ion exceeds in magnitude the cohesive energy of bulk Pt (~564 kJ mol<sup>-1</sup>).<sup>78</sup> As a consequence, Pt<sup>2+</sup> species are thermodynamically stable against sintering. The structure of the resulting PtO<sub>4</sub> moiety is consistent with the interatomic distances and

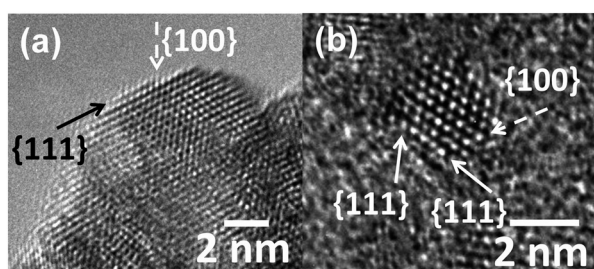
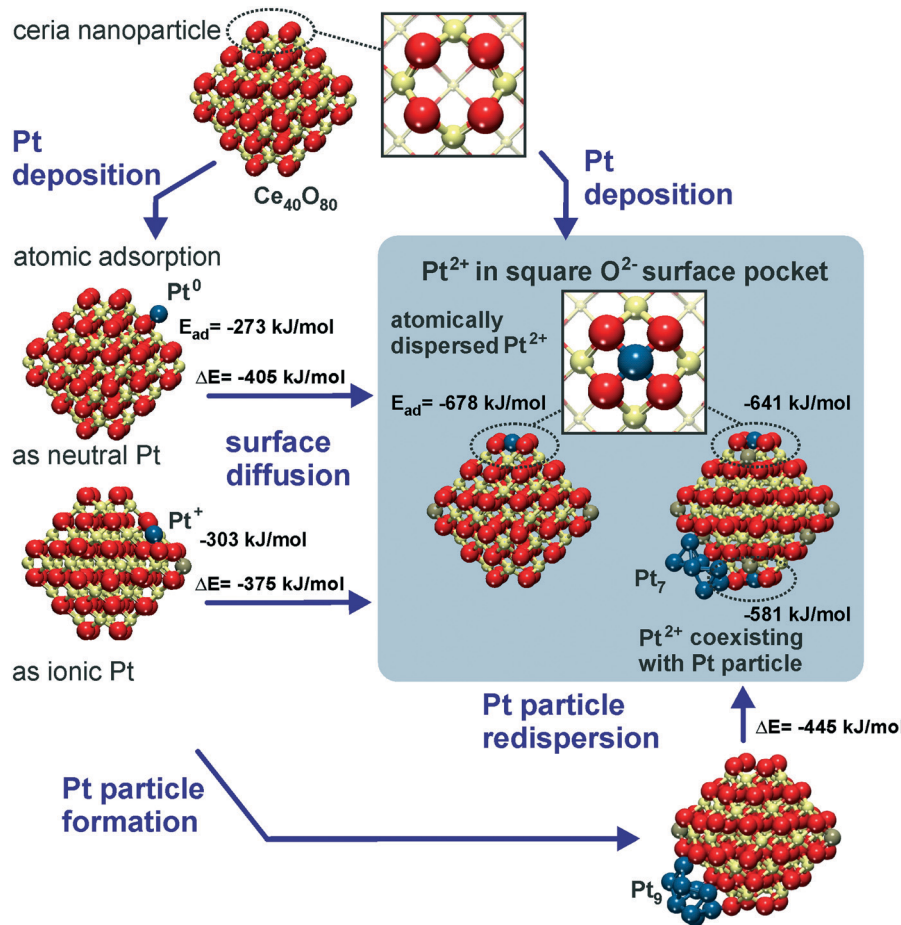


Fig. 5 HRTEM images of the Pt–CeO<sub>2</sub> films supported on n-GDL with Pt loadings of 2 (a) and 4 (b)  $\mu\text{g cm}^{-2}$ . The arrows show the location of the {111} and {100} facets. Reprinted from ref. 41, Copyright 2016, with permission from Elsevier.





**Fig. 6** Structure and energetics of various anchored Pt species on ceria nanoparticles obtained from density functional calculations.  $\text{Pt}^{2+}$  is strongly bound to square  $\text{O}_4$  pockets at the  $\{100\}$  nanofacets of the particles. Color coding of atoms: red O, beige  $\text{Ce}^{4+}$ , brown  $\text{Ce}^{3+}$ , and blue Pt. Reproduced with permission from ref. 70, Copyright 2016, Springer International Publishing AG.

coordination numbers of Pt atoms determined by means of extended X-ray absorption fine structure (EXAFS) studies on real Pt/ceria catalysts.<sup>79</sup>

With respect to sintering and re-dispersion processes, the DFT calculations suggest that the  $\text{O}_4$  sites are even able to abstract Pt atoms from supported Pt particles<sup>21</sup> (Fig. 6). This pathway was calculated to be exothermic for Pt<sub>9</sub> and Pt<sub>8</sub> particles on  $\text{Ce}_{40}\text{O}_{80}$ , where the migration of Pt atoms from the metal particle to the  $\{100\}$  nanofacets of ceria leads to their transformation into strongly bound  $\text{Pt}^{2+}$  species.

Furthermore, the anchored  $\text{Pt}^{2+}$  species do not serve as a stable nucleation site for a second Pt atom. Accordingly, no local minimum corresponding to a  $\text{Pt-Pt}^{2+}/\text{O}_4$  moiety was found and during geometry optimization a supported Pt<sub>2</sub> dimer dissociated into a  $\text{Pt}^{2+}/\text{O}_4$  complex and a neutral Pt atom adsorbed nearby. This finding implies that the anchored  $\text{Pt}^{2+}$  species can actually coexist with Pt particles without being buried by excess Pt.

A very similar local  $\text{PtO}_4$  structure emerges upon Pt adsorption at the steps of the  $\text{CeO}_2(111)$  surface.<sup>22</sup> The thermodynamics of segregation and the corresponding atomic and electronic structures of Pt on stepped  $\text{CeO}_2(111)$  were investi-

gated by density functional calculations.<sup>22</sup> Different adsorption sites were considered (Fig. 7) including oxygen vacancies (a), regular sites (b) and Pt clusters (c) on the  $\text{CeO}_2(111)$  terrace, and the two low-energy one-monolayer-high steps labeled as step I (d, f) and step II (e, g) on stoichiometric (denoted S) and non-stoichiometric (with excess of oxygen, denoted O) surfaces. Structures I and II represent the preferred types of steps at the  $\text{CeO}_2(111)$  surfaces at temperatures below 1000 K.<sup>80,81</sup>

Pt adsorption at step I-S yields  $\text{Pt}^{2+}$  species coordinated by four lattice O atoms in a characteristic  $\text{PtO}_4$  planar unit (Fig. 7d) similar to that identified on the  $\{100\}$  facets of the  $\text{Ce}_{40}\text{O}_{80}$  nanoparticle.<sup>21</sup> Consequently, two  $\text{Ce}^{3+}$  centers are formed in the proximity of the  $\text{Pt}^{2+}$  (Fig. 7d). The resulting adsorption energy of  $\text{Pt}^{2+}$  is  $-5.0 \text{ eV}$ . In contrast, the different atomic structure of the step II-S edge prevents the formation of the  $\text{PtO}_4$  moiety and yields a weakly oxidized  $\text{Pt}^{4+}$  species accompanied by the emergence of one  $\text{Ce}^{3+}$  center (Fig. 7e).

The presence of excess oxygen at the steps triggers restructuring and yields  $\text{Pt}^{2+}$  in the characteristic square-planar  $\text{PtO}_4$  surface arrangement. At step I, the excess oxygen leads to the oxidation of  $\text{Ce}^{3+}$  centers to  $\text{Ce}^{4+}$  while  $\text{Pt}^{2+}$

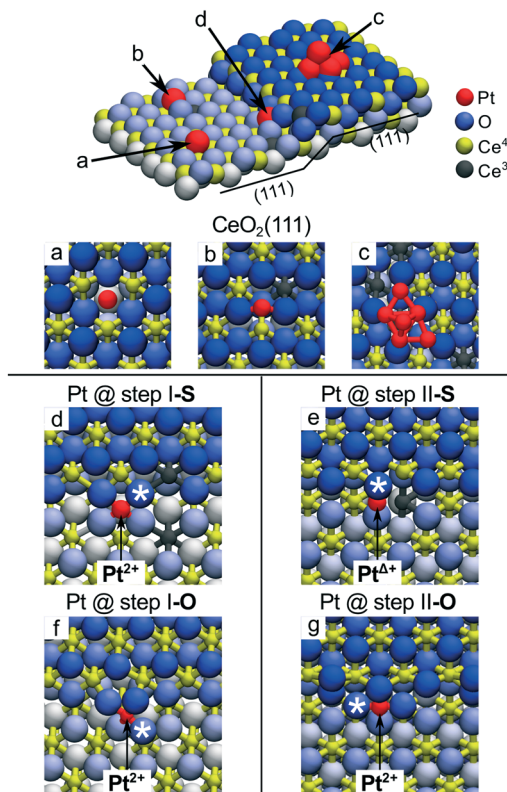


**Fig. 7** Pt adsorption sites on the stepped  $\text{CeO}_2(111)$  surface. (a) Pt adatom in the surface O vacancy, (b) on the stoichiometric  $\text{CeO}_2(111)$  terrace and (c) supported  $\text{Pt}_6$  cluster. (d) Pt adatom at the stoichiometric step I (step I-S) and (e) at the stoichiometric step II (step II-S). (f) Pt adatom at step I with excess O (step I-O) and (g) at step II with excess O (step II-O). Reproduced with permission from ref. 22, Copyright 2016, Nature Publishing Group.

retains its oxidation state. At step II, the oxidation of the  $\text{Pt}^{4+}$  species to  $\text{Pt}^{2+}$  is accompanied by the oxidation of one  $\text{Ce}^{3+}$  to  $\text{Ce}^{4+}$ . Remarkably, the resulting binding energies of  $\text{Pt}^{2+}$  species in excess of oxygen are  $\sim 1.6$  eV higher (*i.e.* more strongly bound) with respect to that calculated for Pt adsorption on stoichiometric step sites. These results demonstrate that stable  $\text{PtO}_4$  moieties with  $\text{Pt}^{2+}$  species can be formed at step sites of ceria upon oxidation of  $\text{Pt}^0$  to  $\text{Pt}^{2+}$  and that the formation of such  $\text{Pt}^{2+}$  species does not necessarily involve the formation of  $\text{Ce}^{3+}$  ions.<sup>22</sup>

The calculations predict the preferential adsorption of Pt atoms at steps I and II regardless of their local geometry and stoichiometry. This prediction is consistent with the higher density of  $\text{Pt}^{2+}$  species on ceria surfaces featuring higher step density. Furthermore, it implies that the same square-planar arrangement of  $\text{PtO}_4$  moieties is formed on different nanostructured ceria supports including stepped surfaces and nanoparticles.

The capacity of the {100} sites on nanostructured ceria to anchor atomically dispersed Pt suggests that other transition metals could interact with the  $\text{O}_4$  site of  $\text{Ce}_{40}\text{O}_{80}$  in a similar way. In this respect, the adsorption of metal atoms (M) including the 3d (Fe, Co, Ni, Cu), 4d (Ru, Rh, Pd, Ag) and 5d

(Os, Ir, Pt, Au) metals of groups 8–10 was investigated.<sup>82</sup> The calculated adsorption energies are shown in Fig. 8 in comparison with the calculated adsorption energy of an edge metal atom of a  $\text{M}_{79}$  nanoparticle of the corresponding metal.

The adsorption of the metal atom M at the {100} site results in the oxidation of the adsorbed atom, accompanied by the reduction of  $\text{Ce}^{4+}$  cations to  $\text{Ce}^{3+}$ . In all cases, the adsorption of the metal atom on the  $\text{O}_4$  site of the ceria nanoparticle is stronger than the binding of edge metal atoms in the  $\text{M}_{79}$  models. Interestingly, all calculated oxidation states of metal atoms of groups 8–11 are also observed experimentally in metal–ceria systems.<sup>21,26,65,79,83–97</sup> However, only the metals of group 10 all yield cationic species of the same oxidation state, *i.e.*  $\text{Pt}^{2+}$ ,  $\text{Pd}^{2+}$ , and  $\text{Ni}^{2+}$ . This similarity is associated with the  $d^8$  electronic configuration of the  $\text{M}^{2+}$  cations in the group 10 metals adsorbed in the square planar arrangement. The metals of group 11 adsorbed at the {100} site are found in multiple oxidation states. For instance,  $\text{Cu}^{2+}$  in the square planar coordination is just slightly more stable than the  $\text{Cu}^+$  in a distorted linear arrangement with two short and two long Cu–O distances. Similarly, atomic Ag was found as  $\text{Ag}^+$  or  $\text{Ag}^{3+}$  species. Atomic Au can also be adsorbed as  $\text{Au}^+$  and  $\text{Au}^{3+}$ , with the latter being more stable.

Clear trends emerge along the rows and groups of the periodic table (Fig. 8). Binding energies of M both on the ceria nanoparticle and in the  $\text{M}_{79}$  nanoparticles generally decrease

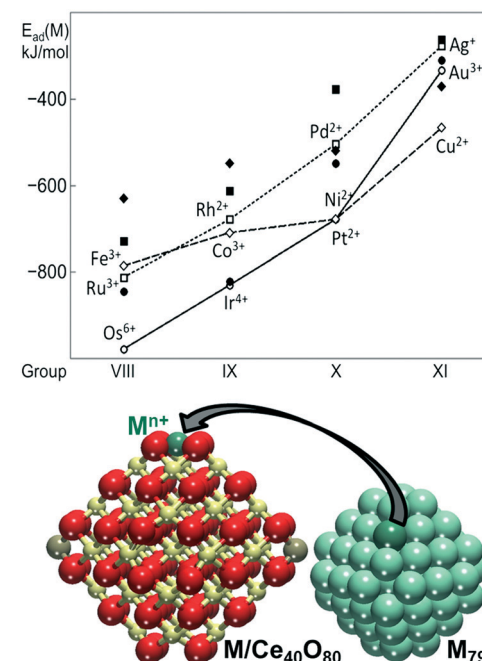


**Fig. 8** Adsorption energies of atomically dispersed 3d (diamonds), 4d (squares), and 5d (circles) metals (M) on the {100} facet of the  $\text{Ce}_{40}\text{O}_{80}$  nanoparticle (empty symbols, connected for guiding the eye) and binding energies of these atoms in edge positions of the  $\text{M}_{79}$  NP (filled symbols). The corresponding  $\text{M}-\text{Ce}_{40}\text{O}_{80}$  and  $\text{M}_{79}$  structures are also shown. Yellow, brown and red spheres represent  $\text{Ce}^{4+}$ ,  $\text{Ce}^{3+}$  and  $\text{O}^{2-}$  ions, respectively. Adapted from ref. 82 with permission from the Royal Society of Chemistry.

in magnitude, when moving from the left to the right of the period. This indicates that metals with less occupied d bands form stronger metal–metal bonds and also bind more strongly to the oxide support. With the exception of Au, 5d metals form the strongest bonds with the O<sub>4</sub> site of ceria, whereas 4d metals form the weakest bonds, with the exception of Ru. Regardless of the overall strength of the interaction of the different metal atoms with the ceria nanoparticle, the resulting adsorption energies indicate that the {100} sites are able to stabilize atomically dispersed species of a wide range of metals.

### 3.2. Stability as a function of noble metal loading

The stability of the ceria supported single atom catalysts is a function of numerous parameters including the metal loading,<sup>98</sup> the structural and chemical environment of the adsorption site,<sup>22</sup> the oxidation state of the substrate, *i.e.* the density of Ce<sup>3+</sup> centers<sup>21</sup> and oxygen vacancies,<sup>89,99</sup> and the ambient atmosphere.<sup>89</sup>

For instance, the adsorption energy of the Pt<sup>2+</sup> species at {100} sites decreases from 7.02 eV to 6.59 eV when the Pt coverage increases from one to four Pt<sup>2+</sup> species per Ce<sub>40</sub>O<sub>80</sub> NP due to the increase of Ce<sup>3+</sup> density.<sup>99</sup> With respect to the limited capacity of the Ce<sub>40</sub>O<sub>80</sub> NP (only 4 Pt atoms can be adsorbed in the form of Pt<sup>2+</sup> since there are only four {100} nanofacets each exposing one O<sub>4</sub> site), the stepped CeO<sub>2</sub>(111) surface allows a higher density of Pt<sup>2+</sup> species to be obtained by assembling PtO<sub>4</sub> units along the steps in close proximity to each other (see Fig. 9).

The maximum coverage of the stable Pt<sup>2+</sup> species at step I-S is 2/3 (Fig. 9a). A further increase of the Pt coverage to 3/3 (1 Pt atom per 1 Ce step edge atom) triggers the nucleation of metallic Pt clusters due to the large strain built up in the long row of interconnected PtO<sub>4</sub> units at the I-S step (Fig. 9b). On step II-S, reduction of Pt<sup>2+</sup> species gives rise to Pt dimers already at coverages exceeding 1/3 (Fig. 9c). In summary, on samples with stoichiometric steps I and II, the calculations predict low Pt<sup>2+</sup> coverage at the steps (<33% of the step-edge sites). In contrast, the calculated maximum coverage of Pt<sup>2+</sup> at the O-rich steps I-O and II-O is 3/3 (Fig. 9e and g), as interconnected assemblies of PtO<sub>4</sub> units fit to the periodicities of both steps I and II (Fig. 7f, g and 9d–g).

The stability of PtO<sub>4</sub> moieties was investigated more quantitatively by evaluating the Gibbs free energy of Pt<sup>2+</sup> adsorbed at the {100} site of a Ce<sub>21</sub>O<sub>42</sub> particle as a function of ambient temperature and partial pressure of oxygen.<sup>89</sup> The relative stability of oxygen vacancies or excess oxygen species evolves progressively with changing pressure and temperature (Fig. 10). Under oxidizing conditions, the adsorption of one oxygen atom in the proximity of the Pt<sup>2+</sup> species is favored and leads to the re-oxidation of two Ce<sup>3+</sup> centers to Ce<sup>4+</sup>. Under reducing conditions, the adsorption energy of the Pt<sup>2+</sup> species at the {100} site decreases with increasing number of oxygen vacancies. At higher temperature, the onset of vacancy formation shifts to higher oxygen pressure and approaches the onset of oxygen adsorption, thus narrowing the region of the Pt<sup>2+</sup> stability.

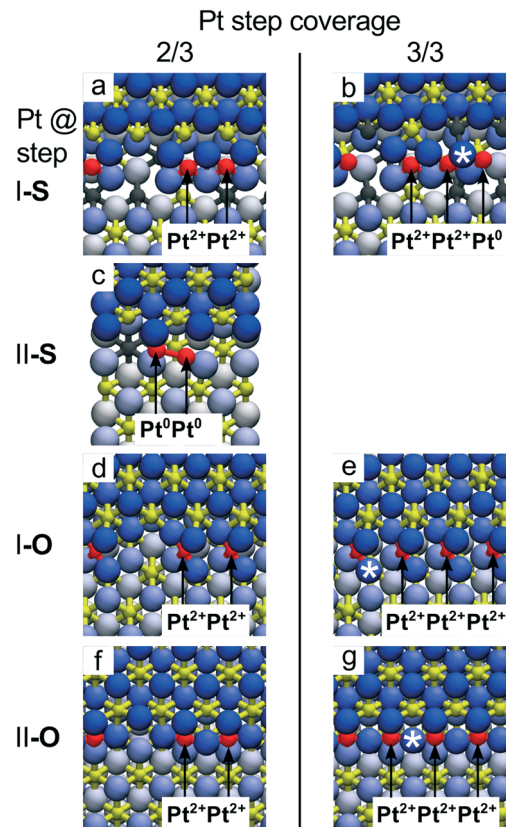


**Fig. 9** Capacity of the CeO<sub>2</sub>(111) step edges to accommodate Pt<sup>2+</sup> ions obtained from DFT calculations. Calculated top views of Pt atoms bound to steps I-S (a and b), II-S (c), I-O (d and e) and II-O (f and g) for Pt step coverage 2/3 (a, c, d and f) and 3/3 (b, e and g). At step I-S, the limiting coverage of Pt<sup>2+</sup> is 2/3 (a), additional Pt attaches to the step edge as Pt<sup>0</sup> (b). At step II-S, the Pt<sup>2+</sup> coverage is 0. Pt atoms attach as weakly ionized Pt<sup>4+</sup> and readily form metallic dimers (c) and clusters. On both steps I-O and II-O, excess oxygen can stabilize ionic Pt<sup>2+</sup> at step edges as single ions appearing isolated or in groups up to 100% step coverage (d–g). Reproduced with permission from ref. 22, Copyright 2016, Nature Publishing Group.

The theoretically predicted behavior of atomically dispersed Pt was examined using appropriate model systems based on well-defined surfaces prepared under UHV conditions.<sup>21,22,98</sup> In particular, Pt<sup>2+</sup> species were prepared either on the surface of nanostructured ceria films<sup>21</sup> or on stepped CeO<sub>2</sub>(111) surfaces.<sup>22</sup> The first approach employed co-deposition of Pt and Ce metal in an oxygen atmosphere onto a well-ordered CeO<sub>2</sub>(111) buffer layer at low temperature. The use of a 1.5 nm thick buffer layer was necessary to minimize the influence of the Cu(111) substrate on the structure of the Pt–CeO<sub>2</sub> film.<sup>100</sup> The procedure yielded three-dimensional Pt–CeO<sub>2</sub> particles with an average diameter of approximately 3 nm and a typical height of around 0.4 nm (see Fig. 11a and b).<sup>21</sup>

After annealing to 700 K, some aggregates reveal a faceted shape, suggesting an epitaxial relationship between the supported Pt–CeO<sub>2</sub> nanoparticles and the CeO<sub>2</sub>(111) buffer layer. The chemical state of Pt in the Pt–CeO<sub>2</sub> film was investigated by means of SRPES with high surface sensitivity. Two



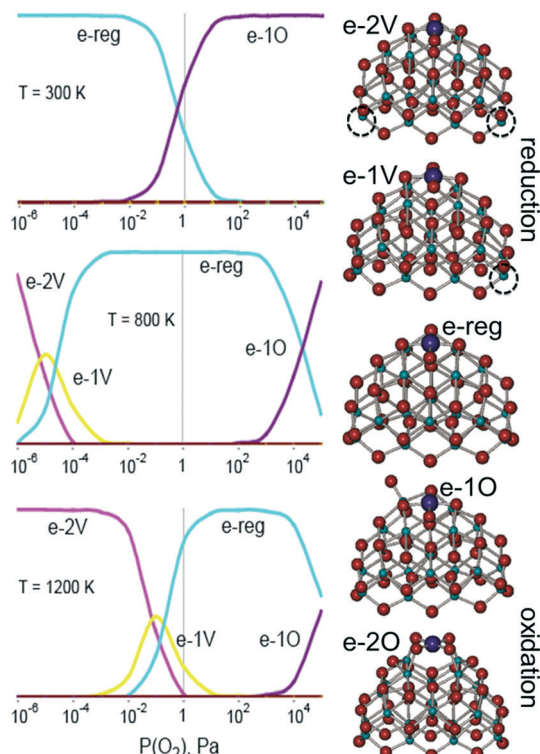


**Fig. 10** Left: results from a general thermodynamic model including a series consisting of the most stable structures of reduced (e-2V and e-1V), stoichiometric (e-reg), and oxidized (e-1O and e-2O)  $\text{PtCe}_{21}\text{O}_{42}$  at three different temperatures. The vertical axis corresponds to the relative concentration of the species ranging from 0 to 100%. Right: structures for the different states considered (dashed circles correspond to the positions of oxygen vacancies). Adapted from ref. 89 with permission from the PCCP Owner Societies.

types of species associated with  $\text{Pt}^{2+}$  and  $\text{Pt}^{4+}$  ions were identified in the  $\text{Pt } 4\text{f}$  spectra obtained from the  $\text{Pt}-\text{CeO}_2$  films as deposited (Fig. 11c and d). In the limit of low Pt loading, the  $\text{Pt}^{2+}$  species in the  $\text{Pt}-\text{CeO}_2$  films demonstrate exceptional thermal stability upon annealing up to 750 K (see Fig. 11c). At the same time, less stable  $\text{Pt}^{4+}$  species were readily converted to  $\text{Pt}^{2+}$ . The critical role of providing the appropriate number of surface sites to anchor Pt becomes evident when the  $\text{Pt}-\text{CeO}_2$  films with higher Pt loading were annealed (Fig. 11d). Consequently, the Pt atoms anchored at less favorable sites are bound too weakly to resist sintering to metallic particles.

In line with the density functional calculations<sup>82</sup> described in section 3.1,  $\text{Pd}^{2+}$  and  $\text{Ni}^{2+}$  species were also anchored on the surface of nanostructured ceria following a similar experimental approach. These films were characterized under similar conditions to the  $\text{Pt}-\text{CeO}_2$  films by means of SRPES (see Fig. 12 and 13, respectively).

The formation of both  $\text{Pd}^{2+}$  and  $\text{Ni}^{2+}$  species was accompanied by additional oxide phases, namely  $\text{PdO}$  and  $\text{NiO}$ , that resulted from the lack of a sufficient number of {100} sites on the nanostructured ceria films (see Fig. 12 and 13). Note that the formation and decomposition of the  $\text{NiO}$  phase can be identified by the presence of two satellite features, *i.e.* I and II in the spectra of  $\text{Ni } 2\text{p}$  in Fig. 13. The abundance of the addi-

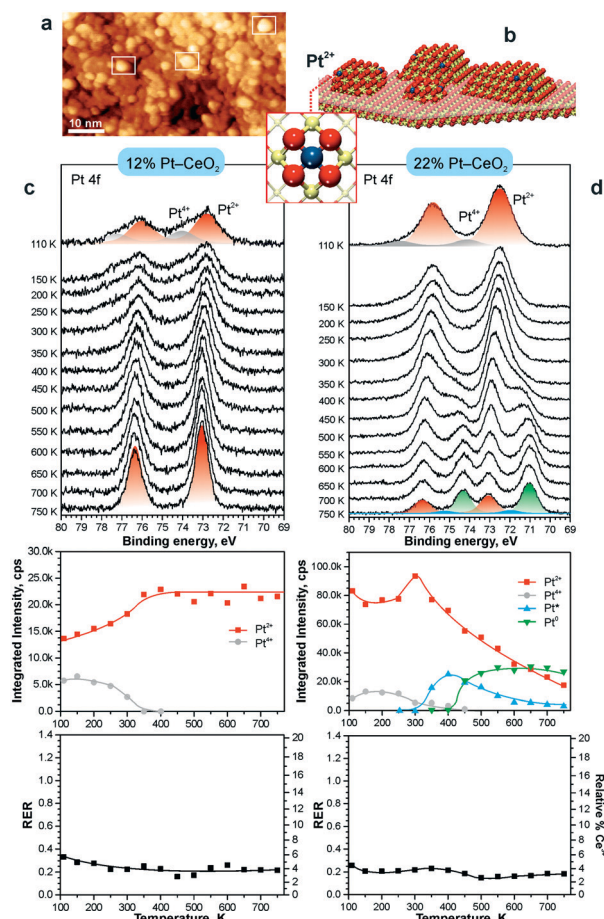


**Fig. 11** a) STM image obtained from  $\text{Pt}-\text{CeO}_2$  nanoparticles supported on the  $\text{CeO}_2(111)$  buffer layer after annealing to 700 K. White rectangles outline faceted  $\text{Pt}-\text{CeO}_2$  particles. b) Schematic structure of the model catalyst. The height of  $\text{Pt}-\text{CeO}_2$  particles is amplified for illustrative purposes. c and d)  $\text{Pt } 4\text{f}$  spectra, the integrated intensities of the surface species, and RER as a function of annealing temperature at a Pt loading of 12% (c) and 22% (d) in the volume of  $\text{Pt}-\text{CeO}_2$  films. The nominal thickness of the  $\text{Pt}-\text{CeO}_2$  films is 0.3 nm.  $\text{Pt } 4\text{f}$  spectra were obtained with a photon energy of 180 eV. (a and b) reproduced from ref. 21 with permission from John Wiley & Sons, Inc. Copyright © 2016 by John Wiley & Sons, Inc. (c and d) Adapted with permission from ref. 98, Copyright 2016, American Chemical Society.

tional phases, *e.g.* oxide and metal particles is a function of metal loading. Thus, in the limit of the low metal loading, the most stable  $\text{Pd}^{2+}$  and  $\text{Ni}^{2+}$  species can be isolated from the less stable oxide phases by annealing in UHV (see Fig. 12a and b and 13a and b). Both  $\text{PdO}$  and  $\text{NiO}$  phases decompose *via* dissolution in the  $\text{CeO}_2(111)$  buffer layer upon annealing.

Higher Pd loading in the films results in a low stability of atomically dispersed  $\text{Pd}^{2+}$  species (see Fig. 12d and e). Similar to the  $\text{Pt}^{2+}$ , atomically dispersed  $\text{Pd}^{2+}$  species are converted into metallic particles upon annealing in UHV.

However, the characteristic difference between the  $\text{Pt}^{2+}$  and  $\text{Pd}^{2+}$  species is that  $\text{Pt}^{2+}$  is preferentially stabilized at the oxygen pockets at the surface, whereas Pd can be stabilized both at the surface and in the bulk in a similar square planar arrangement.<sup>94</sup> This property facilitates the diffusion of  $\text{Pd}^{2+}$  species into the bulk upon annealing. In sharp contrast to



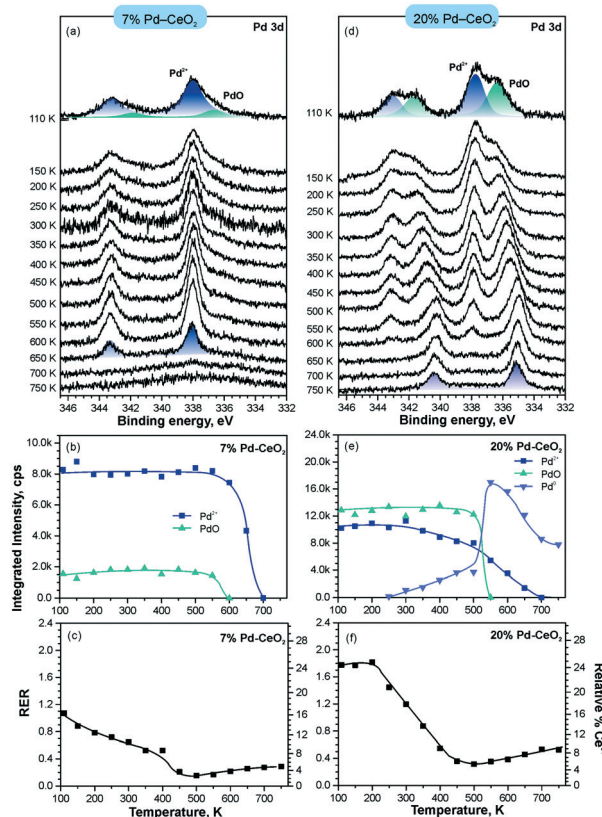


**Fig. 12** Stability of 7% Pd–CeO<sub>2</sub> (a–c) and 20% Pd–CeO<sub>2</sub> (d–f) upon annealing in UHV. Pd 3d spectra (a and d) obtained with  $h\nu = 410$  eV. The integrated intensities of the surface species (b and e) and RER (c and f) on 7% Pd–CeO<sub>2</sub> (a–c) and 20% Pd–CeO<sub>2</sub> (d–f) as a function of temperature. Adapted with permission from ref. 98, Copyright 2016, American Chemical Society.

both Pt–CeO<sub>2</sub> and Pd–CeO<sub>2</sub>, formation of metallic Ni particles was not observed in Ni–CeO<sub>2</sub>, even at high metal loading. This observation is in agreement with the calculated data suggesting that the formation of metallic Ni from ionic Ni<sup>2+</sup> is strongly disfavored energetically.

Interestingly, the atomically dispersed metals of group 10 yielded different concentrations of Ce<sup>3+</sup> centers. This again demonstrates the diversity of mechanisms involved in the anchoring. In contrast to the Pt–CeO<sub>2</sub> films, the Pd–CeO<sub>2</sub> films maintain a considerably higher degree of reduction even at low dopant concentrations.<sup>8</sup> The decomposition of PdO and NiO phases during annealing results in re-oxidation of Ce<sup>3+</sup>.

An alternative approach to form Pt<sup>2+</sup> species involves the deposition of Pt onto stepped CeO<sub>2</sub>(111) surfaces in UHV. Under these conditions, the availability of the adsorption sites capable of anchoring Pt<sup>2+</sup> species is the most critical parameter. The Pt deposition on CeO<sub>2</sub>(111) surfaces with a low density of steps and surface oxygen vacancies (Fig. 14a) yields metallic Pt<sup>0</sup> clusters in combination with ionic Pt<sup>2+</sup> species (Fig. 14b and c).

Subsequent annealing of the films to 700 K increases the amount of Pt<sup>2+</sup> species at the expense of Pt<sup>0</sup>. Interestingly, this process was not accompanied by the reduction of the CeO<sub>2</sub>(111) surface. This implies the involvement of another oxidizing agent such as excess oxygen atoms. In the UHV environment,

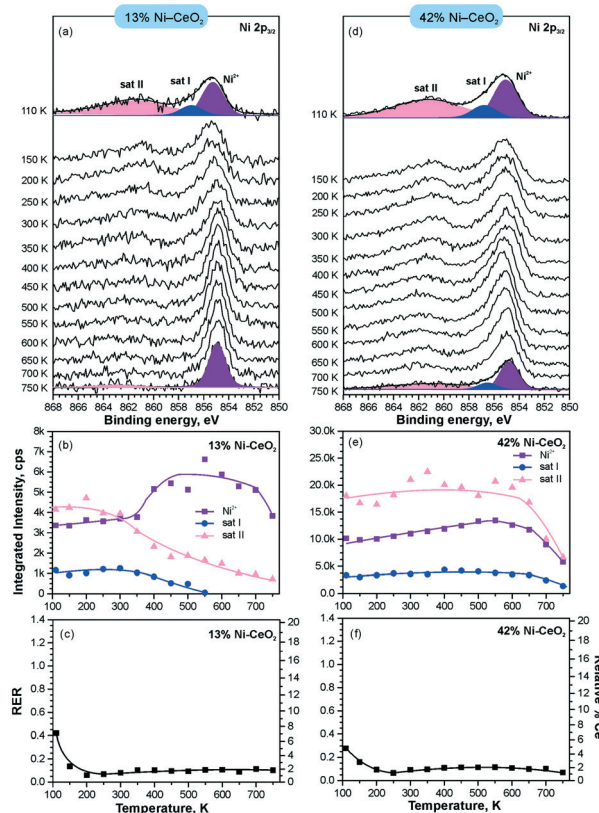


**Fig. 13** Stability of 13% Ni–CeO<sub>2</sub> (a–c) and 42% Ni–CeO<sub>2</sub> (d–f) upon annealing in UHV. Ni 2p<sub>3/2</sub> spectra (a and d) obtained with  $h\nu = 1000$  eV. The integrated intensities of the surface species (b and e) and RER (c and f) on 13% Ni–CeO<sub>2</sub> (a–c) and 42% Ni–CeO<sub>2</sub> (d–f) as a function of temperature. Adapted with permission from ref. 98, Copyright 2016, American Chemical Society.

one possible source of excess oxygen is water adsorbing in sub-monolayer amounts from the background and undergoing dissociation on reduced ceria and Pt/ceria substrates.<sup>101,102</sup> In the real Pt–CeO<sub>2</sub> catalysts, excess O atoms may also be incorporated during the synthesis that proceeds in air.<sup>103,104</sup>

Most importantly, it was found that the relative abundance of the Pt<sup>2+</sup> and Pt<sup>0</sup> species depends on the density of steps and the number of oxygen vacancies in the CeO<sub>2</sub>(111) film. In particular, the amount of Pt<sup>2+</sup> species scales linearly with the step density.

The presence of oxygen vacancies does not promote the dispersion of Pt<sup>2+</sup> species but, instead, leads to the formation of small metallic particles (Fig. 14e and f). According to density functional calculations, oxygen vacancies are not the favorable sites for Pt<sup>2+</sup> formation.<sup>22,89</sup> Based on the analysis of the adsorption energies of Pt, formation of metallic clusters is preferred on reduced ceria nanoparticles.<sup>89</sup>

### 3.3. Identification of the oxidation state of the supported catalyst by CO adsorption

The straightforward identification of Pt sites under reaction conditions is important to understand and tune the structure and stability of Pt–CeO<sub>2</sub> films. CO is commonly used as a

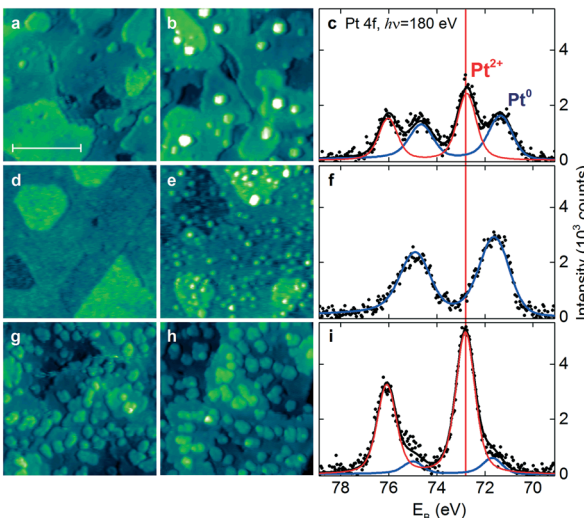


**Fig. 14** STM images (a and b, d–e and g–h) and Pt 4f spectra (c, f and i) obtained from the stepped  $\text{CeO}_2(111)$  surfaces with a low density of surface oxygen vacancies and steps (a–c), a high density of surface oxygen vacancies (d–f), and a high density of steps (g–i) before (a, d and g) and after (b, e and h) Pt deposition in UHV followed by annealing to 700 K. The size of the images is  $45 \times 45 \text{ nm}^2$  and the scale bar is 20 nm. All STM images were obtained with a tunneling current of 25–75 pA and a sample bias voltage of 2.5–3.5 V. Pt 4f spectra were acquired with photon energy  $h\nu = 180 \text{ eV}$ . Reproduced with permission from ref. 22, Copyright 2016, Nature Publishing Group.

probe molecule in combination with infrared absorption spectroscopy (IRAS) for identification of adsorption sites in heterogeneous catalysts.<sup>105–108</sup>

The factors that influence the vibrational frequency of CO adsorbed on Pt particles in Pt– $\text{CeO}_2$  systems include the local structure of the adsorption site (on-top, bridge, and hollow), the oxidation state and coordination number of the Pt adsorption center, the CO coverage, and the stoichiometry of the support.

For instance, the vibrational frequency of CO adsorbed in the on-top configuration on Pt surfaces increases as a function of the coordination number of the Pt atom. The effect was demonstrated for Pt(111) and unsupported Pt particles as well as for ceria-supported Pt particles of different sizes<sup>109,110</sup> (Fig. 15).

As under-coordinated sites have characteristic IRAS fingerprints and the relative number of these sites depends on particle size, the trends derived from Fig. 15 allow estimating particle sizes on the basis of the measured CO vibrational frequencies (and *vice versa*).<sup>111</sup> For example, the size of Pt particles under electrochemical working conditions in Pt–ceria electrocatalysts was determined by comparing the experimental frequency shifts in IRAS with calculated shifts, both on free and ceria-supported Pt particles of varying size.<sup>109</sup>

The calculated vibrational frequencies of CO adsorbed in the on-top configuration on Pt species with different oxidation states and coordination numbers of Pt atoms found in several structural Pt– $\text{CeO}_2$  models<sup>110</sup> are summarized schematically in Fig. 16. A quick inspection of these data reveals a high degree of overlap between CO frequencies calculated

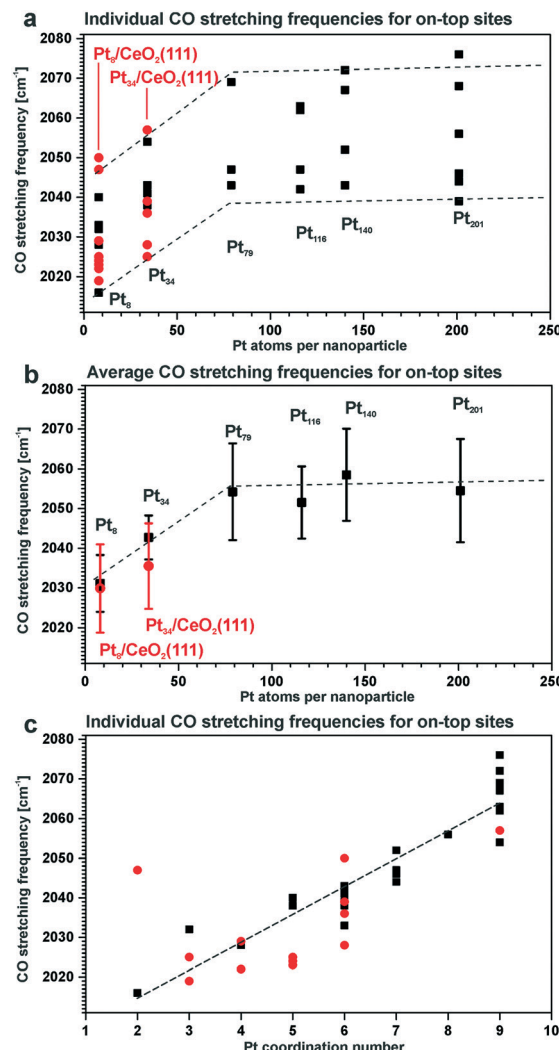


**Fig. 15** Summary of the stretching frequencies calculated by DFT on different on-top sites of each Pt model particle (black, unsupported particles; red, supported particles): (a) CO stretching frequencies on all on-top sites of each particle and the corresponding tendency visualized by the dashed lines; (b) average on-top stretching frequencies and their standard deviation taking into account weights of all on-top sites in each particle; (c) correlation between the CO stretching frequency and the Pt coordination number with respect to neighboring Pt atoms. Reproduced with permission from ref. 109, Copyright 2016, American Chemical Society.

for the different structures. However, general trends indicate that the vibrational frequency of the CO molecule in the on-top configuration depends on the distance between Pt and the nearest oxygen atom of ceria at which the platinum atom is bound to, and that CO vibrational frequencies increase as a function of the oxidation state of atomically dispersed Pt on ceria.<sup>110</sup> In addition, an increase in CO coverage leads to a widening of the CO frequency range for adsorption on supported  $\text{Pt}_8$  clusters and to an increase of the frequency on  $\text{Pt}^{2+}$  species.

This scenario suggests that an assignment of platinum species based exclusively on the vibrational frequency might be misleading or inconclusive. When probing metal species

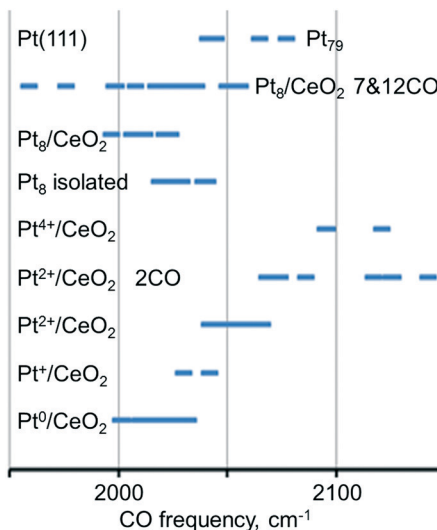


**Fig. 16** Regions of the calculated C–O vibrational frequency for CO adsorbed on-top of neutral and cationic platinum species. Adapted from ref. 110 with permission from the PCCP Owner Societies.

with CO and IRAS, it is therefore necessary to monitor the coverage dependent changes in the spectra carefully. In addition, it appears that the adsorption energy of CO is a critical parameter. For example, the adsorption of CO on the  $\text{Pt}^{2+}$  cation of the  $\text{PtO}_4$  moiety is rather weak ( $-0.61$  eV) and also involves a significant reconstruction, suggesting that this is an activated and not very favorable process. Similarly, the vibrational frequency calculated for CO adsorption on  $\text{Pt}^{4+}$  comes from a rather unstable system, where excess O atoms have been added to obtain the  $\text{Pt}^{4+}$  state. This model is probably not very representative of sites one would find in experiments on Pt–ceria systems, but it is nevertheless useful as a tool to explore how the CO frequency changes with the oxidation state of Pt. CO does not adsorb under pertinent experimental conditions on  $\text{Pt}^{2+}$  and  $\text{Pt}^{4+}$  species based on the calculated stability of the resulting adsorption complexes.

As a complementary tool, SRPES allows direct determination of the oxidation state of Pt as well as the adsorption site of molecular surface species. The changes in the oxidation state of atomically dispersed Pt species caused by annealing in UHV were reliably identified from their Pt 4f spectra.<sup>112</sup> In particular, comparison of the intensities of the Pt 4f spectra before and after CO adsorption at 110 K indicated the presence of metallic Pt clusters which served as adsorption sites for CO.

The development of the Pt 4f spectra obtained from  $\text{Pt-CeO}_2$  films with different Pt loadings are shown in Fig. 17. CO adsorption on the surfaces containing  $\text{Pt}^{2+}$  and  $\text{Pt}^{4+}$  exclusively does not attenuate the corresponding contributions (I–II) in the Pt 4f spectra. This suggests that neither  $\text{Pt}^{2+}$  nor  $\text{Pt}^{4+}$  serve as adsorption sites for CO in line with the calculated instability of CO on these sites. In contrast, small metallic Pt particles formed at high Pt loading (see Fig. 17c) readily adsorb CO. The emergence of metallic particles yielded distinct differences between Pt 4f spectra before (black) and after (green) CO adsorption (Fig. 17). In particu-

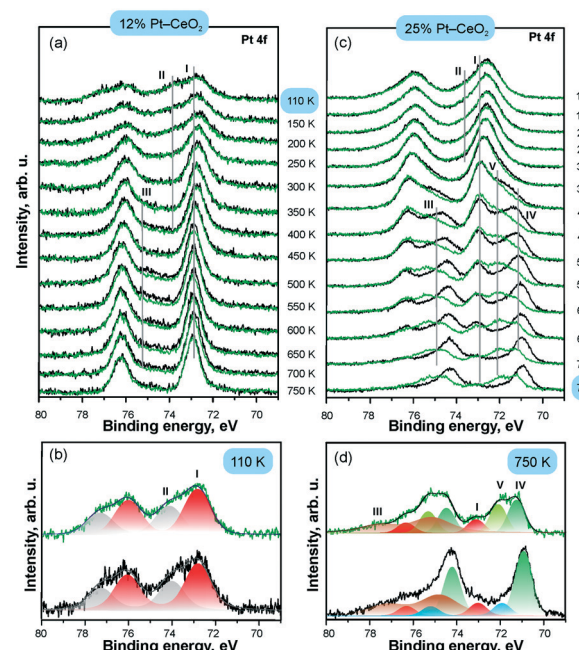


**Fig. 17** Pt 4f spectra obtained from 12%  $\text{Pt-CeO}_2$  (a and b) and 25%  $\text{Pt-CeO}_2$  (c and d) films prepared at 110 K on  $\text{CeO}_2(111)/\text{Cu}(111)$  annealed at different temperatures (black) and exposed to 50 L of CO at 110 K (green); the structure of the Pt 4f spectra on as-prepared 12%  $\text{Pt-CeO}_2$  at 110 K (b) and 25%  $\text{Pt-CeO}_2$  films annealed to 750 K (d); the components labelled I–V arise from  $\text{Pt}^{2+}$ ,  $\text{Pt}^{4+}$ , Cu 3p, and metallic Pt particles (IV–V), respectively. Adapted from ref. 112 with permission from the PCCP Owner Societies.

lar, the contribution from metallic Pt (IV) in the Pt 4f spectra is attenuated and a new component (V) emerges in the Pt 4f spectra upon CO adsorption. Peak V is identified as a shifted component of peak IV, which is consistent with the core level shift expected upon CO adsorption on metallic Pt.

The development of the C 1s spectra upon CO adsorption on  $\text{Pt-CeO}_2$  films with different Pt loadings is shown in Fig. 18 in comparison with the Pt-free nanostructured  $\text{CeO}_2$  film. The C 1s spectra reveal the presence of CO-derived species on the three films. The dominant species formed on all surfaces are tridentate (A) and bidentate (B) carbonates. The emergence of the second tridentate carbonate (C) and carbonite (D) contributions indicates the presence of oxygen vacancies in the films. The formation of carbonite species is not associated with the formation of the tridentate carbonate species at oxygen vacancies (C) suggesting that the two species are formed at structurally different types of oxygen vacancies.

The emergence of a wide range of adsorbed molecular surface species including carbonates, carbonites, and formates, whose stability and spectroscopic signatures strongly depend on the structure and oxidation state of the adsorption site is in line with the results of DFT studies of CO adsorption on a  $\text{Ce}_{21}\text{O}_{42}$  particle.<sup>113</sup>

The changes in the relative abundance of species A–D in Fig. 18 are consistent with restructuring of the films upon annealing. The morphological changes induced by the

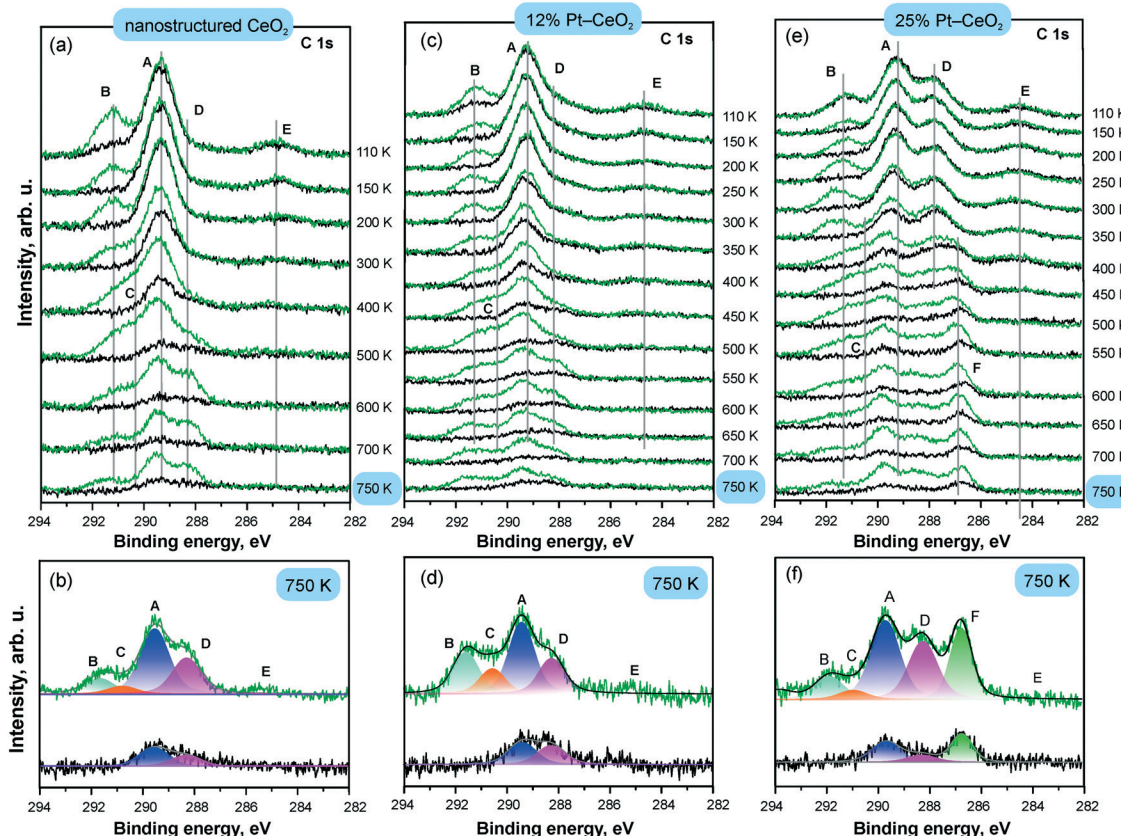


**Fig. 18** C 1s spectra obtained from Pt-free nanostructured  $\text{CeO}_2$  (a and b), 12%  $\text{Pt}-\text{CeO}_2$  (c and d), and 25%  $\text{Pt}-\text{CeO}_2$  (e and f) films prepared at 110 K on  $\text{CeO}_2(111)/\text{Cu}(111)$  annealed at different temperatures (black) and exposed to 50 L of CO at 110 K (green); the structure of the C 1s spectra obtained from Pt-free nanostructured  $\text{CeO}_2$  (b), 12%  $\text{Pt}-\text{CeO}_2$  (d), and 25%  $\text{Pt}-\text{CeO}_2$  film (f) annealed to 750 K before (black) and after CO adsorption (green). The components labelled A–F arise from tridentate (A and C) and bidentate carbonates (B), carbonite (D), atomic carbon (E), and CO adsorption on metallic Pt particles (F). Adapted from ref. 112 with permission from the PCCP Owner Societies.

annealing of the 12% and 25%  $\text{Pt}-\text{CeO}_2$  mixed oxides are similar to the changes of the Pt-free  $\text{CeO}_2$  film and occur above 300 K. The observed reduction of  $\text{Pt}^{2+}$  to metallic Pt particles on the 25%  $\text{Pt}-\text{CeO}_2$  film is also associated with restructuring causing a decrease in the number of stable sites that can anchor  $\text{Pt}^{2+}$  species. The presence of metallic Pt can therefore be identified by both Pt 4f and C 1s spectra. The appearance of metallic Pt features in the Pt 4f spectra is concomitant with the appearance of a C 1s feature (F) corresponding to CO in the on-top configuration.

## 4. Reactivity of supported single atom catalysts towards $\text{H}_2$

### 4.1. Supported single metal atoms in the absence of metal particles

Dissociation of molecular hydrogen is the major function of the anode catalyst in hydrogen powered PEMFCs. It was reported that surface cationic Pt species promote dissociation of  $\text{H}_2$  and facilitate hydrogen spillover on Pt-doped  $\text{CeO}_2$  powders prepared by the solution combustion method.<sup>114</sup> The origins of this reactivity, however, remained obscure.

One of the reasons is that the role of atomically dispersed  $\text{Pt}^{2+}$  on  $\text{CeO}_2$  had not been studied individually, *i.e.* in the absence of other active species such as  $\text{Pt}^{4+}$ ,  $\text{Pt}^0$ , and oxygen vacancies.<sup>114–116</sup> Using well-defined model catalysts, atomically dispersed  $\text{Pt}^{2+}$  species can be prepared and studied individually.<sup>21,99</sup> The corresponding approach involves the preparation of  $\text{Pt}-\text{CeO}_2$  films with low Pt loading at low temperature followed by brief annealing to 700 K.<sup>21</sup> The same procedure allows the preparation of atomically dispersed  $\text{Pd}^{2+}$  and  $\text{Ni}^{2+}$  species on nanostructured ceria.<sup>98</sup> Thus, the reactivity of atomically dispersed  $\text{Pt}^{2+}$ ,  $\text{Pd}^{2+}$ , and  $\text{Ni}^{2+}$  species can be investigated under identical experimental conditions.

Changes in the oxidation states of  $\text{Pt}^{2+}$ ,  $\text{Pd}^{2+}$ , and  $\text{Ni}^{2+}$  species upon reaction with  $\text{H}_2$  were investigated by means of SRPES with high surface sensitivity under UHV conditions (see Fig. 19). Additionally, the oxidation state of Ce cations was monitored by means of resonant photoemission spectroscopy (RPES). The resonant enhancement ratio (RER) scales with the  $\text{Ce}^{3+}/\text{Ce}^{4+}$  concentration ratio.<sup>117</sup>

Based on the analysis of the corresponding Pt 4f, Pd 3d, and Ni 2p core level spectra and the RER in Fig. 19, it was concluded that isolated  $\text{Pt}^{2+}$ ,  $\text{Pd}^{2+}$ , and  $\text{Ni}^{2+}$  species do not facilitate dissociation of molecular hydrogen under the

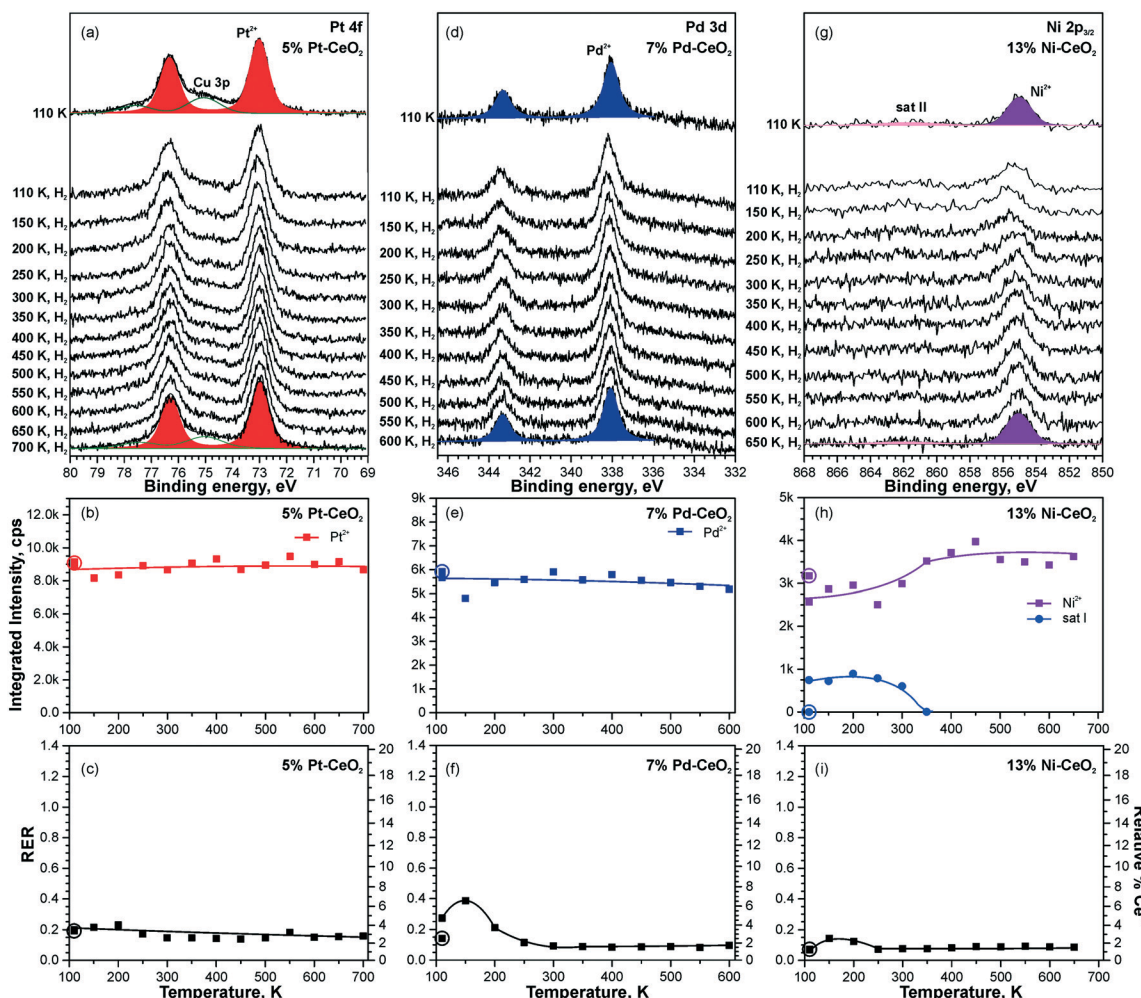


**Fig. 19** Reactivity of 5% Pt–CeO<sub>2</sub> (a–c), 7% Pd–CeO<sub>2</sub> (d–f), and 13% Ni–CeO<sub>2</sub> (g–i) films towards hydrogen activation. The samples were briefly annealed at 700 K (5% Pt–CeO<sub>2</sub>, 13% Ni–CeO<sub>2</sub>) or 600 K (7% Pd–CeO<sub>2</sub>). Pt 4f (a), Pd 3d (d), and Ni 2p<sub>3/2</sub> (g) spectra obtained with  $h\nu = 180$  eV,  $h\nu = 410$  eV, and  $h\nu = 1000$  eV, respectively. The integrated intensities of the surface species (b, e and h) and RER (c, f and i) on 5% Pt–CeO<sub>2</sub> (b and c), 7% Pd–CeO<sub>2</sub> (e and f), and 13% Ni–CeO<sub>2</sub> (h and i) following the exposure to 50 L of H<sub>2</sub> as a function of temperature. The data points obtained prior to the hydrogen exposure are circled. (a–c) Reproduced from ref. 99 with permission from the PCCP Owner Societies. (d–i) Adapted with permission from ref. 98. Copyright 2016, American Chemical Society.

experimental conditions employed, since reduction of neither these metal cations nor Ce<sup>4+</sup> ones by H<sub>2</sub> has been detected.<sup>98,99</sup>

This experimental finding was corroborated by DFT calculations for the case of ceria supported Pt<sup>2+</sup> species.<sup>99</sup> The reaction pathways and the energetics for H<sub>2</sub> dissociation on the Pt–CeO<sub>2</sub> system and the CeO<sub>2</sub>(111) surface are compared in Fig. 20.

The Pt–CeO<sub>2</sub> system was modeled as a low-energy vicinal surface exposing CeO<sub>2</sub>(111) terraces and step edges along the [110] direction accommodating Pt<sup>2+</sup> ions. These calculations showed that the barrier for H<sub>2</sub> dissociation at the Pt<sup>2+</sup> sites (1.2 eV) is even larger than the barrier for dissociation on the pristine CeO<sub>2</sub>(111) surface (1.0 eV).<sup>99</sup> The rather high H<sub>2</sub> activation energy is consistent with a very high thermodynamic stability of the Pt<sup>2+</sup> species.<sup>21</sup> This implies that the low barrier desorption of weakly adsorbed H<sub>2</sub> is strongly favored over dissociation, in accordance with the experimental findings.<sup>99</sup>

In contrast to isolated Pt<sup>2+</sup> species, DFT simulations show that sub-nanometer Pt clusters supported on ceria are highly active for H<sub>2</sub> dissociation. For instance, the calculated activation energy of only ~0.3 eV (Fig. 20, green line) for Pt<sub>6</sub> on CeO<sub>2</sub>(111) could be easily overcome even at room temperature.<sup>99</sup>

#### 4.2. Supported single atom catalysts with traces of metallic clusters

Higher levels of metal loading in Pt–CeO<sub>2</sub> and Pd–CeO<sub>2</sub> films yield metallic particles upon annealing<sup>98</sup> (Fig. 21a and d). In contrast, no metallic Ni was detected in Ni–CeO<sub>2</sub> films despite the high metal loading (Fig. 21g).

The activation of molecular hydrogen becomes strongly favored in the presence of metallic Pt and Pd particles on Pt–CeO<sub>2</sub> and Pd–CeO<sub>2</sub> films. The process is accompanied by the reduction of Pt<sup>2+</sup> and Pd<sup>2+</sup> species coupled with the reduction

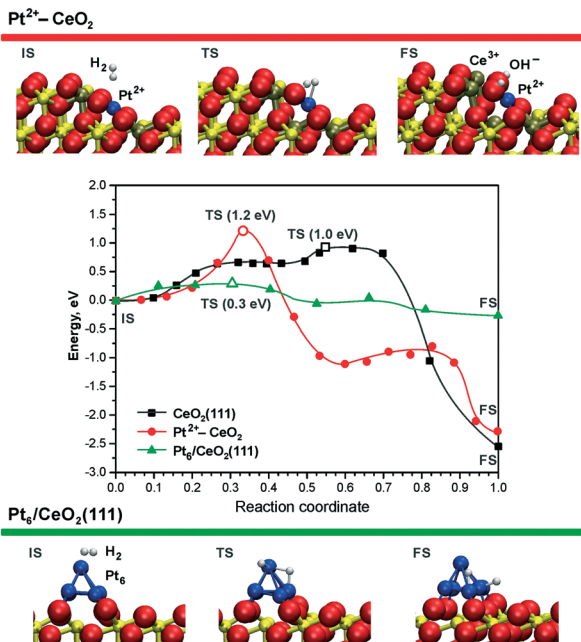


**Fig. 20** Minimum energy paths for  $\text{H}_2$  dissociation on the pristine  $\text{CeO}_2(111)$  surface (black), on the ionic  $\text{Pt}^{2+}$  sites (red), and on the supported  $\text{Pt}_6$  cluster (green) – middle panel. The top and bottom panels display the initial (IS), transition (TS), and final (FS) states of  $\text{H}_2$  dissociation on the  $\text{Pt}^{2+}\text{-CeO}_2$  and  $\text{Pt}_6/\text{CeO}_2(111)$  systems. The activation energies in TS states (open symbols) are given in parentheses.  $\text{Ce}^{4+}$ ,  $\text{Ce}^{3+}$ , and  $\text{O}^{2-}$  ions are displayed as yellow, brown, and red spheres, respectively. Reproduced from ref. 99 with permission from the PCCP Owner Societies.

of  $\text{Ce}^{4+}$  at elevated temperatures (Fig. 21). Eventually, all  $\text{Pt}^{2+}$  and  $\text{Pd}^{2+}$  species are reduced quantitatively to metallic  $\text{Pt}^0$ . Remarkably, very small amounts of metallic Pt (the traces hardly detected by conventional XPS) turned out to be sufficient to initiate  $\text{H}_2$  dissociation under similar conditions.<sup>99</sup>

In contrast to the  $\text{Pt-CeO}_2$  and  $\text{Pd-CeO}_2$  films, no reactivity towards  $\text{H}_2$  was observed on the  $\text{Ni-CeO}_2$  mixed oxide regardless of the Ni loading. The reason is the particularly high stability of the  $\text{Ni}^{2+}$  state preventing formation of metallic Ni.<sup>98</sup> In order to probe the role of metallic Ni in hydrogen activation, small amounts of metallic Ni were deposited onto  $\text{Ni-CeO}_2$  films in UHV.<sup>98</sup> However, annealing of the film containing metallic  $\text{Ni}^0$  in hydrogen at 600 K did not yield a detectable change of the oxidation state of Ni. Apparently, the reaction sequence leading to reduction of cationic Pd and Pt species in  $\text{Pd-CeO}_2$  and  $\text{Pt-CeO}_2$  films is not possible for  $\text{Ni-CeO}_2$ , even in the presence of metallic Ni. Besides the high stability of  $\text{Ni}^{2+}$ , a reason for the low reactivity could be that annealing of the Ni particles on  $\text{Ni-CeO}_2$  triggers the formation of a  $\text{NiO}$  capping layer. Such encapsulation processes of the metallic Ni particles could prevent the dissociation of hydrogen.

Overall, the  $\text{Pt-CeO}_2$  and  $\text{Pd-CeO}_2$  films show a very similar reactivity towards  $\text{H}_2$ . Therefore, the mechanisms of hydrogen activation on both  $\text{Pd-CeO}_2$  and  $\text{Pt-CeO}_2$  films are expected to be similar. With respect to the reduction of atomically dispersed Pt-group species, density functional model-

ling suggests that hydroxylation of the  $\text{Pt-O}_4$  moieties upon adsorption of atomic hydrogen<sup>21</sup> leads to the reduction of  $\text{Ce}^{4+}$  cations and may result in destabilization and, possibly, reduction of  $\text{Pt}^{2+}$  species. In the presence of metallic  $\text{Pt}^0$  on  $\text{Pt-CeO}_2$ , atomic hydrogen could spillover from Pt particles onto the support, leading to hydroxylation of the  $\text{Pt-O}_4$  moiety. In fact, the calculated reaction pathway on  $\text{Pt}_6/\text{CeO}_2$  (Fig. 20) suggests the tendency of H to migrate to the cluster periphery and accumulate at the boundary in contact with the oxide support.<sup>99</sup> However, this pathway was ruled out based on the insignificant changes in the RER at temperatures where hydrogen reverse spillover processes are typically observed,<sup>118</sup> *i.e.* between 190 and 260 K (see Fig. 21c and f). This suggests that hydrogen spillover and hydroxylation of the  $\text{PtO}_4$  moiety are not the key steps in  $\text{Pt}^{2+}$  reduction during the reaction with  $\text{H}_2$ .

Thus, the mechanism of  $\text{H}_2$  dissociation involving  $\text{Pt}^{2+}$  reduction is likely to be associated with the formation of oxygen vacancies upon reverse oxygen spillover<sup>119</sup> from  $\text{Pt-CeO}_2$  to the Pt particles. Upon exposure to  $\text{H}_2$  the spilt-over oxygen is continuously removed from the Pt particles by reaction with hydrogen and subsequent formation of water. This reaction channel leads to the formation of oxygen vacancies accompanied by the reduction of  $\text{Ce}^{4+}$ .

## 5. Redox conversion of atomically dispersed species to sub-nanometer particles

### 5.1. The role of oxygen vacancies

Density functional calculations show that the formation of oxygen vacancies can notably lower the adsorption energy of dispersed Pt on the ceria nanoparticles (Fig. 22). The energetic stability of the  $\text{Pt}^{2+}$  species depends on the proximity of the oxygen vacancies, their number, the  $\text{Pt}^{2+}$  concentration, and the distribution of  $\text{Ce}^{3+}$  ions.<sup>99</sup> Reduction of  $\text{Pt}^{2+}$  species is expected once the adsorption energy of atomic Pt falls below the bulk cohesive energy of Pt ( $-5.85$  eV (ref. 120)).

The formation of a single oxygen vacancy outside the  $\text{PtO}_4$  moiety (Fig. 22a) is not sufficient to initiate the reduction of a  $\text{Pt}^{2+}$  cation. In contrast, removal of one oxygen atom directly from the  $\text{PtO}_4$  moiety lowers the adsorption energy  $\text{Pt}^{2+}$  species strongly and triggers the reduction, followed by release of Pt from the resulting  $\text{Pt-O}_3$  moiety. However, the vacancy formation is strongly disfavored at the pocket sites in the presence of  $\text{Pt}^{2+}$  species, rendering such a process rather unlikely.<sup>99</sup> This suggests that oxygen vacancies are preferentially formed outside the  $\text{Pt-O}_4$  moiety. If two such oxygen vacancies are created per  $\text{Pt}^{2+}$  ion, the  $\text{Pt}^{2+}$  adsorption energy falls well below the cohesive energy (Fig. 22b). Thus, density functional calculations indicate that the onset of  $\text{Pt}^{2+}$  reduction occurs when approximately two oxygen vacancies are created per  $\text{Pt}^{2+}$  site.

A rough estimation of the ratio between the concentration of oxygen vacancies and the  $\text{Pt}^{2+}$  cations at the onset of  $\text{Pt}^{2+}$

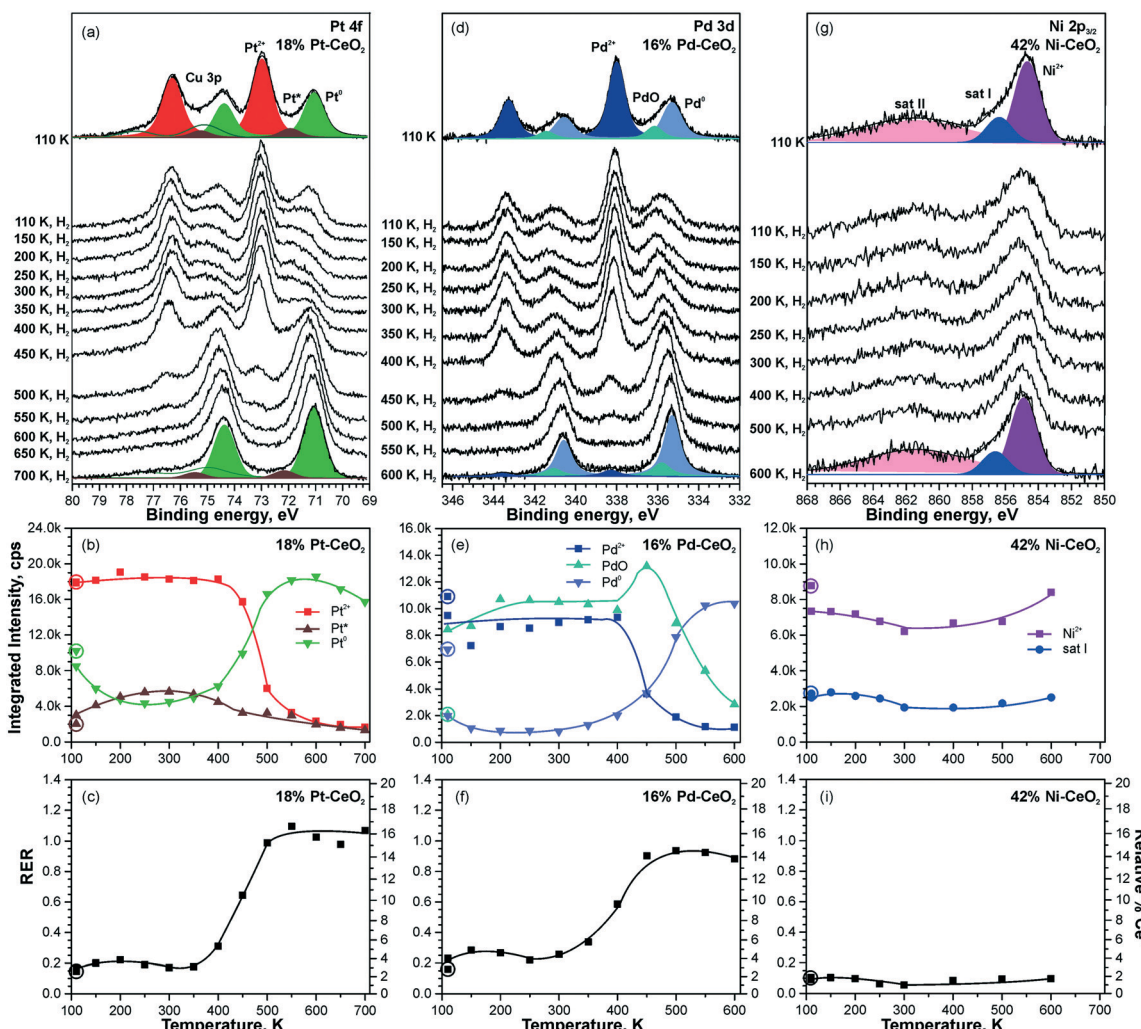


**Fig. 21** Reactivity of 18% Pt-CeO<sub>2</sub> (a–c), 16% Pd-CeO<sub>2</sub> (d–f), and 42% Ni-CeO<sub>2</sub> (g–i) films towards hydrogen activation. The samples were briefly annealed at 700 K (18% Pt-CeO<sub>2</sub>, 42% Ni-CeO<sub>2</sub>) or 600 K (16% Pd-CeO<sub>2</sub>). Pt 4f (a), Pd 3d (d), and Ni 2p<sub>3/2</sub> (g) spectra obtained with  $h\nu = 180$  eV,  $h\nu = 410$  eV, and  $h\nu = 1000$  eV, respectively. The integrated intensities of the surface species (b, e and h) and RER (c, f and i) on 18% Pt-CeO<sub>2</sub> (b and c), 16% Pd-CeO<sub>2</sub> (e and f), and 42% Ni-CeO<sub>2</sub> (h and i) following the exposure to 50 L of H<sub>2</sub> as a function of temperature. The data points obtained prior to the hydrogen exposure are circled. (a–c) Reproduced from ref. 99 with permission from the PCCP Owner Societies; (d–i) adapted with permission from ref. 98, Copyright 2016, American Chemical Society.

reduction could be obtained also from experimental data.<sup>99,121</sup> For the Pt-CeO<sub>2</sub> film, the corresponding ratio for reduction of Pt<sup>2+</sup> to Pt with hydrogen was determined to be about 1.5 O vacancies per Pt<sup>2+</sup> cation.

The direct involvement of metallic Pt particles in the reduction of Pt<sup>2+</sup> species can be ruled out by using methanol as a reducing agent.<sup>121</sup> The decomposition of methanol on CeO<sub>2</sub> films involves the formation of formaldehyde, CO, and oxygen vacancies.<sup>122–124</sup> Therefore, the reduction of Pt<sup>2+</sup> species is observed as a consequence of the formation of oxygen vacancies regardless of the Pt loading (see Fig. 23). The estimation of the number of oxygen vacancies at the onset of Pt<sup>2+</sup> reduction suggested that the formation of two oxygen vacancies is required for reduction of one Pt<sup>2+</sup> species.<sup>121</sup> This agrees with results of density functional calculations.<sup>99</sup> Also, a good correspondence of the ratio between the number of O vacancies and the number of reduced Pt<sup>2+</sup> species determined in the

presence and in the absence of metallic Pt particles rules out a direct involvement of Pt particles in the destabilization of Pt<sup>2+</sup>.

Notably, the reduction of Pt<sup>2+</sup> species on the Pt-CeO<sub>2</sub> film yields two types of metallic Pt, labeled as Pt<sup>0</sup> and Pt<sup>\*</sup> (see Fig. 23). The different binding energies are associated with differences in particle sizes. Based on the value of the binding energy in the Pt 4f spectra, the particle size for the Pt<sup>\*</sup> components falls into the sub-nanometer range (less than 25 Pt atoms per particle) while the Pt<sup>0</sup> signal corresponds to “regular” nanoparticles with a size above 2 nm.<sup>117</sup>

As one would expect, the formation of sub-nanometer Pt particles precedes the formation of larger Pt<sup>0</sup> particles. The stability of the sub-nanometer Pt<sup>\*</sup> particles strongly depends on the Pt loading in the Pt-CeO<sub>2</sub> films. In the presence of Pt<sup>0</sup> particles, Pt<sup>\*</sup> particles are rapidly lost by sintering and coalescence with Pt<sup>0</sup> particles.



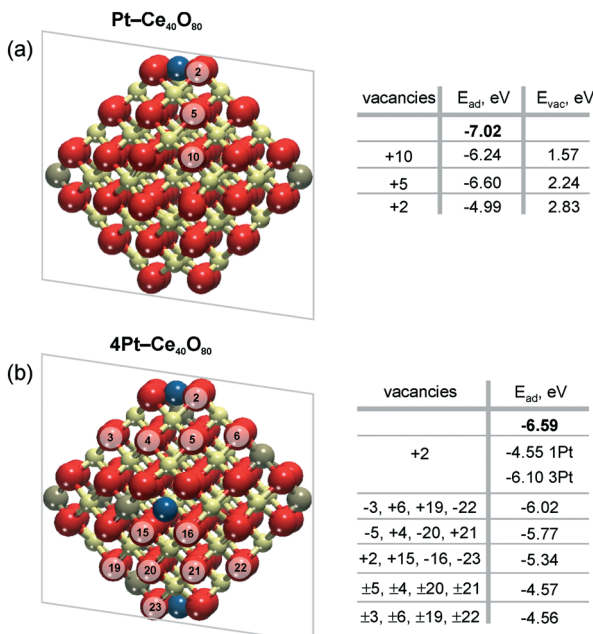


**Fig. 22** Adsorption energies of atomic Pt in the 2+ state,  $E_{ad}$ , without ( $n = 0$ ) and with  $n$  ( $n > 0$ ) oxygen vacancies on a)  $\text{Pt-Ce}_{40}\text{O}_{80-n}$  and b)  $4\text{Pt-Ce}_{40}\text{O}_{80-n}$  nanoparticle models.  $E_{ad}$  values calculated in the absence of oxygen vacancies are shown in bold. The transparent planes cut the nanoparticles into two halves. The vacancies with the signs “+” and “-” are located in front of and behind the planes, respectively. The sign “±” indicates two symmetric oxygen vacancies located in front of and behind the transparent planes. For the  $4\text{Pt-Ce}_{40}\text{O}_{80-n}$  nanoparticle (b), the formation of one oxygen vacancy at the position +2 leads to a significant decrease of  $E_{ad}$  of one  $\text{Pt}^{2+}$  in the proximity of the vacancy (1Pt) while the remaining three  $\text{Pt}^{2+}$  species (3Pt) are influenced less significantly. Formation energies of oxygen vacancies,  $E_{vac}$ , in the  $\text{Pt-Ce}_{40}\text{O}_{80}$  model (a) were calculated with respect to  $\frac{1}{2}$  of the energy of the  $\text{O}_2$  molecule. Reproduced from ref. 99 with permission from the PCCP Owner Societies.

In the absence of  $\text{Pt}^0$  particles, however, the sub-nanometer  $\text{Pt}^*$  particles show remarkable stability upon annealing even under strongly reducing conditions (see Fig. 23a).

Due to the high binding energy of the  $\text{Pt}^*$  contribution in the  $\text{Pt 4f}$  spectra (72.0 eV), the metallic nature of sub-nanometer  $\text{Pt}^*$  particles is difficult to prove.<sup>98,99</sup> For example, the presence of a  $\text{PtO}$  phase or the adsorption of CO on Pt gives rise to spectral contributions at similar binding energies.<sup>112,125</sup> Therefore, it is instructive to compare the trends in the formation of oxygen vacancies on  $\text{Pt-CeO}_2$  films with different Pt loadings with respect to the Pt-free  $\text{CeO}_2$  film during reaction with methanol (see Fig. 24). The nearly linear increase of the RER on the Pt-free  $\text{CeO}_2$  film indicates the formation of oxygen vacancies resulting from desorption of formaldehyde, CO, and water that involves partial removal of lattice oxygen from ceria.<sup>122–124</sup> In the presence of metallic Pt particles, however, a second channel opens that involves reverse hydrogen spillover followed by desorption of molecular hydrogen.<sup>118</sup>

This process is accompanied by re-oxidation of ceria. As a result, the amount of the oxygen vacancies formed in the

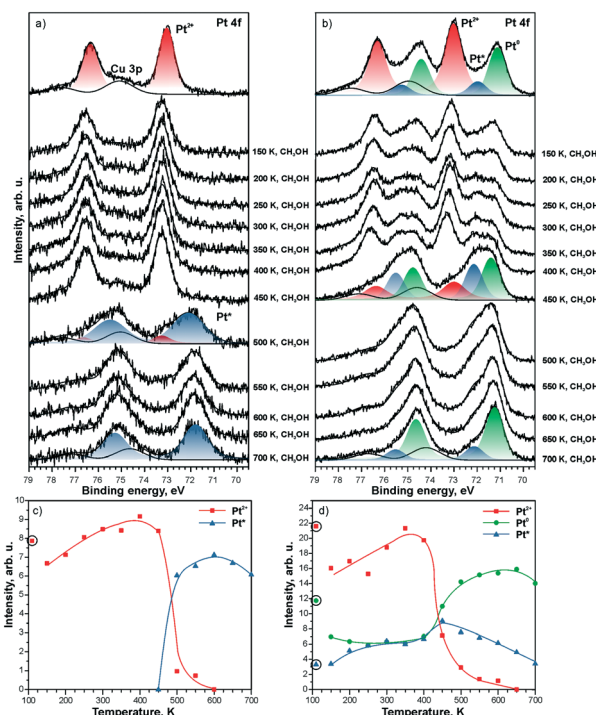


**Fig. 23** Pt 4f spectra obtained from a) 5%  $\text{Pt-CeO}_2$  and b) 18%  $\text{Pt-CeO}_2$  films (top spectra) after annealing while exposing to methanol (10 L) between 150 and 700 K. The Cu 3p signal originates from the underlying Cu(111) substrate. The spectra were acquired with a photon energy of 180 eV. Integrated intensities of  $\text{Pt}^{2+}$ ,  $\text{Pt}^0$ , and  $\text{Pt}^*$  species on c) 5%  $\text{Pt-CeO}_2$  and d) 18%  $\text{Pt-CeO}_2$  films are shown as a function of temperature during annealing under methanol exposure. The circled data points were obtained prior to the methanol exposure. Reprinted from ref. 121, Copyright 2016, with permission from Elsevier.

presence of Pt particles is lowered. The limited density of oxygen vacancies in the presence of the Pt particles is reflected by the RER which shows saturation with increasing temperature. Notably, the formation of vacancies is limited on both  $\text{Pt-CeO}_2$  films regardless of the Pt loadings. This suggests the

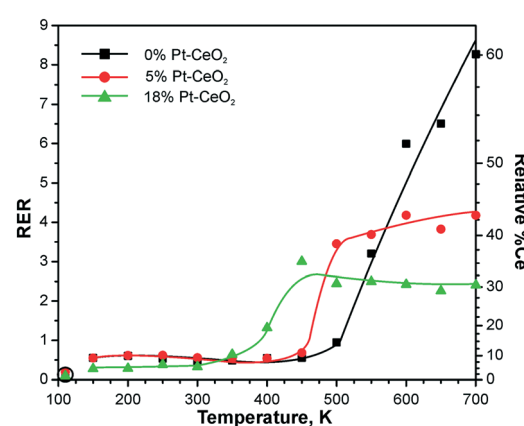


**Fig. 24** RERs on 0%  $\text{Pt-CeO}_2$  (black), 5%  $\text{Pt-CeO}_2$  (red), and 18%  $\text{Pt-CeO}_2$  (green) films as a function of the temperature during annealing under exposure to methanol (10 L). The data points indicated by circles were obtained prior to the methanol exposure. Reprinted from ref. 121, Copyright 2016, with permission from Elsevier.

presence of metallic Pt on all Pt–CeO<sub>2</sub> films and corroborates the assignment of the Pt\* component to sub-nanometer Pt particles. It can be concluded that the formation of stable sub-nanometer Pt particles is possible *via* preparation of stable atomically dispersed Pt<sup>2+</sup> species followed by their reduction. A similar preparation strategy was employed to obtain finely dispersed Pt particles *via* Pt segregation from Pt-doped ceria.<sup>126</sup>

## 5.2. Redox coupling with the reducing agent

The relationship between the formation of oxygen vacancies and stability of the Pt<sup>2+</sup> species<sup>99,121</sup> enables new methods to prepare thermally stable sub-nanometer Pt particles.<sup>127</sup> Since the formation of oxygen vacancies in ceria-based materials leads to reduction of Ce<sup>4+</sup> to Ce<sup>3+</sup>,<sup>123,128,129</sup> one could speculate that reduction of Pt<sup>2+</sup> could be controlled *via* the formation of Ce<sup>3+</sup> centers.

Following this idea, the reduction of Pt<sup>2+</sup> species in Pt–CeO<sub>2</sub> materials might be triggered by addition of reducing agents

which do not involve the removal of oxygen. For instance, the adsorption of Sn on CeO<sub>2</sub> films results in the formation of Sn<sup>2+</sup> cations accompanied by the reduction of Ce<sup>4+</sup> cations and formation of Ce<sup>3+</sup> centers.<sup>130–132</sup> Thus, the adsorption of Sn on Pt–CeO<sub>2</sub> could trigger the conversion of Pt<sup>2+</sup> to sub-nanometer Pt particles. The process could occur at low temperature and without the formation of oxygen vacancies.

Indeed, stepwise Sn deposition onto the Pt–CeO<sub>2</sub> film at 300 K in UHV initiated the reduction of Pt<sup>2+</sup> species yielding sub-nanometer Pt particles (see Fig. 25). Comparing the trends in the formation of Pt particles under different Sn deposition conditions, it was possible to correlate the onset of Pt<sup>2+</sup> reduction with the concentration of the Ce<sup>3+</sup> centers determined by the RER.<sup>127</sup> Estimating the number of Ce<sup>3+</sup> centers formed by Sn deposition on the Pt–CeO<sub>2</sub> film it was concluded that approximately 6 Ce<sup>3+</sup> cations are required per Pt<sup>2+</sup> species to induce the reduction of Pt<sup>2+</sup>. This number corresponds to 3 Sn<sup>2+</sup> cations deposited per Pt<sup>2+</sup> species. This finding is in good agreement with density functional modeling data.<sup>127</sup>

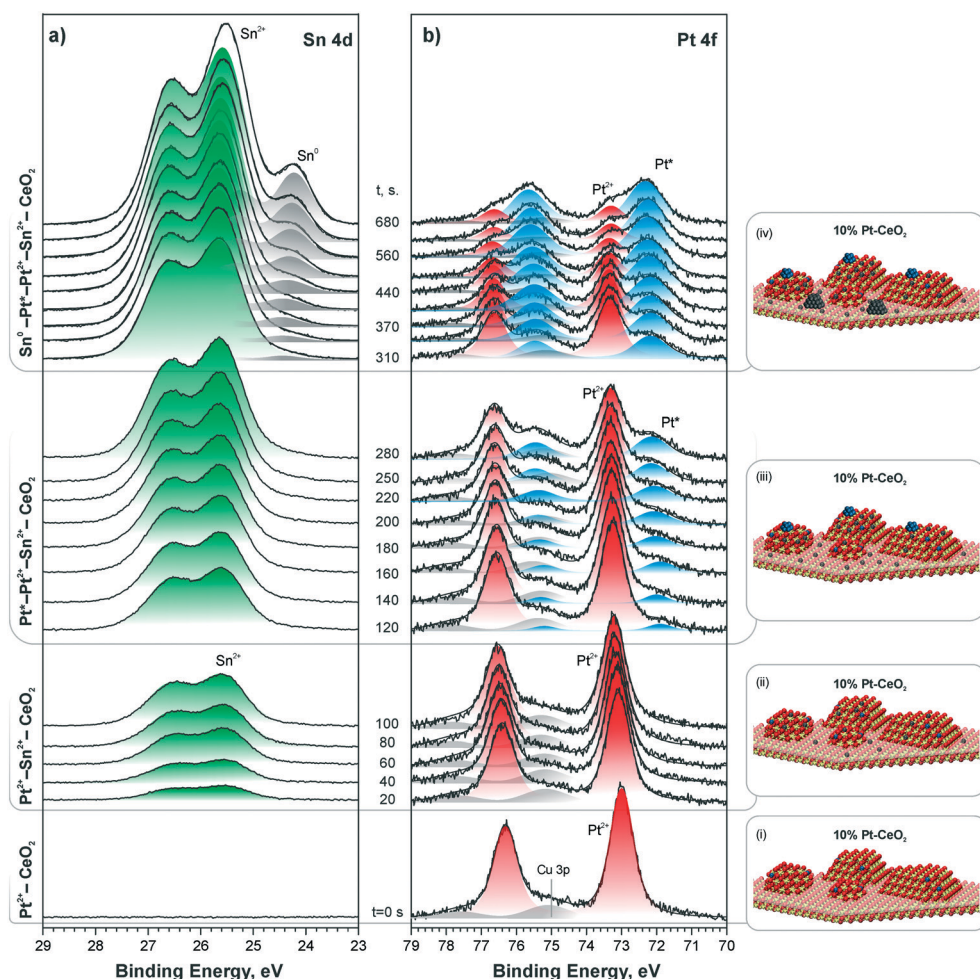


**Fig. 25** Sn 4d (a) and Pt 4f (b) spectra obtained from a 10% Pt–CeO<sub>2</sub> film during stepwise Sn deposition at 300 K in UHV. The Sn 4d and Pt 4f spectra were obtained with photon energies of 60 and 180 eV, respectively. The spectra are grouped (i)–(iv) according to the Pt and Sn oxidation states in the film. In the corresponding ball-and-stick models (i)–(iv), red, yellow, blue, and dark grey balls represent oxygen, cerium, platinum, and tin, respectively. Reproduced from ref. 127 with permission from the Royal Society of Chemistry.



## 6. Properties of supported sub-nanometer metal particles

### 6.1. Metal-support interaction as a function of particle size

Metal particles supported on reducible ceria-based materials retain a number of unique properties arising from electronic metal-support interactions (EMSI).<sup>34,102,119,133</sup> These include, for instance, higher reactivity and selectivity, structural flexibility, and self-cleaning capacity. Depending on the strength of the EMSI, there is a substantial charge transfer between the supported metal particle and the supporting oxide.<sup>73,117,119,134,135</sup> Combining synchrotron-radiation photoelectron spectroscopy and scanning tunneling microscopy it was possible to “count” the number of electrons transferred across the metal/oxide interface as a function of particle size (Fig. 26).<sup>117</sup> The maximum charge transferred per Pt atom was detected at particle sizes between 1 and 1.5 nm corresponding to a number of 30 and 70 Pt atoms per particle (see Fig. 26a). At higher Pt coverage the overall number of transferred electrons approaches a limit (Fig. 26b). Consequently, the average charge per Pt atom decreases as a function of size for particles containing more than 70 Pt atoms (Fig. 26a). At these particle sizes, the metal–support interaction is mostly

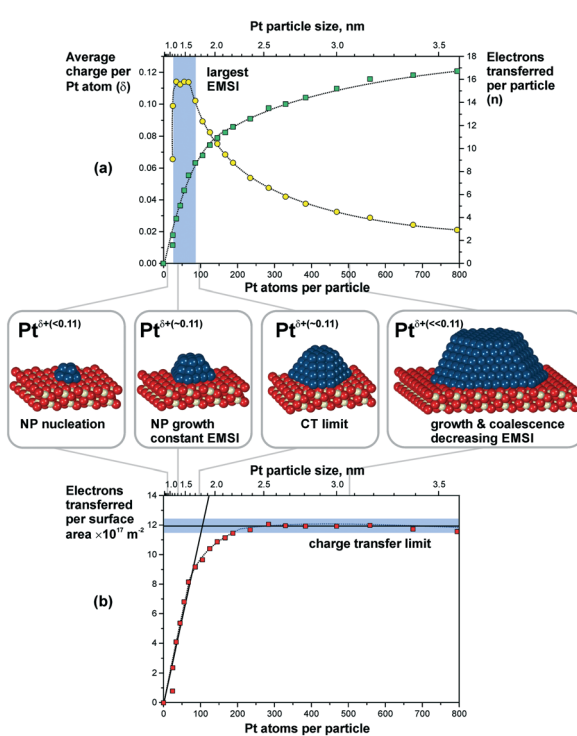


**Fig. 26** (a) The number of electrons transferred per Pt particle to the ceria support increases with increasing particle size (green squares). The partial charge per Pt atom reaches a maximum for particles with 30 to 70 atoms (yellow circles). Here, the EMSI is largest. (b) At higher Pt coverage the total amount of transferred charge approaches a limit which we denote as the “charge transfer limit” (red squares). The atomic models show schematically the average particle sizes in the different regions. Reproduced with permission from ref. 117, Copyright 2016, Nature Publishing Group.

associated with the restructuring of the particle shape and Pt/cevia interface which is rather insensitive to the charge transfer.<sup>136</sup> Density functional modeling rationalized the magnitude of the charge transfer, mainly depending on three parameters, *i.e.* the size of the Pt particles, their density, and the presence of oxygen vacancies<sup>117</sup> (Fig. 27). In particular, the limits of charge transfer were attributed to the electrostatic destabilization at a high surface concentration of Ce<sup>3+</sup> centers. In this respect, the degree of nanostructuring, *i.e.* the size of ceria nanoparticles or the roughness of the ceria support, becomes an additional parameter that has a direct impact on the magnitude of the charge transfer.<sup>134</sup> The charge transfer would thus increase with increasing density of low-coordinated Ce<sup>4+</sup> cations which are capable of accepting electrons from Pt particles and still avoid electrostatic destabilization.<sup>134</sup>

The most remarkable behavior was observed in the regime of sub-nanometer sized Pt particles (Fig. 26a). There, the charge transfer per Pt atom was found to decrease compared to what was predicted by DFT calculations for Pt particles on surfaces of stoichiometric ceria.<sup>117,119,137</sup> The observed phenomenon was assigned to nucleation of Pt at Ce<sup>3+</sup> defect sites.<sup>117,138</sup> Indeed, calculated models also showed that vacancies reduce the net charge transfer from Pt to ceria (Fig. 27). In consequence, the net charge transfer is a function of the degree of reduction of the ceria support.<sup>35,139,140</sup> Depending on the specific system, metal particles can bear a positive charge on highly oxidized ceria supported and a negative charge on highly reduced supports.<sup>139,140</sup>

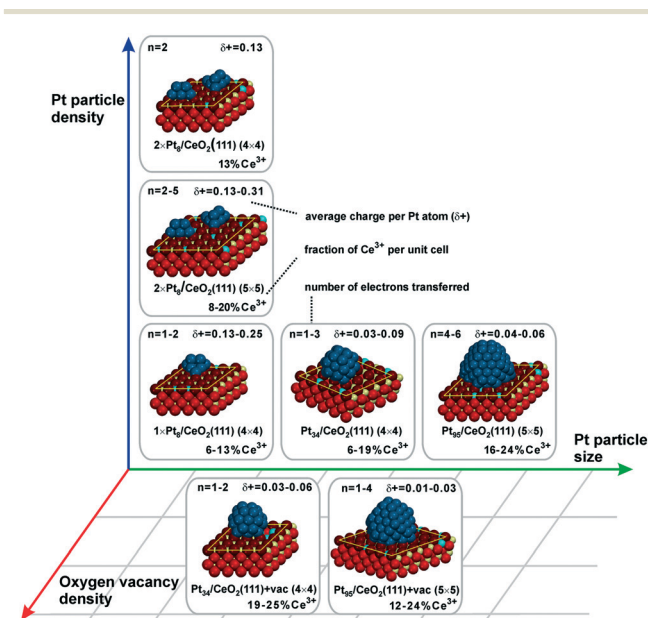


**Fig. 27** Summarized results of density functional calculations of Pt<sub>n</sub>/CeO<sub>2</sub>(111) models. The particle size, the particle density, and the oxygen vacancy density on the support are important factors that control the charge transfer across the metal–oxide interface. Reproduced with permission from ref. 117, Copyright 2016, Nature Publishing Group.



In summary, the charge transfer is controlled by the particle size, the particle density, the support structure and the degree of reduction of the ceria support.

The DFT modeling suggests that the charge is mainly localized on metal atoms in the vicinity of the interface.<sup>117,136</sup> Small Pt aggregates in the sub-nanometer regime consist of only a few atomic layers and, therefore, most of their surface atoms bear an excess charge. This effect may be employed to modify the catalytic properties of the supported particles.

## 6.2. Charge transfer in aqueous environments

On ceria-based catalysts, water molecules readily dissociate *via* proton transfer to surface O atoms, resulting in partial surface hydroxylation.<sup>101,141,142</sup> DFT calculations were employed to investigate water dissociation at the ceria (111) surface<sup>143</sup> and at the ceria/liquid interface<sup>144</sup> as well as to elucidate the charge transfers between Pt particles and the ceria support resulting from water dissociation. The influence of the aqueous environment on the reaction mechanism, thermodynamics and kinetics was investigated by means of *ab initio* molecular dynamics (MD) simulations.<sup>144</sup>

At equilibrium, these MD simulations revealed the existence of a fast proton dynamics at the water/ceria interface involving surface hydroxyl groups, solvated hydroxide ions, and water molecules coordinated to the surface Ce<sup>4+</sup> cations at the water/ceria interface.<sup>144</sup> Under these conditions, the dissociation of water molecules in the first surface solvation layer becomes a reversible dynamic process, which is governed by solvent-induced short-ranged transfers of protons between the adsorbed water molecules and the surface oxygen sites, or, in the reverse process, between surface hydroxyl groups and solvated hydroxide ions. The local increase of concentration of hydroxide ions on ceria surface, which results from water dissociation, activates a water-mediated Grotthus-like mechanism that gives rise to fast long-ranged proton diffusion along the water/ceria interface.<sup>144</sup> It involves concerted transfer of protons along the chains formed by solvent water molecules bridging between surface hydroxide and surface water molecules (Fig. 28a and b).

The catalytic importance of this dynamic process was demonstrated for water dissociation in the presence of supported sub-nanometer-sized Pt nanoparticles where the solvent accelerates the spillover of ad-species between oxide and metal sites.<sup>144</sup> The mechanism of this process, calculated in the presence of a Pt<sub>6</sub> cluster on a stoichiometric ceria (111) slab, is demonstrated in Fig. 28c–e. In the first step, a water molecule of the solvation layer dissociates at the periphery of the supported Pt particle into a hydroxide ion and a proton. This activates the dissociation of a neighboring solvent water molecule (see ovals in Fig. 28c and d), which mediates the proton transfer at the water/oxide interface. The proton is effectively transferred to an oxide surface site away from the nanoparticle, forming a surface hydroxyl (Fig. 28e). The resulting OH<sup>-</sup> species readily binds to a Pt site of the

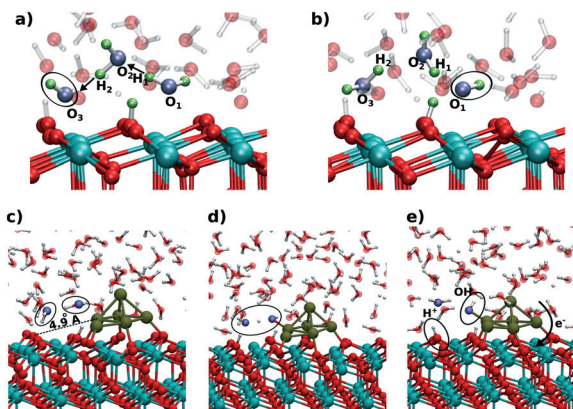


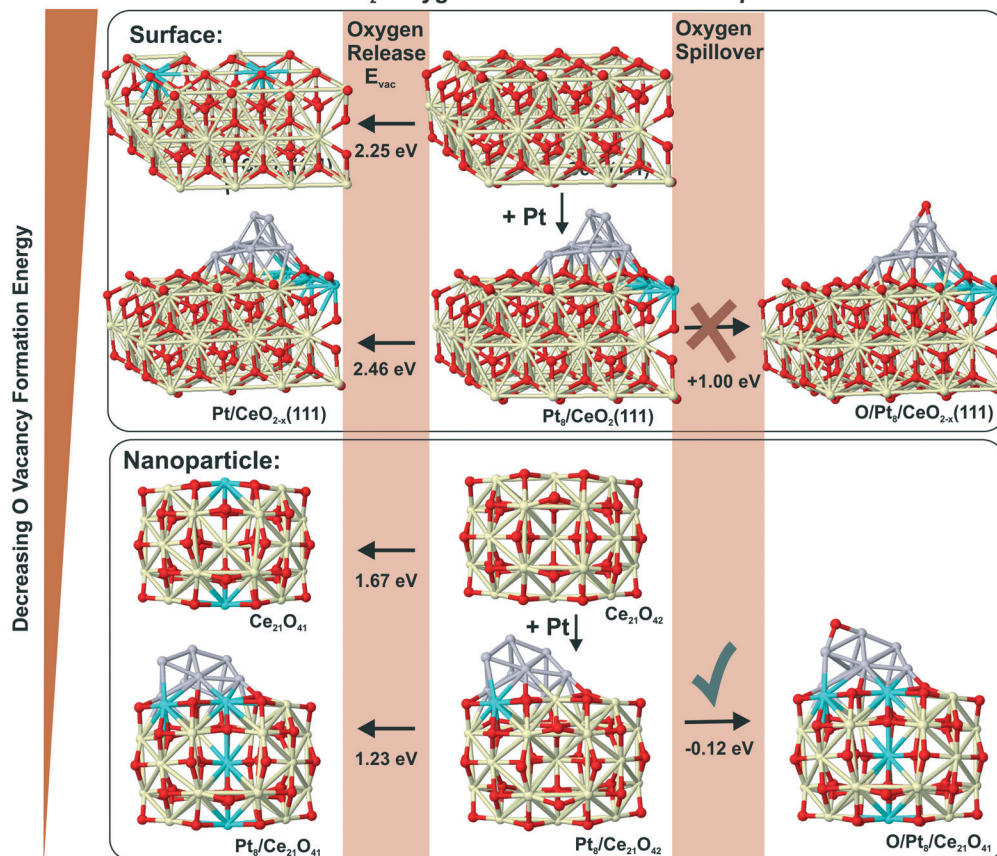
Fig. 28 Snapshots from the *ab initio* MD simulations showing the initial (a and c), intermediate (d), and final (b and e) configurations of the proton chain leading to long-range proton diffusion on the CeO<sub>2</sub>(111) surface (a and b) and at the periphery of a supported Pt<sub>6</sub> cluster (c–e). Adapted with permission from ref. 144, Copyright 2016, American Chemical Society.

supported cluster inducing substantial charge transfer across the metal/oxide interface.

Upon electron reorganization in the Pt/CeO<sub>2</sub> system one electron from the hydroxide species and another one from the Pt cluster are transferred to the oxide substrate through the metal/oxide interface, thus indicating that the cluster/solvent and metal/oxide interfaces are strongly coupled.<sup>144</sup> This demonstrates that, with respect to UHV conditions, the number of electrons transferred from a supported Pt cluster in an aqueous environment to the ceria support is larger by up to a factor of two.<sup>144</sup> Given the concerted reaction mechanism, the transfer of protons away from the Pt cluster cannot be distinguished from the transfer of the hydroxide ion towards the Pt cluster. In any case, however, the supported Pt clusters act as a basin attracting hydroxide species, which consequently accumulate at the cluster sites.

## 6.3. Formation of oxygen vacancies and reverse oxygen spillover

In the context of metal-support interaction, the supported metal particles may have a significant influence on the reactivity of ceria and, particularly, on its oxygen storage capacity. For bare ceria, the formation of oxygen vacancies in ceria nanostructures is strongly favored with respect to bulk samples.<sup>65,68,83,145,146</sup> DFT calculations suggest that the oxygen vacancy formation energy decreases from 2.25 eV on the CeO<sub>2</sub>(111) slab to 0.8 eV on ceria nanoparticles such as Ce<sub>40</sub>O<sub>80</sub> (see Fig. 29). The deposition of a Pt particle appears to have only little effect on the energy of vacancy formation, both on extended ceria<sup>73,119</sup> and on ceria nanoparticles<sup>134</sup> (Fig. 29). However, the formation of an oxygen vacancy results in a variation of the initial charge of the supported Pt<sub>8</sub> particle as a function of the size of the ceria nanoparticle, *i.e.* the degree of ceria nanostructuring.<sup>119,134</sup> This effect reflects the flexibility of the electronic structure of nanostructured ceria-based systems.

Metal Oxide Interaction on Pt/CeO<sub>2</sub>: Oxygen Release and Reverse Spillover

**Fig. 29** Oxygen release and oxygen reverse spillover in extended and nanostructured Pt/ceria models according to DFT calculations. Reproduced with permission from ref. 119, Copyright 2011, Nature Publishing Group.

In the presence of supported Pt particles, oxygen vacancies can also be created by migration of atomic oxygen from the support onto Pt particles. The corresponding process is denoted as reverse oxygen spillover. Considering the energy of oxygen vacancy formation on CeO<sub>2</sub>(111) (2.25 eV) and the adsorption energy of oxygen on Pt(111) (0.60–1.55 eV),<sup>147</sup> such a reverse spillover process seems to be energetically unfavorable. At this point, the degree of the nanostructuring of ceria plays a critical role. In particular, the low energy for oxygen vacancy formation on nanostructured ceria favors reverse oxygen spillover and makes the process exothermic by 0.51 eV (Fig. 29). The reaction is accompanied by the formation of two new Ce<sup>3+</sup> centers. These estimations strongly suggest that the occurrence of oxygen reverse spillover intrinsically requires the presence of a nanostructured ceria support.

The above described processes associated with charge transfer and reverse oxygen spillover were investigated experimentally (see Fig. 30). In particular, the initial increase in Ce<sup>3+</sup> concentration indicates the charge transfer from the Pt particles to the ceria film. In contrast to the charge transfer, reverse oxygen spillover is associated with a substantial activation barrier and does not occur spontaneously at low temperature. However, a rapid increase of the Ce<sup>3+</sup> concentration was observed upon annealing above 500 K which is associated with the onset of reverse oxygen spillover (Fig. 30).

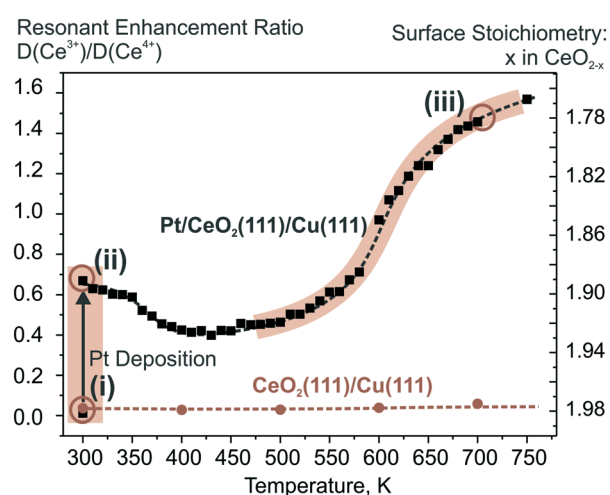


**Fig. 30** The evolution of the resonant enhancement ratio (RER) indicates the occurrence of the charge transfer upon Pt deposition on nanostructured CeO<sub>2</sub>(111) at 300 K and the reverse oxygen spillover above 500 K. The RER determined from the heights of the resonant features in the valence bands associated with Ce<sup>3+</sup> and Ce<sup>4+</sup> cations scales with the Ce<sup>3+</sup>/Ce<sup>4+</sup> concentration ratio by a factor of 5.5.<sup>117</sup> Reproduced with permission from ref. 119, Copyright 2011, Nature Publishing Group.

#### 6.4. Structural flexibility of sub-nanometer metal particles

The structural flexibility of metal particles facilitates a chemical reaction by reducing the activation barrier.<sup>137,148–153</sup> In the regime of sub-nanometer size this property should become increasingly important. For instance, for a Pt<sub>6</sub> cluster supported on a regular CeO<sub>2</sub>(111) surface the structural flexibility of the former turns the energetic balance of oxygen reverse spillover from endothermic, when structural changes are neglected, to weakly exothermic, when structural changes are taken into account (see Fig. 31).<sup>137</sup> In other words, the binding energy of an oxygen atom to the Pt<sub>6</sub> cluster becomes comparable to the binding energy of oxygen in the ceria lattice if structural rearrangements in the Pt cluster are considered. Interestingly, this effect suggests that oxygen transfer to supported Pt clusters does not necessarily require nanostructured ceria particles, but may become slightly exothermic for very small Pt clusters even on extended ceria surfaces.<sup>137,145</sup> Notably, the initial and final stages of this process identified with global structural optimization indicate a transition from a 3D to 2D morphology of the supported Pt<sub>6</sub> cluster (Fig. 31).

#### 6.5. Interconversion between atomically dispersed Pt<sup>2+</sup> and sub-nanometer sized Pt particles

Because of the strong correlation between the oxidation state of Pt and the degree of reduction of the ceria support, it is expected that the Pt–CeO<sub>2</sub> catalyst can switch between two stable states, one associated with atomically dispersed Pt<sup>2+</sup> species anchored at {100} sites and a second one with the Pt

from sub-nanometer-sized Pt aggregates. The interconversion between the two states will occur in response to changes of the reactive environment. The latter may be associated with changes in the gas composition or, in the case of the fuel cell catalysts, in response to changes of the electrode potential.

Reversible changes in the oxidation state of Pt particles supported on nanostructured ceria have previously been monitored by Hatanaka *et al.*<sup>154</sup> The presence of oxidized Pt species was explained by the formation of Pt–O–Ce bonds in an oxidative atmosphere at high temperature. It was proposed that the formation of such bonds drives the re-dispersion of Pt particles into smaller clusters.<sup>155</sup> These studies<sup>154,155</sup> suggested the formation of a monolayer of oxidized Pt on the surface of a ceria-based material after treatment in an oxygen atmosphere. Based on the binding energy of the corresponding species in Pt 4f spectra, we speculate that the species described in that work are similar to Pt<sup>2+</sup> species anchored at {100} facets described above.

On single-crystal-based Pt–CeO<sub>2</sub> model films containing traces of metallic Pt, annealing in a H<sub>2</sub> atmosphere was shown to trigger reduction of Pt<sup>2+</sup> and formation of metallic Pt, both in the form of sub-nanometer sized aggregates and larger Pt particles.<sup>98,99</sup> The corresponding situation is shown in Fig. 32a.

Remarkably, the subsequent annealing of the Pt–CeO<sub>2</sub> film in oxygen triggers partial re-dispersion of metallic Pt particles. We observe a partial recovery of the characteristic signal associated with the Pt<sup>2+</sup> species anchored at the {100} sites (Fig. 32a). Similar and partially reversible changes were also observed between Pd<sup>2+</sup> species and metallic Pd particles (Fig. 32b). The degree of reversibility between two oxidation states likely depends on the conditions of the redox treatment, *e.g.* the temperature and the pressure of hydrogen and oxygen. Additionally, the degree of sintering can be controlled by the metal loading in a ceria-based catalyst.<sup>156</sup> In this respect the ideal Pt loading should allow full recovery of the atomically dispersed state.<sup>104</sup> It is likely that the degree of stabilization and the strong dependence of the catalytic activity (power density) on Pt loading observed for the Pt–CeO<sub>2</sub>

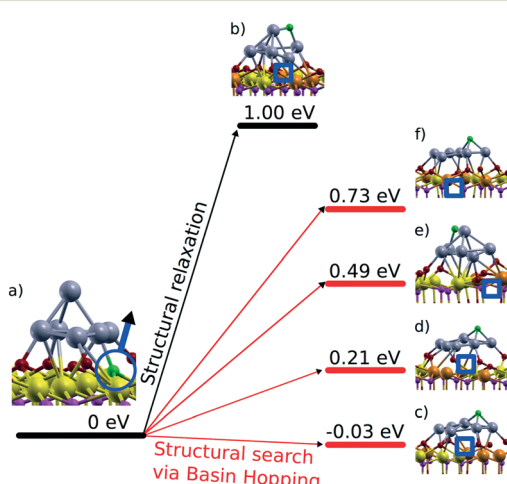


**Fig. 31** Thermodynamics of reverse oxygen spillover between a supported Pt<sub>6</sub> cluster and a CeO<sub>2</sub>(111) surface. Initial state (a) Pt<sub>6</sub> cluster deposited on a stoichiometric CeO<sub>2</sub>(111) slab and final states (b–f), partially oxidized Pt<sub>6</sub>O cluster on the slab with an oxygen vacancy beneath the cluster, resulting from a usual structural relaxation towards the local minimum (b) and from a basin hopping structure optimization (c–f) that allows the global minimum to be reached in the configurational space. Pt atoms are in gray, oxygen from the first (second) layer in red (violet), Ce<sup>4+</sup> in yellow, and Ce<sup>3+</sup> in orange. The oxygen vacancy site is indicated by blue squares. Reproduced with permission from ref. 137, Copyright 2014, American Chemical Society.

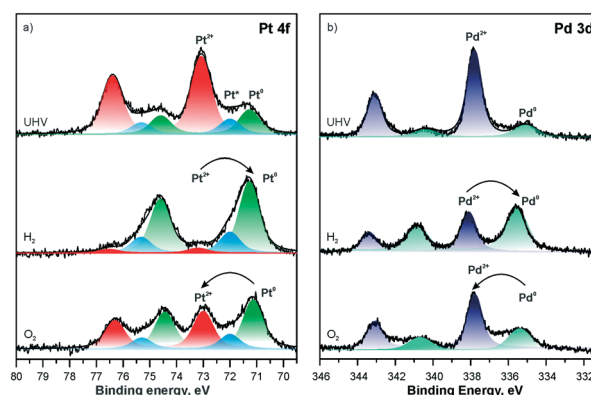


**Fig. 32** The development of Pt 4f (a) and Pd 3d (b) spectra obtained from Pt–CeO<sub>2</sub> and Pd–CeO<sub>2</sub> films, respectively, following the annealing in UHV (top), under H<sub>2</sub> (middle), and O<sub>2</sub> (bottom) atmosphere.



anode fuel cell catalysts are associated with the degree of reversibility that can be achieved in the catalyst film.<sup>41</sup>

## 7. Active state of Pt–CeO<sub>x</sub> thin film catalysts under electrochemical conditions

The active state of the Pt–CeO<sub>x</sub> catalyst films under electrochemical conditions can be examined by means of spectroelectrochemical methods. In line with the above discussion, changes of the electrode potential give rise to dynamic changes in the oxidation state of ceria and, in response, also of the supported Pt species. The stability of Pt–CeO<sub>x</sub> catalyst films was investigated as a function of Pt loading by means of electrochemical infrared spectroscopy.<sup>109</sup> In these experiments CO formed during electro-oxidation of methanol was employed as a probe molecule. The corresponding IR spectra obtained from Pt–CeO<sub>x</sub> films are presented in Fig. 33. Reference spectra obtained from Pt(111) under identical conditions are also shown for comparison.

Typically, CO adsorption on Pt(111) gives rise to two bands associated with adsorption in on-top (CO<sub>t</sub>) and bridging (CO<sub>b</sub>) configurations (see Fig. 33a). Clearly, the emergence of CO<sub>t</sub> stretching bands on Pt–CeO<sub>x</sub> films indicates that a fraction of the atomically dispersed Pt<sup>2+</sup> species was converted into metallic Pt particles already in the first potential cycle.

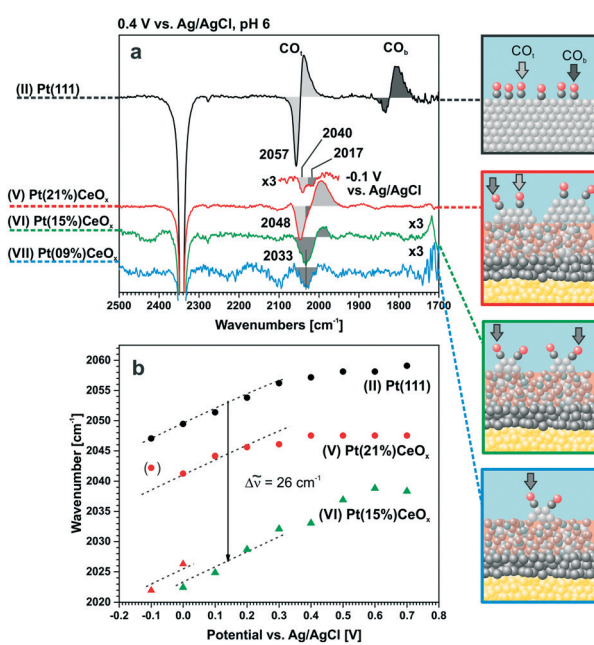


**Fig. 33** Comparison of the electrochemical IR spectra taken during methanol oxidation on Pt–CeO<sub>x</sub> electrocatalysts with different Pt concentrations at pH 6 (1 M CH<sub>3</sub>OH in 0.1 M HClO<sub>4</sub>): (a) IR spectra at an electrode potential of 0.4 V<sub>Ag/AgCl</sub> (reference –0.15 V<sub>Ag/AgCl</sub>); (b) peak position of the on-top CO band as a function of the electrode potential. The samples are numbered (I–VII) for easy comparison. Reproduced with permission from ref. 109, Copyright 2016, American Chemical Society.

The red shift and broadening of the CO<sub>t</sub> band along with the absence of the CO<sub>b</sub> on Pt–CeO<sub>x</sub> films suggests the formation of small Pt aggregates with less developed (111) facets.<sup>157</sup> In particular, the contributions from the low-coordinated sites and from (111) facet are well resolved on Pt–CeO<sub>x</sub> films with high Pt loading (see dark and light grey areas and arrows in Fig. 33a). In the limit of low Pt loadings, the CO<sub>t</sub> band is dominated by the contributions from CO adsorbed at low-coordinated sites. This situation is consistent with the formation of sub-nanometer-sized Pt particles that do not expose any measurable fraction of regular (111) facets.

Under electrochemical conditions, the blue shift of the CO<sub>t</sub> bands with increasing electrode potential is associated with the Stark effect.<sup>158</sup> The relative offsets in the Stark plot between the Pt(111) and Pt–CeO<sub>x</sub> films (Fig. 33b) are related to the size of supported Pt particles. Density functional modeling reinforces the correlation between the stretching frequency and the particle size, on both unsupported and supported Pt particles.<sup>109,110</sup> In particular, the offset of the CO vibrational frequencies by 26 cm<sup>-1</sup> with respect to Pt(111) indicates the formation of sub-nanometer-sized particles containing about 30 Pt atoms per particle.

The findings both in UHV and under electrochemical conditions suggest that the conversion of atomically dispersed Pt<sup>2+</sup> to sub-nanometer sized Pt particles transforms the Pt–CeO<sub>x</sub> film into an electrocatalytically active state. Notably, the stability of the sub-nanometer Pt particles under electrochemical conditions is a function of the Pt loading. A progressive blue shift of the CO<sub>t</sub> band on the Pt–CeO<sub>x</sub> film with high Pt loading during repetitive cycling is associated with sintering and growth of larger Pt particles with defined (111) facets (Fig. 34a). In sharp contrast, such changes are not seen for Pt–CeO<sub>x</sub> films with low Pt loading, even after repeated

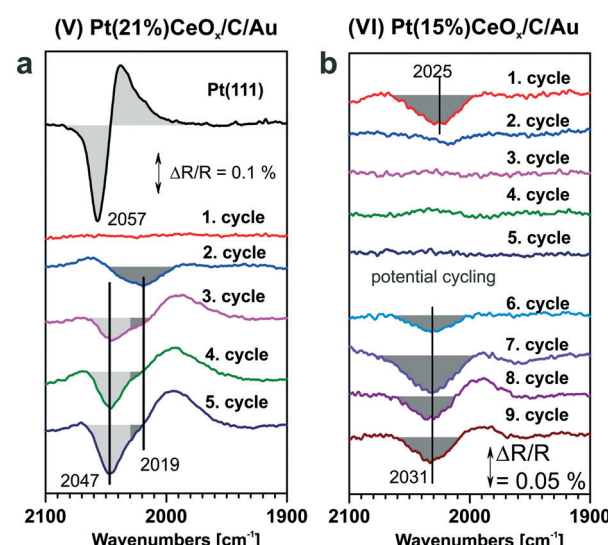


**Fig. 34** Electrochemical IR spectra during repeated cycles of methanol oxidation on (a) Pt(21%)-CeO<sub>x</sub>/C/Au and (b) Pt(15%)-CeO<sub>x</sub>/C/Au at 0.4 V<sub>Ag/AgCl</sub>. All reference spectra were taken at a potential of –0.15 V<sub>Ag/AgCl</sub>. Adapted with permission from ref. 109, Copyright 2016, American Chemical Society.



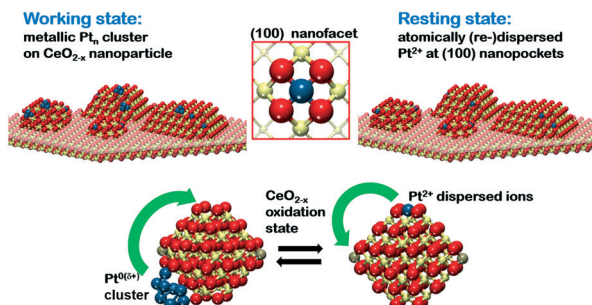


**Fig. 35** The Pt–CeO<sub>x</sub> catalyst in two stable states associated with atomically dispersed Pt<sup>2+</sup> species (resting state) and sub-nanometer Pt particles (working state) in an electrochemical environment. The conversion between two states is driven by the charge transfer as a function of the electrode potential. DFT modeling corroborates reversible conversion as a function of the degree of reduction of ceria in the presence of {100} sites.

potential cycling (Fig. 34b). This behavior is consistent with enhanced stability of the sub-nanometer Pt particles on Pt–CeO<sub>x</sub> films with low Pt loading in an electrochemical environment.

The enhanced stability of the sub-nanometer Pt particles is associated with the strong interaction between Pt particles and ceria support. The above findings suggest that Pt<sup>2+</sup> species are formed under oxidizing conditions, which prevents the Pt particles from sintering during potential cycling. In this respect, the abundance of the {100} sites determines the maximum Pt loading in Pt–CeO<sub>x</sub> films up to which the stabilization mechanism will operate. At Pt loadings exceeding the density of these sites, the formation and growth of larger metallic Pt particles is no longer suppressed.

In summary, the Pt–CeO<sub>x</sub> catalyst with ideal Pt loading will be able to undergo reversible conversion between atomically dispersed Pt<sup>2+</sup> species and sub-nanometer Pt particles as a function of the oxidation state and/or the electrode potential.

A consistent scenario would involve the presence of two stable states, denoted as the working state and the resting state (see Fig. 35). Accordingly, the resting state is associated with the formation of atomically dispersed Pt<sup>2+</sup> anchored at {100} nanofacets. The conversion from the resting state into the working state is accompanied by the formation of sub-nanometer Pt particles triggered by the reduction under electrochemical conditions. Conversely, the resting state is recovered upon returning to oxidizing conditions. Note that such dynamic changes of the Pt oxidation state are typically associated with dissolution processes and sintering. In the presence of the ceria support, the release of Pt species may be prevented, leading to enhanced stability and constant activity.

## Conclusions

A dynamic catalyst concept involving a single atom catalyst state has been applied to prepare anode fuel cell catalysts with high noble metal efficiency and enhanced stability. The approach involves the deposition of thin Pt–CeO<sub>2</sub> films on

carbon substrates by means of radio frequency magnetron sputtering from separate CeO<sub>2</sub> and Pt targets in a non-reactive atmosphere. The deposition process is accompanied by the etching of carbon substrates yielding highly porous columnar structures coated with Pt–CeO<sub>2</sub> films. Atomically dispersed Pt was found to be present in these films in the form of Pt<sup>2+</sup> and Pt<sup>4+</sup> species at the surface and in the bulk, respectively. The ratio between the Pt<sup>2+</sup> and Pt<sup>4+</sup> species strongly depends on the degree of the nanostructuring of the Pt–CeO<sub>2</sub> films. Fuel cell tests demonstrated the direct link between the electrocatalytic performance of the Pt–CeO<sub>2</sub> films and the density of the surface Pt<sup>2+</sup> species.

The local structure and reactivity of the Pt<sup>2+</sup> species supported on nanostructured ceria films have been investigated by a variety of techniques including high-resolution TEM, SRPES, AR XPS, HAXPS, and STM in combination with density functional modeling. The appropriate model systems were developed to identify possible anchoring sites for the atomically dispersed Pt species. By means of density functional calculations and surface-science-based model catalysts the adsorption sites yielding strongly anchored Pt<sup>2+</sup> were associated with {100} nanofacets on ceria particles. There, the Pt<sup>2+</sup> species were found to be located in the center of a planar PtO<sub>4</sub> moiety forming a quadratic coordination environment. A similar structural element was found at the steps of CeO<sub>2</sub>(111) films. CeO<sub>2</sub>(100) nanofacets were also identified on real Pt–CeO<sub>2</sub> catalyst films by means of HRTEM.

The stability and the reactivity of the Pt<sup>2+</sup> species were investigated as a function of Pt loading on the model Pt–CeO<sub>2</sub> films under ultra-high vacuum conditions. It was found that the capacity of the nanostructured ceria surface to form isolated Pt<sup>2+</sup> is limited by the number of available {100} sites. If the Pt loading exceeds the density of anchoring sites available, the growth of Pt nanoparticles is observed.

The activation of molecular hydrogen at single Pt<sup>2+</sup> species is associated with a high activation barrier. In the presence of metallic Pt, the hydrogen activation is facile and eventually leads to reduction of all Pt<sup>2+</sup> species. It was found that metallic Pt is not directly involved in the reduction of the Pt<sup>2+</sup> species. Instead the reduction of Pt<sup>2+</sup> is coupled to the reduction of Ce<sup>4+</sup> to Ce<sup>3+</sup>, resulting from the formation of oxygen vacancies. Reaction with methanol also leads to reduction of the ceria support and triggers the formation of sub-nanometer Pt particles. Alternatively, the reduction of Pt<sup>2+</sup> and the formation of Pt particles can also be mediated by co-adsorption of reducing agents such as Sn that lead to formation of Ce<sup>3+</sup> without formation of oxygen vacancies. In an electrochemical environment, conversion of the Pt<sup>2+</sup> species to sub-nanometer Pt particles is triggered by the electrode potential.

The sub-nanometer Pt particles exhibit remarkable thermal stability with respect to sintering under both UHV and electrochemical conditions. The chemical properties of the supported sub-nanometer-sized particles are modified by metal–support interactions associated with strong charge transfer, by their structural flexibility, and by spillover phenomena. Regarding

the electronic metal support interactions between Pt particles and ceria, the amount of charge accumulated on the Pt particle depends on the Pt particle, the particle density, the structure and the stoichiometry of the ceria support.

From the above results, a consistent picture emerges with respect to the operation of the Pt–CeO<sub>2</sub> catalyst films under electrochemical conditions. The stabilization mechanism involves reversible conversion between two chemical states, the atomically dispersed Pt<sup>2+</sup> species and sub-nanometer-sized Pt particles in an electrochemical environment. This concept rationalizes the high stability of the Pt–CeO<sub>2</sub> catalyst films with low Pt loading under conditions of dynamically changing electrode potentials.

Regarding the transfer of the above described concepts to other less expensive metals, similar anchoring phenomena were predicted by density functional modeling for various metals from groups 8 to 11. The general trends in the energetics of the corresponding atomically dispersed metals have been established and could for some metals (Pd, Ni) be confirmed by experiments. However, characteristic differences are observed regarding the stability and segregation behavior, rendering the Pt–CeO<sub>2</sub> system unique in this comparison.

## Outlook

At present, one challenge regarding the application of single-atom-based Pt–CeO<sub>2</sub> films in fuel cell catalysis is the limited density of the {100} sites, which also limits the total Pt loading and the resulting power density. Different strategies may be employed to tackle this challenge. The first strategy focuses on the improvement of the carbon supports. Along this line, GDLs coated with soot or nitrogen doped carbon films demonstrated great potential.<sup>45,54</sup> The second strategy involves shaping the morphology of the Pt–CeO<sub>2</sub> film into high-surface area nanostructures with a large fraction of {100} facets, *e.g.* cubes or nanoscrews.<sup>159,160</sup> This can be achieved, for instance, by innovative deposition techniques or a strain driven growth induced, for example, by doping. As a last strategy, we may consider to prepare the key structure, *i.e.* the square planar PtO<sub>4</sub> moiety, on a different support with a higher degree of nanostructuring.

Additional insight from theoretical modelling studies should also contribute to unravelling in greater detail the mechanism of reversible conversion between Pt<sup>2+</sup> and the sub-nanometer Pt particles and their interaction with reactants. This will allow establishing a kinetic model of the catalyst under fuel-cell operating conditions, providing valuable understanding of the factors influencing the performance of catalytic materials with atomically dispersed metals.

## List of abbreviations

AR XPS	Angle-resolved X-ray photoelectron spectroscopy
nanoGDL, n-GDL	Carbon nanoparticle coated gas diffusion layer

CVD-CNTs	Chemical vapor deposited carbon nanotubes
DFT	Density functional theory
DWCNTs	Double-wall carbon nanotubes
EMSI	Electronic metal-support interactions
GDL	Gas diffusion layer
GLAD	Glancing angle deposition
HAXPS	Hard X-ray photoelectron spectroscopy
SRPES	High-resolution synchrotron spectroscopy
HRTEM	High-resolution transmission electron microscopy
IRAS	Infrared absorption spectroscopy
MWCNTs	Multi-wall carbon nanotubes
ND	Normal deposition
PD	Power density
PEMFC	Proton exchange membrane fuel cell
RER	Resonant enhancement ratio
RPES	Resonant photoemission spectroscopy
SEM	Scanning electron microscopy
SAC	Single atom catalyst
SP	Specific power
UHV	Ultrahigh vacuum
XPS	X-ray photoelectron spectroscopy

## Acknowledgements

This work was funded by the European Community (FP7-NMP.2012.1.1-1 project chipCAT, Reference No. 310191), by the Deutsche Forschungsgemeinschaft (DFG) within the Excellence Cluster “Engineering of Advanced Materials” in the framework of the excellence initiative, by the Spanish MINECO (grants CTQ2012-34969 and CTQ2015-64618-R/FEDER), by the Generalitat de Catalunya (grants 2014SGR97 and XRQTC), and by the Czech Ministry of Education (grant LM2015057). Computer resources, technical expertise and assistance were provided by the Red Española de Supercomputación. Y. L. and coworkers thank Elettra for excellent working conditions and support. The authors also acknowledge the CERIC-ERIC Consortium for the access to experimental facilities and financial support and the COST Action CM1104 for travel support. Finally, the authors thank all colleagues involved in the chipCAT project for their dedication and invaluable contributions.

## References

- Y. Wang, K. S. Chen, J. Mishler, S. C. Cho and X. C. Adroher, A review of polymer electrolyte membrane fuel cells: Technology, applications, and needs on fundamental research, *Appl. Energy*, 2011, **88**, 981–1007.
- S. C. Kelley, G. A. Deluga and W. H. Smyrl, Miniature fuel cells fabricated on silicon substrates, *AIChE J.*, 2002, **48**, 1071–1082.
- J. D. Morse, Micro-fuel cell power sources, *Int. J. Energy Res.*, 2007, **31**, 576–602.



- 4 T. U. D. o. E. (DOE), Energy Efficiency and Renewable Energy, [http://www.eere.energy.gov/hydrogenandfuelcells/mypp/pdfs/fuel\\_cells.pdf](http://www.eere.energy.gov/hydrogenandfuelcells/mypp/pdfs/fuel_cells.pdf).
- 5 C. Wang, M. Yang and M. Flytzani-Stephanopoulos, Single gold atoms stabilized on nanoscale metal oxide supports are catalytic active centers for various reactions, *AICHE J.*, 2016, **62**, 429–439.
- 6 J. Liu, Catalysis by Supported Single Metal Atoms, *ACS Catal.*, 2017, **7**, 34–59.
- 7 S. Liang, C. Hao and Y. Shi, The Power of Single-Atom Catalysis, *ChemCatChem*, 2015, **7**, 2559–2567.
- 8 X.-F. Yang, A. Wang, B. Qiao, J. Li, J. Liu and T. Zhang, Single-Atom Catalysts: A New Frontier in Heterogeneous Catalysis, *Acc. Chem. Res.*, 2013, **46**, 1740–1748.
- 9 M. Flytzani-Stephanopoulos and B. C. Gates, Atomically Dispersed Supported Metal Catalysts, *Annu. Rev. Chem. Biomol. Eng.*, 2012, **3**, 545–574.
- 10 C. K. Narula and M. Moses-DeBusk, in *Catalysis by Materials with Well-Defined Structures*, ed. S. H. Overbury, Elsevier, Amsterdam, 2015, pp. 263–274.
- 11 N. Cheng, S. Stambula, D. Wang, M. N. Banis, J. Liu, A. Riese, B. Xiao, R. Li, T.-K. Sham, L.-M. Liu, G. A. Botton and X. Sun, Platinum single-atom and cluster catalysis of the hydrogen evolution reaction, *Nat. Commun.*, 2016, **7**, 13638.
- 12 S. Sun, G. Zhang, N. Gauquelain, N. Chen, J. Zhou, S. Yang, W. Chen, X. Meng, D. Geng, M. N. Banis, R. Li, S. Ye, S. Knights, G. A. Botton, T.-K. Sham and X. Sun, Single-atom Catalysis Using Pt/Graphene Achieved through Atomic Layer Deposition, *Sci. Rep.*, 2013, **3**, 1775.
- 13 H. Wang, Q. Feng, Y. Cheng, Y. Yao, Q. Wang, K. Li, U. Schwingenschlögl, X. X. Zhang and W. Yang, Atomic Bonding between Metal and Graphene, *J. Phys. Chem. C*, 2013, **117**, 4632–4638.
- 14 S. Yang, J. Kim, Y. J. Tak, A. Soon and H. Lee, Single-Atom Catalyst of Platinum Supported on Titanium Nitride for Selective Electrochemical Reactions, *Angew. Chem., Int. Ed.*, 2016, **55**, 2058–2062.
- 15 R.-Q. Zhang, T.-H. Lee, B.-D. Yu, C. Stampfl and A. Soon, The role of titanium nitride supports for single-atom platinum-based catalysts in fuel cell technology, *Phys. Chem. Chem. Phys.*, 2012, **14**, 16552–16557.
- 16 K. Mao, L. Li, W. Zhang, Y. Pei, X. C. Zeng, X. Wu and J. Yang, A Theoretical Study of Single-Atom Catalysis of CO Oxidation Using Au Embedded 2D h-BN Monolayer: A CO-Promoted O<sub>2</sub> Activation, *Sci. Rep.*, 2014, **4**, 5441.
- 17 G. Vilé, D. Albani, M. Nachtegaal, Z. Chen, D. Dontsova, M. Antonietti, N. López and J. Pérez-Ramírez, A Stable Single-Site Palladium Catalyst for Hydrogenations, *Angew. Chem., Int. Ed.*, 2015, **54**, 11265–11269.
- 18 J. M. Thomas, Catalysis: Tens of thousands of atoms replaced by one, *Nature*, 2015, **525**, 325–326.
- 19 J. Lu, C. Aydin, N. D. Browning and B. C. Gates, Imaging Isolated Gold Atom Catalytic Sites in Zeolite NaY, *Angew. Chem., Int. Ed.*, 2012, **51**, 5842–5846.
- 20 A. Uzun, V. Ortalan, Y. Hao, N. D. Browning and B. C. Gates, Imaging Gold Atoms in Site-Isolated MgO-Supported Mononuclear Gold Complexes, *J. Phys. Chem. C*, 2009, **113**, 16847–16849.
- 21 A. Bruix, Y. Lykhach, I. Matolínová, A. Neitzel, T. Skála, N. Tsud, M. Vorokhta, V. Stetsovych, K. Ševčíková, J. Mysliveček, R. Fiala, M. Václavů, K. C. Prince, S. Bruyere, V. Potin, F. Illas, V. Matolín, J. Libuda and K. M. Neyman, Maximum Noble Metal Efficiency in Catalytic Materials: Atomically Dispersed Surface Platinum, *Angew. Chem., Int. Ed.*, 2014, **53**, 10525–10530.
- 22 F. Dvořák, M. Farnesi Camellone, A. Tovt, N.-D. Tran, F. R. Negreiros, M. Vorokhta, T. Skála, I. Matolínová, J. Mysliveček, V. Matolín and S. Fabris, Creating single-atom Pt-ceria catalysts by surface step decoration, *Nat. Commun.*, 2016, **7**, 10801.
- 23 B. T. Qiao, A. Q. Wang, X. F. Yang, L. F. Allard, Z. Jiang, Y. T. Cui, J. Y. Liu, J. Li and T. Zhang, Single-atom catalysis of CO oxidation using Pt<sub>1</sub>/FeO<sub>x</sub>, *Nat. Chem.*, 2011, **3**, 634–641.
- 24 R. Si and M. Flytzani-Stephanopoulos, Shape and Crystal-Plane Effects of Nanoscale Ceria on the Activity of Au-CeO<sub>2</sub> Catalysts for the Water-Gas Shift Reaction, *Angew. Chem., Int. Ed.*, 2008, **47**, 2884–2887.
- 25 J. H. Kwak, J. Z. Hu, D. Mei, C. W. Yi, D. H. Kim, C. H. F. Peden, L. F. Allard and J. Szanyi, Coordinatively unsaturated Al<sup>3+</sup> centers as binding sites for active catalyst phases of platinum on gamma-Al<sub>2</sub>O<sub>3</sub>, *Science*, 2009, **325**, 1670–1673.
- 26 P. Hu, Z. Huang, Z. Amghouz, M. Makkee, F. Xu, F. Kapteijn, A. Dikhtierenko, Y. Chen, X. Gu and X. Tang, Electronic Metal-Support Interactions in Single-Atom Catalysts, *Angew. Chem., Int. Ed.*, 2014, **53**, 3418–3421.
- 27 J. Jones, H. Xiong, A. T. DeLaRiva, E. J. Peterson, H. Pham, S. R. Challa, G. Qi, S. Oh, M. H. Wiebenga, X. I. Pereira Hernández, Y. Wang and A. K. Datye, Thermally stable single-atom platinum-on-ceria catalysts via atom trapping, *Science*, 2016, **353**, 150–154.
- 28 L. Wang, W. Zhang, S. Wang, Z. Gao, Z. Luo, X. Wang, R. Zeng, A. Li, H. Li, M. Wang, X. Zheng, J. Zhu, W. Zhang, C. Ma, R. Si and J. Zeng, Atomic-level insights in optimizing reaction paths for hydroformylation reaction over Rh/CoO single-atom catalyst, *Nat. Commun.*, 2016, **7**, 14036.
- 29 T. Rajesh, A. K. Rajarajan, C. S. Gopinath and R. N. Devi, Evidence of Cationic Pt Active for Water-Gas Shift Reaction: Pt-Doped BaCeO<sub>3</sub> Perovskite, *J. Phys. Chem. C*, 2012, **116**, 9526–9532.
- 30 J. Liu, Advanced Electron Microscopy of Metal-Support Interactions in Supported Metal Catalysts, *ChemCatChem*, 2011, **3**, 934–948.
- 31 G. S. Parkinson, Z. Novotny, G. Argentero, M. Schmid, J. Pavělec, R. Kosak, P. Blaha and U. Diebold, Carbon monoxide-induced adatom sintering in a Pd-Fe<sub>3</sub>O<sub>4</sub> model catalyst, *Nat. Mater.*, 2013, **12**, 724–728.
- 32 K. T. Rim, D. Eom, L. Liu, E. Stolyarova, J. M. Raitano, S.-W. Chan, M. Flytzani-Stephanopoulos and G. W. Flynn, Charging and Chemical Reactivity of Gold Nanoparticles and Adatoms on the (111) Surface of Single-Crystal Magnetite: A Scanning Tunneling Microscopy/Spectroscopy Study, *J. Phys. Chem. C*, 2009, **113**, 10198–10205.



- 33 Z. Huang, X. Gu, Q. Cao, P. Hu, J. Hao, J. Li and X. Tang, Catalytically Active Single-Atom Sites Fabricated from Silver Particles, *Angew. Chem., Int. Ed.*, 2012, **51**, 4198–4203.
- 34 C. T. Campbell, Catalyst-support interactions: Electronic perturbations, *Nat. Chem.*, 2012, **4**, 597–598.
- 35 G. Pacchioni, Electronic interactions and charge transfers of metal atoms and clusters on oxide surfaces, *Phys. Chem. Chem. Phys.*, 2013, **15**, 1737–1757.
- 36 M. S. Hegde and P. Bera, Noble Metal Ion Substituted CeO<sub>2</sub> Catalysts: Electronic Interaction between Noble Metal Ions and CeO<sub>2</sub> Lattice, *Catal. Today*, 2015, **253**, 40–50.
- 37 M. S. Hegde, G. Madras and K. C. Patil, Noble Metal Ionic Catalysts, *Acc. Chem. Res.*, 2009, **42**, 704–712.
- 38 E. W. McFarland and H. Metiu, Catalysis by Doped Oxides, *Chem. Rev.*, 2013, **113**, 4391–4427.
- 39 V. Matolín, M. Cabala, I. Matolínová, M. Škoda, M. Václavů, K. C. Prince, T. Skála, T. Mori, H. Yoshikawa, Y. Yamashita, S. Ueda and K. Kobayashi, Pt and Sn Doped Sputtered CeO<sub>2</sub> Electrodes for Fuel Cell Applications, *Fuel Cells*, 2010, **10**, 139–144.
- 40 M. Vaclavu, I. Matolinova, J. Myslivecek, R. Fiala and V. Matolin, Anode Material for Hydrogen Polymer Membrane Fuel Cell: Pt-CeO<sub>2</sub> RF-Sputtered Thin Films, *J. Electrochem. Soc.*, 2009, **156**, B938–B942.
- 41 R. Fiala, A. Figueroba, A. Bruix, M. Vaclavu, A. Rednyk, I. Khalakhan, M. Vorokhta, J. Lavkova, F. Illas, V. Potin, I. Matolinova, K. M. Neyman and V. Matolin, High efficiency of Pt<sup>2+</sup>-CeO<sub>2</sub> novel thin film catalyst as anode for proton exchange membrane fuel cells, *Appl. Catal., B*, 2016, **197**, 262–270.
- 42 V. Matolín, I. Matolínová, M. Václavů, I. Khalakhan, M. Vorokhta, R. Fiala, I. Piš, Z. Sofer, J. Poltierová-Vejpravová, T. Mori, V. Potin, H. Yoshikawa, S. Ueda and K. Kobayashi, Platinum-doped CeO<sub>2</sub> thin film catalysts prepared by magnetron sputtering, *Langmuir*, 2010, **26**, 12824–12831.
- 43 R. Fiala, I. Khalakhan, I. Matolínová, M. Václavů, M. Vorokhta, Z. Sofer, S. Huber, V. Potin and V. Matolín, Pt-CeO<sub>2</sub> Coating of Carbon Nanotubes Grown on Anode Gas Diffusion Layer of the Polymer Electrolyte Membrane Fuel Cell, *J. Nanosci. Nanotechnol.*, 2011, **11**, 5062–5067.
- 44 R. Fiala, M. Vaclavu, A. Rednyk, I. Khalakhan, M. Vorokhta, J. Lavkova, V. Potin, I. Matolinova and V. Matolin, Pt-CeO<sub>x</sub> Thin Film Catalysts for PEMFC, *Catal. Today*, 2015, **240**(Part B), 236–241.
- 45 I. Khalakhan, R. Fiala, J. Lavkova, P. Kúš, A. Ostroverkh, M. Václavů, M. Vorokhta, I. Matolínová and V. Matolín, Candle Soot as Efficient Support for Proton Exchange Membrane Fuel Cell Catalyst, *Fuel Cells*, 2016, **16**, 652–655.
- 46 V. Matolín, I. Khalakhan, I. Matolínová, M. Václavů, K. Veltruská and M. Vorokhta, Pt<sup>2+,4+</sup> ions in CeO<sub>2</sub> rf-sputtered thin films, *Surf. Interface Anal.*, 2010, **42**, 882–885.
- 47 R. Fiala, M. Vaclavu, M. Vorokhta, I. Khalakhan, J. Lavkova, V. Potin, I. Matolínová and V. Matolín, Proton Exchange Membrane Fuel Cell Made of Magnetron Sputtered Pt-CeO<sub>x</sub> and Pt-Co Thin Film Catalysts, *J. Power Sources*, 2015, **273**, 105–109.
- 48 H. Yoshikawa, I. Matolínová and V. Matolín, Practical chemical analysis of Pt and Pd based heterogeneous catalysts with hard X-ray photoelectron spectroscopy, *J. Electron Spectrosc. Relat. Phenom.*, 2013, **190**(Part B), 268–277.
- 49 K. Ševčíková, V. Nehasil, M. Vorokhta, S. Havíar, V. Matolín, I. Matolínová, K. Mašek, I. Piš, K. Kobayashi, M. Kobata, T. Nagata, Y. Matsushita and H. Yoshikawa, Altering properties of cerium oxide thin films by Rh doping, *Mater. Res. Bull.*, 2015, **67**, 5–13.
- 50 V. Matolin, M. Cabala, I. Matolinova, M. Skoda, J. Libra, M. Vaclavu, K. C. Prince, T. Skala, H. Yoshikawa, Y. Yamashita, S. Ueda and K. Kobayashi, Au<sup>+</sup> and Au<sup>3+</sup> ions in CeO<sub>2</sub> rf-sputtered thin films, *J. Phys. D: Appl. Phys.*, 2009, **42**, 115301.
- 51 V. Matolín, R. Fiala, I. Khalakhan, J. Lavková, M. Václavů and M. Vorokhta, Nanoporous Pt<sup>n+</sup>-CeO<sub>x</sub> catalyst films grown on carbon substrates, *Int. J. Nanotechnol.*, 2012, **9**, 680–694.
- 52 M. Vorokhta, I. Khalakhan, I. Matolínová, M. Kobata, H. Yoshikawa, K. Kobayashi and V. Matolín, Nanostructured Pt-CeO<sub>2</sub> thin film catalyst grown on graphite foil by magnetron sputtering, *Appl. Surf. Sci.*, 2013, **267**, 119–123.
- 53 I. Khalakhan, M. Dubau, S. Havíar, J. Lavková, I. Matolínová, V. Potin, M. Vorokhta and V. Matolín, Growth of nano-porous Pt-doped cerium oxide thin films on glassy carbon substrate, *Ceram. Int.*, 2013, **39**, 3765–3769.
- 54 M. Dubau, J. Lavková, I. Khalakhan, S. Havíar, V. Potin, V. R. Matolín and I. Matolínová, Preparation of Magnetron Sputtered Thin Cerium Oxide Films with a Large Surface on Silicon Substrates Using Carbonaceous Interlayers, *ACS Appl. Mater. Interfaces*, 2014, **6**, 1213–1218.
- 55 S. Havíar, M. Dubau, J. Lavková, I. Khalakhan, V. Potin, V. Matolín and I. Matolínová, Investigation of Growth Mechanism of Thin Sputtered Cerium Oxide Films on Carbon Substrates, *Sci. Adv. Mater.*, 2014, **6**, 1278–1285.
- 56 J. Lavkova, I. Khalakhan, M. Chundak, M. Vorokhta, V. Potin, V. Matolin and I. Matolinova, Growth and composition of nanostructured and nanoporous cerium oxide thin films on a graphite foil, *Nanoscale*, 2015, **7**, 4038–4047.
- 57 M. Vorokhta, I. Khalakhan, I. Matolínová, J. Nováková, S. Havíar, J. Lančok, M. Novotný, H. Yoshikawa and V. Matolín, PLD prepared nanostructured Pt-CeO<sub>2</sub> thin films containing ionic platinum, *Appl. Surf. Sci.*, 2017, **396**, 278–283.
- 58 N. Zanfoni, L. Avril, L. Imhoff, B. Domenichini and S. Bourgeois, Direct liquid injection chemical vapor deposition of platinum doped cerium oxide thin films, *Thin Solid Films*, 2015, **589**, 246–251.
- 59 L. Avril, N. Zanfoni, P. Simon, L. Imhoff, S. Bourgeois and B. Domenichini, MOCVD growth of porous cerium oxide thin films on silicon substrate, *Surf. Coat. Technol.*, 2015, **280**, 148–153.



- 60 P. Simon, N. Zanfoni, L. Avril, Z. Li, V. Potin, B. Domenichini and S. Bourgeois, Nanoporous Platinum Doped Cerium Oxides Thin Films Grown on Silicon Substrates: Ionic Platinum Localization and Stability, *Adv. Mater. Interfaces*, 2017, **4**, 1600821.
- 61 P. Simon, N. Zanfoni, L. Avril, J. Lavkova, I. Matolinova, L. Imhoff, V. Potin, B. Domenichini and S. Bourgeois, Observation of surface reduction in porous ceria thin film grown on graphite foil substrate, *Mater. Today*, 2016, **3**, 2772–2779.
- 62 I. Matolínová, R. Fiala, I. Khalakhan, M. Vorokhta, Z. Sofer, H. Yoshikawa, K. Kobayashi and V. Matolín, Synchrotron radiation photoelectron spectroscopy study of metal-oxide thin film catalysts: Pt-CeO<sub>2</sub> coated CNTs, *Appl. Surf. Sci.*, 2012, **258**, 2161–2164.
- 63 S. Bruyère, A. Cacucci, V. Potin, I. Matolinova, M. Vorokhta and V. Matolin, Deposition of Pt and Sn doped CeO<sub>x</sub> layers on silicon substrate, *Surf. Coat. Technol.*, 2013, **227**, 15–18.
- 64 V. Potin, J. Lavkova, S. Bourgeois, M. Dubau, I. Matolinova and V. Matolin, Structural and Chemical Characterization of Cerium Oxide Thin Layers Grown on Silicon Substrate, *Mater. Today*, 2015, **2**, 101–107.
- 65 A. Migani, G. N. Vayssilov, S. T. Bromley, F. Illas and K. M. Neyman, Dramatic Reduction of the Oxygen Vacancy Formation Energy in Ceria Particles: A Possible Key to Their Remarkable Reactivity at the Nanoscale, *J. Mater. Chem.*, 2010, **20**, 10535–10546.
- 66 A. Migani, K. M. Neyman and S. T. Bromley, Octahedrality versus tetrahedrality in stoichiometric ceria nanoparticles, *Chem. Commun.*, 2012, **48**, 4199–4201.
- 67 F. Zhang, Q. Jin and S.-W. Chan, Ceria nanoparticles: Size, size distribution, and shape, *J. Appl. Phys.*, 2004, **95**, 4319–4326.
- 68 A. Migani, G. N. Vayssilov, S. T. Bromley, F. Illas and K. M. Neyman, Greatly Facilitated Oxygen Vacancy Formation in Ceria Nanocrystallites, *Chem. Commun.*, 2010, **46**, 5936–5938.
- 69 M. M. Branda, R. M. Ferullo, M. Causà and F. Illas, Relative stabilities of low index and stepped CeO<sub>2</sub> surfaces from hybrid and GGA plus U implementations of density functional theory, *J. Phys. Chem. C*, 2011, **115**, 3716–3721.
- 70 A. Bruix and K. M. Neyman, Modeling Ceria-Based Nano-materials for Catalysis and Related Applications, *Catal. Lett.*, 2016, **146**, 2053–2080.
- 71 A. Bruix, K. M. Neyman and F. Illas, Adsorption, oxidation state, and diffusion of Pt atoms on the CeO<sub>2</sub>(111) surface, *J. Phys. Chem. C*, 2010, **114**, 14202–14207.
- 72 A. Bruix, F. Nazari, K. M. Neyman and F. Illas, On the adsorption and formation of Pt dimers on the CeO<sub>2</sub>(111) surface, *J. Chem. Phys.*, 2011, **135**, 244708.
- 73 A. Bruix, A. Migani, G. N. Vayssilov, K. M. Neyman, J. Libuda and F. Illas, Effects of deposited Pt particles on the reducibility of CeO<sub>2</sub>(111), *Phys. Chem. Chem. Phys.*, 2011, **13**, 11384–11392.
- 74 K. M. Neyman, C. Inntam, V. A. Nasluzov, R. Kosarev and N. Rösch, Adsorption of d-metal atoms on the regular MgO(001) surface: Density functional study of cluster models embedded in an elastic polarizable environment, *Appl. Phys. A: Mater. Sci. Process.*, 2004, **78**, 823–828.
- 75 K. M. Neyman, C. Inntam, A. V. Matveev, V. A. Nasluzov and N. Rösch, Single d-Metal Atoms on F<sub>s</sub> and F<sub>s</sub><sup>+</sup> Defects of MgO(001): A Theoretical Study across the Periodic Table, *J. Am. Chem. Soc.*, 2005, **127**, 11652–11660.
- 76 A. G. Hu, K. M. Neyman, M. Staufer, T. Belling, B. C. Gates and N. Rosch, A Surface Site as Polydentate Ligand of a Metal Complex: Density Functional Studies of Rhenium Subcarbonyls Supported on Magnesium Oxide, *J. Am. Chem. Soc.*, 1999, **121**, 4522–4523.
- 77 F. A. Cotton and G. Wilkinson, *Advanced Inorganic Chemistry*, Wiley, New York, 1990.
- 78 C. Kittel, *Introduction to Solid State Physics*, Wiley, New York, 1976.
- 79 Y. Nagai, T. Hirabayashi, K. Dohmae, N. Takagi, T. Minami, H. Shinjoh and S. Matsumoto, Sintering inhibition mechanism of platinum supported on ceria-based oxide and Pt-oxide-support interaction, *J. Catal.*, 2006, **242**, 103–109.
- 80 N. Nilius, S. M. Kozlov, J.-F. Jerratsch, M. Baron, X. Shao, F. Viñes, S. Shaikhutdinov, K. M. Neyman and H.-J. Freund, Formation of One-Dimensional Electronic States along the Step Edges of CeO<sub>2</sub>(111), *ACS Nano*, 2012, **6**, 1126–1133.
- 81 S. M. Kozlov, F. Viñes, N. Nilius, S. Shaikhutdinov and K. M. Neyman, Absolute Surface Step Energies: Accurate Theoretical Methods Applied to Ceria Nanoislands, *J. Phys. Chem. Lett.*, 2012, **3**, 1956–1961.
- 82 A. Figueroba, G. Kovács, A. Bruix and K. M. Neyman, Towards stable single-atom catalysts: Strong binding of atomically dispersed transition metals on the surface of nanostructured ceria, *Catal. Sci. Technol.*, 2016, **6**, 6806–6813.
- 83 M. A. Sk, S. M. Kozlov, K. H. Lim, A. Migani and K. M. Neyman, Oxygen Vacancies in Self-Assemblies of Ceria Nanoparticles, *J. Mater. Chem. A*, 2014, **2**, 18329–18338.
- 84 R. Nedyalkova, D. Niznansky and A.-C. Roger, Iron–ceria-zirconia fluorite catalysts for methane selective oxidation to formaldehyde, *Catal. Commun.*, 2009, **10**, 1875–1880.
- 85 A. Satsuma, M. Yanagihara, J. Ohyama and K. Shimizu, Oxidation of CO over Ru/Ceria prepared by self-dispersion of Ru metal powder into nano-sized particle, *Catal. Today*, 2013, **201**, 62–67.
- 86 S. S. Y. Lin, D. H. Kim, M. H. Engelhard and S. Y. Ha, Water-induced formation of cobalt oxides over supported cobalt/ceria-zirconia catalysts under ethanol-steam conditions, *J. Catal.*, 2010, **273**, 229–235.
- 87 M. Haneda, K. Shinoda, A. Nagane, O. Houshito, H. Takagi, Y. Nakahara, K. Hiroe, T. Fujitani and H. Hamada, Catalytic performance of rhodium supported on ceria-zirconia mixed oxides for reduction of NO by propene, *J. Catal.*, 2008, **259**, 223–231.

- 88 Y. Huang, A. Wang, L. Li, X. Wang, D. Su and T. Zhang, "Ir-in-ceria": A highly selective catalyst for preferential CO oxidation, *J. Catal.*, 2008, **255**, 144–152.
- 89 H. A. Aleksandrov, K. M. Neyman and G. N. Vayssilov, The Structure and Stability of Reduced and Oxidized Mononuclear Platinum Species on Nanostructured Ceria from Density Functional Modeling, *Phys. Chem. Chem. Phys.*, 2015, **17**, 14551–14560.
- 90 T. Wu, X. Pan, Y. Zhang, Z. Miao, B. Zhang, J. Li and X. Yang, Investigation of the Redispersion of Pt Nanoparticles on Polyhedral Ceria Nanoparticles, *J. Phys. Chem. Lett.*, 2014, **5**, 2479–2483.
- 91 Y. Gao, W. Wang, S. Chang and W. Huang, Morphology Effect of CeO<sub>2</sub> Support in the Preparation, Metal-Support Interaction, and Catalytic Performance of Pt/CeO<sub>2</sub> Catalysts, *ChemCatChem*, 2013, **5**, 3610–3620.
- 92 J. Carrasco, D. López-Durán, Z. Liu, T. Duchoň, J. Evans, S. D. Senanayake, E. J. Crumlin, V. Matolín, J. A. Rodriguez and M. V. Ganduglia-Pirovano, In Situ and Theoretical Studies for the Dissociation of Water on an Active Ni/CeO<sub>2</sub> Catalyst: Importance of Strong Metal-Support Interactions for the Cleavage of O-H Bonds, *Angew. Chem., Int. Ed.*, 2015, **54**, 3917–3921.
- 93 S. Colussi, A. Gayen, M. Farnesi Camellone, M. Boaro, J. Llorca, S. Fabris and A. Trovarelli, Nanofaceted Pd-O Sites in Pd-Ce Surface Superstructures: Enhanced Activity in Catalytic Combustion of Methane, *Angew. Chem., Int. Ed.*, 2009, **48**, 8481–8484.
- 94 R. V. Gulyaev, T. Y. Kardash, S. E. Malykhin, O. A. Stonkus, A. S. Ivanova and A. I. Boronin, The local structure of Pd<sub>x</sub>Ce<sub>1-x</sub>O<sub>2-x-δ</sub> solid solutions, *Phys. Chem. Chem. Phys.*, 2014, **16**, 13523–13539.
- 95 J. S. Elias, M. Risch, L. Giordano, A. N. Mansour and Y. Shao-Horn, Structure, Bonding, and Catalytic Activity of Monodisperse, Transition-Metal-Substituted CeO<sub>2</sub> Nanoparticles, *J. Am. Chem. Soc.*, 2014, **136**, 17193–17200.
- 96 H. Müller-Buschbaum, Zur Kristallchemie der Oxoargentate und Silberoxometallate, *Z. Anorg. Allg. Chem.*, 2004, **630**, 2125–2175.
- 97 A. M. Venezia, G. Pantaleo, A. Longo, G. Di Carlo, M. P. Casalotto, F. L. Liotta and G. Deganello, Relationship between Structure and CO Oxidation Activity of Ceria-Supported Gold Catalysts, *J. Phys. Chem. B*, 2005, **109**, 2821–2827.
- 98 A. Neitzel, A. Figueroba, Y. Lykhach, T. Skála, M. Vorokhta, N. Tsud, S. Mehl, K. Ševčíková, K. C. Prince, K. M. Neyman, V. Matolín and J. Libuda, Atomically Dispersed Pd, Ni and Pt Species in Ceria-Based Catalysts: Principal Differences in Stability and Reactivity, *J. Phys. Chem. C*, 2016, **120**, 9852–9862.
- 99 Y. Lykhach, A. Figueroba, M. F. Camellone, A. Neitzel, T. Skála, F. R. Negreiros, M. Vorokhta, N. Tsud, K. C. Prince, S. Fabris, K. M. Neyman, V. Matolín and J. Libuda, Reactivity of Atomically Dispersed Pt<sup>2+</sup> Species towards H<sub>2</sub>: Model Pt-CeO<sub>2</sub> Fuel Cell Catalyst, *Phys. Chem. Chem. Phys.*, 2016, **18**, 7672–7679.
- 100 F. Dvořák, O. Stetsovych, M. Steger, E. Cherradi, I. Matolínová, N. Tsud, M. Škoda, T. Skála, J. Myšliveček and V. Matolín, Adjusting Morphology and Surface Reduction of CeO<sub>2</sub>(111) Thin Films on Cu(111), *J. Phys. Chem. C*, 2011, **115**, 7496–7503.
- 101 D. R. Mullins, P. M. Albrecht, T.-L. Chen, F. C. Calaza, M. D. Biegalski, H. M. Christen and S. H. Overbury, Water Dissociation on CeO<sub>2</sub>(100) and CeO<sub>2</sub>(111) Thin Films, *J. Phys. Chem. C*, 2012, **116**, 19419–19428.
- 102 A. Bruix, J. A. Rodriguez, P. J. Ramírez, S. D. Senanayake, J. Evans, J. B. Park, D. Stacchiola, P. Liu, J. Hrbek and F. Illas, A New Type of Strong Metal-Support Interaction and the Production of H<sub>2</sub> through the Transformation of Water on Pt/CeO<sub>2</sub>(111) and Pt/CeO<sub>x</sub>/TiO<sub>2</sub>(110) Catalysts, *J. Am. Chem. Soc.*, 2012, **134**, 8968–8974.
- 103 Q. Fu, H. Saltsburg and M. Flytzani-Stephanopoulos, Active Nonmetallic Au and Pt Species on Ceria-Based Water-Gas Shift Catalysts, *Science*, 2003, **301**, 935–938.
- 104 M. Hatanaka, N. Takahashi, T. Tanabe, Y. Nagai, K. Dohmae, Y. Aoki, T. Yoshida and H. Shinjoh, Ideal Pt loading for a Pt/CeO<sub>2</sub>-based catalyst stabilized by a Pt-O-Ce bond, *Appl. Catal., B*, 2010, **99**, 336–342.
- 105 G. Ertl, H. Knözinger, F. Schüth and J. Weitkamp, *Handbook of Heterogeneous Catalysis*, Wiley, Weinheim, 2008.
- 106 F. M. Hoffmann, Infrared reflection-absorption spectroscopy of adsorbed molecules, *Surf. Sci. Rep.*, 1983, **3**, 107–192.
- 107 J. M. Chalmers and P. R. Griffiths, *Handbook of vibrational spectroscopy*, John Wiley & Sons, Ltd., Chichester, UK, 2001.
- 108 K. I. Hadjiivanov and G. N. Vayssilov, in *Adv. Catal.*, Academic Press, 2002, vol. 47, pp. 307–511.
- 109 O. Brummel, F. Waidhas, F. Faisal, R. Fiala, M. Vorokhta, I. Khalakhan, M. Dubau, A. Figueroba, G. Kovács, H. A. Aleksandrov, G. N. Vayssilov, S. M. Kozlov, K. M. Neyman, V. Matolín and J. Libuda, Stabilization of Small Platinum Nanoparticles on Pt-CeO<sub>2</sub> Thin Film Electrocatalysts During Methanol Oxidation, *J. Phys. Chem. C*, 2016, **120**, 19723–19736.
- 110 H. A. Aleksandrov, K. M. Neyman, K. I. Hadjiivanov and G. N. Vayssilov, Can the state of platinum species be unambiguously determined by the stretching frequency of an adsorbed CO probe molecule?, *Phys. Chem. Chem. Phys.*, 2016, **18**, 22108–22121.
- 111 M. J. Kappers and J. H. van der Maas, Correlation between CO frequency and Pt coordination number. A DRIFT study on supported Pt catalysts, *Catal. Lett.*, 1991, **10**, 365–373.
- 112 A. Neitzel, Y. Lykhach, T. Skála, N. Tsud, M. Vorokhta, D. Mazur, K. C. Prince, V. Matolín and J. Libuda, Surface Sites on Pt-CeO<sub>2</sub> Mixed Oxide Catalysts Probed by CO Adsorption: A Synchrotron Radiation Photoelectron Spectroscopy Study, *Phys. Chem. Chem. Phys.*, 2014, **16**, 24747–24754.
- 113 G. N. Vayssilov, M. Mihaylov, P. S. Petkov, K. I. Hadjiivanov and K. M. Neyman, Reassignment of the Vibrational



- Spectra of Carbonates, Formates, and Related Surface Species on Ceria: A Combined Density Functional and Infrared Spectroscopy Investigation, *J. Phys. Chem. C*, 2011, **115**, 23435–23454.
- 114 G. Dutta, U. V. Waghmare, T. Baidya and M. S. Hegde, Hydrogen Spillover on  $\text{CeO}_2/\text{Pt}$ : Enhanced Storage of Active Hydrogen, *Chem. Mater.*, 2007, **19**, 6430–6436.
- 115 P. Bera, K. R. Priolkar, A. Gayen, P. R. Sarode, M. S. Hegde, S. Emura, R. Kumashiro, V. Jayaram and G. N. Subbanna, Ionic Dispersion of Pt over  $\text{CeO}_2$  by the Combustion Method: Structural Investigation by XRD, TEM, XPS, and EXAFS, *Chem. Mater.*, 2003, **15**, 2049–2060.
- 116 B. D. Mukri, U. V. Waghmare and M. S. Hegde, Platinum Ion-Doped  $\text{TiO}_2$ : High Catalytic Activity of  $\text{Pt}^{2+}$  with Oxide Ion Vacancy in  $\text{Ti}^{4+}_{1-x}\text{Pt}^{2+}_x\text{O}_{2-x}$  Compared to  $\text{Pt}^{4+}$  without Oxide Ion Vacancy in  $\text{Ti}^{4+}_{1-x}\text{Pt}^{4+}_x\text{O}_2$ , *Chem. Mater.*, 2013, **25**, 3822–3833.
- 117 Y. Lykhach, S. M. Kozlov, T. Skála, A. Tovt, V. Stetsovich, N. Tsud, F. Dvořák, V. Johánek, A. Neitzel, J. Mysliveček, S. Fabris, V. Matolín, K. M. Neyman and J. Libuda, Counting Electrons on Supported Nanoparticles, *Nat. Mater.*, 2016, **15**, 284–288.
- 118 Y. Lykhach, T. Staudt, M. Vorokhta, T. Skála, V. Johánek, K. C. Prince, V. Matolín and J. Libuda, Hydrogen Spillover Monitored by Resonant Photoemission Spectroscopy, *J. Catal.*, 2012, **285**, 6–9.
- 119 G. N. Vayssilov, Y. Lykhach, A. Migani, T. Staudt, G. P. Petrova, N. Tsud, T. Skála, A. Bruix, F. Illas, K. C. Prince, V. Matolín, K. M. Neyman and J. Libuda, Support Nanostructure Boosts Oxygen Transfer to Catalytically Active Platinum Nanoparticles, *Nat. Mater.*, 2011, **10**, 310–315.
- 120 C. Kittel, *Introduction to Solid State Physics*, 8th edition, Wiley, 2004.
- 121 A. Neitzel, V. Johánek, Y. Lykhach, T. Skála, N. Tsud, M. Vorokhta, V. Matolín and J. Libuda, Reduction of  $\text{Pt}^{2+}$  species in model Pt– $\text{CeO}_2$  fuel cell catalysts upon reaction with methanol, *Appl. Surf. Sci.*, 2016, **387**, 674–681.
- 122 V. Matolín, J. Libra, M. Škoda, N. Tsud, K. C. Prince and T. Skála, Methanol Adsorption on a  $\text{CeO}_2(111)/\text{Cu}(111)$  Thin Film Model Catalyst, *Surf. Sci.*, 2009, **603**, 1087–1092.
- 123 D. R. Mullins, M. D. Robbins and J. Zhou, Adsorption and Reaction of Methanol on Thin-Film Cerium Oxide, *Surf. Sci.*, 2006, **600**, 1547–1558.
- 124 M. Capdevila-Cortada, M. García-Melchor and N. López, Unraveling the structure sensitivity in methanol conversion on  $\text{CeO}_2$ : A DFT + U study, *J. Catal.*, 2015, **327**, 58–64.
- 125 D. J. Miller, H. Öberg, S. Kaya, H. Sanchez Casalongue, D. Friebel, T. Anniyev, H. Ogasawara, H. Bluhm, L. G. M. Pettersson and A. Nilsson, Oxidation of Pt(111) under Near-Ambient Conditions, *Phys. Rev. Lett.*, 2011, **107**, 195502.
- 126 F. Pilger, A. Testino, A. Carino, C. Proff, A. Kambolis, A. Cervellino and C. Ludwig, Size Control of Pt Clusters on  $\text{CeO}_2$  Nanoparticles via an Incorporation–Segregation Mechanism and Study of Segregation Kinetics, *ACS Catal.*, 2016, **6**, 3688–3699.
- 127 Y. Lykhach, A. Figueroba, T. Skála, T. Duchoň, N. Tsud, M. Aulická, A. Neitzel, K. Veltruská, K. C. Prince, V. Matolín, K. M. Neyman and J. Libuda, Redox-mediated conversion of atomically dispersed platinum to sub-nanometer particles, *J. Mater. Chem. A*, 2017, **5**, 9250–9261.
- 128 J. Paier, C. Penschke and J. Sauer, Oxygen Defects and Surface Chemistry of Ceria: Quantum Chemical Studies Compared to Experiment, *Chem. Rev.*, 2013, **113**, 3949–3985.
- 129 M. V. Ganduglia-Pirovano, J. L. F. Da Silva and J. Sauer, Density-Functional Calculations of the Structure of Near-Surface Oxygen Vacancies and Electron Localization on  $\text{CeO}_2(111)$ , *Phys. Rev. Lett.*, 2009, **102**, 026101–026104.
- 130 T. Skála, F. Šutara, K. C. Prince and V. Matolín, Cerium oxide stoichiometry alteration via Sn deposition: Influence of temperature, *J. Electron Spectrosc. Relat. Phenom.*, 2009, **169**, 20–25.
- 131 M. Škoda, M. Cabala, V. Cháb, K. C. Prince, L. Sedláček, T. Skála, F. Šutara and V. Matolín, Sn interaction with  $\text{CeO}_2(111)$  system: Bimetallic bonding and ceria reduction, *Appl. Surf. Sci.*, 2008, **254**, 4375–4379.
- 132 A. Neitzel, Y. Lykhach, T. Skála, N. Tsud, V. Johánek, M. Vorokhta, K. C. Prince, V. Matolín and J. Libuda, Hydrogen activation on Pt–Sn nanoalloys supported on mixed Sn–Ce oxide films, *Phys. Chem. Chem. Phys.*, 2014, **16**, 13209–13219.
- 133 C. T. Campbell, S. C. Parker and D. E. Starr, The Effect of Size-Dependent Nanoparticle Energetics on Catalyst Sintering, *Science*, 2002, **298**, 811–814.
- 134 G. N. Vayssilov, A. Migani and K. Neyman, Density Functional Modeling of the Interactions of Platinum Clusters with  $\text{CeO}_2$  Nanoparticles of Different Size, *J. Phys. Chem. C*, 2011, **115**, 16081–16086.
- 135 Z. Lu and Z. Yang, Interfacial properties of NM– $\text{CeO}_2(111)$  (NM = noble metal atoms or clusters of Pd, Pt and Rh): a first principles study, *J. Phys.: Condens. Matter*, 2010, **22**, 475003.
- 136 S. M. Kozlov and K. M. Neyman, Effects of electron transfer in model catalysts composed of Pt nanoparticles on  $\text{CeO}_2(111)$  surface, *J. Catal.*, 2016, **344**, 507–514.
- 137 F. R. Negreiros and S. Fabris, Role of Cluster Morphology in the Dynamics and Reactivity of Subnanometer Pt Clusters Supported on Ceria Surfaces, *J. Phys. Chem. C*, 2014, **118**, 21014–21020.
- 138 Y. Pan, N. Nilius, H.-J. Freund, J. Paier, C. Penschke and J. Sauer, Titration of  $\text{Ce}^{3+}$  Ions in the  $\text{CeO}_2(111)$  Surface by Au Adatoms, *Phys. Rev. Lett.*, 2013, **111**, 206101.
- 139 K. Ševčíková, L. Szabová, M. Kettner, P. Homola, N. Tsud, S. Fabris, V. Matolín and V. Nehasil, Experimental and Theoretical Study on the Electronic Interaction between Rh Adatoms and  $\text{CeO}_x$  Substrate in Dependence on a Degree of Cerium Oxide Reduction, *J. Phys. Chem. C*, 2016, **120**, 5468–5476.
- 140 K. Ševčíková, T. Kolářová, T. Skála, N. Tsud, M. Václavů, Y. Lykhach, V. Matolín and V. Nehasil, Impact of Rh– $\text{CeO}_x$  interaction on CO oxidation mechanisms, *Appl. Surf. Sci.*, 2015, **332**, 747–755.



- Open Access Article. Published on 02 June 2017. Downloaded on 9/24/2019 9:35:03 AM.  
This article is licensed under a Creative Commons Attribution 3.0 Unported Licence.
- 
- 141 Y. Lykhach, V. Johánek, H. Aleksandrov, S. M. Kozlov, M. Happel, T. Skála, P. S. Petkov, N. Tsud, G. N. Vayssilov, K. C. Prince, K. M. Neyman, V. Matolín and J. Libuda, Water Chemistry on Model Ceria and Pt/Ceria Catalysts, *J. Phys. Chem. C*, 2012, **116**, 12103–12113.
- 142 V. Matolín, I. Matolínová, F. Dvořák, V. Johánek, J. Mysliveček, K. C. Prince, T. Skála, O. Stetsovich, N. Tsud, M. Václavů and B. Šmíd, Water Interaction with CeO<sub>2</sub>(111)/Cu(111) Model Catalyst Surface, *Catal. Today*, 2012, **181**, 124–132.
- 143 L. Szabová, Y. Tateyama, V. Matolín and S. Fabris, Water Adsorption and Dissociation at Metal-Supported Ceria Thin Films: Thickness and Interface-Proximity Effects Studied with DFT+U Calculations, *J. Phys. Chem. C*, 2015, **119**, 2537–2544.
- 144 M. Farnesi Camellone, F. Negreiros Ribeiro, L. Szabová, Y. Tateyama and S. Fabris, Catalytic Proton Dynamics at the Water/Solid Interface of Ceria-Supported Pt Clusters, *J. Am. Chem. Soc.*, 2016, **138**, 11560–11567.
- 145 S. M. Kozlov and K. M. Neyman, O vacancies on steps on the CeO<sub>2</sub>(111) surface, *Phys. Chem. Chem. Phys.*, 2014, **16**, 7823–7829.
- 146 S. Garrettin, P. Concepción, A. Corma, J. M. López Nieto and V. F. Puntes, Nanocrystalline CeO<sub>2</sub> Increases the Activity of Au for CO Oxidation by Two Orders of Magnitude, *Angew. Chem., Int. Ed.*, 2004, **43**, 2538–2540.
- 147 V. Fiorin, D. Borthwick and D. A. King, Microcalorimetry of O<sub>2</sub> and NO on flat and stepped platinum surfaces, *Surf. Sci.*, 2009, **603**, 1360–1364.
- 148 P. Ghosh, M. Farnesi Camellone and S. Fabris, Fluxionality of Au Clusters at Ceria Surfaces during CO Oxidation: Relationships among Reactivity, Size, Cohesion, and Surface Defects from DFT Simulations, *J. Phys. Chem. Lett.*, 2013, **4**, 2256–2263.
- 149 P. C. Jennings, H. A. Aleksandrov, K. M. Neyman and R. L. Johnston, A DFT study of oxygen dissociation on platinum based nanoparticles, *Nanoscale*, 2014, **6**, 1153–1165.
- 150 P. C. Jennings, H. A. Aleksandrov, K. M. Neyman and R. L. Johnston, DFT studies of oxygen dissociation on the 116-atom platinum truncated octahedron particle, *Phys. Chem. Chem. Phys.*, 2014, **16**, 26539–26545.
- 151 P. C. Jennings, H. A. Aleksandrov, K. M. Neyman and R. L. Johnston, O<sub>2</sub> Dissociation on M@Pt Core–Shell Particles for 3d, 4d, and 5d Transition Metals, *J. Phys. Chem. C*, 2015, **119**, 11031–11041.
- 152 F. Viñes, C. Loschen, F. Illas and K. M. Neyman, Edge sites as a gate for subsurface carbon in palladium nanoparticles, *J. Catal.*, 2009, **266**, 59–63.
- 153 K. M. Neyman and S. Schauermann, Hydrogen Diffusion into Palladium Nanoparticles: Pivotal Promotion by Carbon, *Angew. Chem., Int. Ed.*, 2010, **49**, 4743–4746.
- 154 M. Hatanaka, N. Takahashi, N. Takahashi, T. Tanabe, Y. Nagai, A. Suda and H. Shinjoh, Reversible Changes in the Pt Oxidation State and Nanostructure on a Ceria-Based Supported Pt, *J. Catal.*, 2009, **266**, 182–190.
- 155 Y. Nagai, K. Dohmae, Y. Ikeda, N. Takagi, T. Tanabe, N. Hara, G. Guilera, S. Pascarelli, M. A. Newton, O. Kuno, H. Jiang, H. Shinjoh and S. I. Matsumoto, In Situ Redispersion of Platinum Autoexhaust Catalysts: An On-Line Approach to Increasing Catalyst Lifetimes?, *Angew. Chem., Int. Ed.*, 2008, **47**, 9303–9306.
- 156 Y. Nagai, K. Dohmae, Y. Ikeda, N. Takagi, N. Hara, T. Tanabe, G. Guilera, S. Pascarelli, M. A. Newton, N. Takahashi, H. Shinjoh and S. I. Matsumoto, In situ observation of platinum sintering on ceria-based oxide for autoexhaust catalysts using Turbo-XAS, *Catal. Today*, 2011, **175**, 133–140.
- 157 M. Happel, J. Mysliveček, V. Johánek, F. Dvořák, O. Stetsovich, Y. Lykhach, V. Matolín and J. Libuda, Adsorption Sites, Metal Support Interactions, and Oxygen Spillover Identified by Vibrational Spectroscopy of Adsorbed CO: A Reference Study on Pt/Ceria Model Catalysts, *J. Catal.*, 2012, **289**, 118–126.
- 158 D. K. Lambert, Stark effect of adsorbate vibrations, *Solid State Commun.*, 1984, **51**, 297–300.
- 159 F. Meng, S. A. Morin, A. Forticaux and S. Jin, Screw Dislocation Driven Growth of Nanomaterials, *Acc. Chem. Res.*, 2013, **46**, 1616–1626.
- 160 X. Yin, J. Shi, X. Niu, H. Huang and X. Wang, Wedding Cake Growth Mechanism in One-Dimensional and Two-Dimensional Nanostructure Evolution, *Nano Lett.*, 2015, **15**, 7766–7772.